RUPERTO-CAROLA-UNIVERSITY
HEIDELBERG

Hayk Pirumov

QCD Analysis of Neutral and Charged Current Cross Sections

and

Search for Contact Interactions at HERA

2013

PHYSICAL INSTITUTE

Dissertation

submitted to the

Combined Faculties of the Natural Sciences and

Mathematics

of the Ruperto-Carola-University of Heidelberg,

Germany

for the degree of

Doctor of Natural Sciences

Put forward by

Mast. Phys. YSU Hayk Pirumov

born in Yerevan, Armenia

citizen of Armenia

Oral examination: 17$^{\text{th}}$ of April 2013

QCD Analysis of Neutral and Charged Current Cross Sections

and

Search for Contact Interactions at HERA

Referees: Prof. Dr. André Schöning

Prof. Dr. Hans-Christian Schultz-Coulon

Abstract

A QCD analysis of the inclusive deep inelastic ep scattering cross section measured by the H1 experiment at HERA is presented. The data correspond to a total integrated luminosity of about $0.5\,\mathrm{fb}^{-1}$ and covers a kinematic range of $0.5\,\mathrm{GeV}^2 - 30000\,\mathrm{GeV}^2$ in the negative four-momentum transfer Q^2 and $3 \cdot 10^{-5} - 0.65$ in Bjorken x. The performed QCD analysis of the double differential neutral and charged current cross sections results in a set of parton distribution functions H1PDF 2012. The precise data from HERA II period in the kinematic region of high Q^2 considerably improve the accuracy of the PDFs at the high x. In addition a search for signs of new physics using single differential neutral current cross section measurements at high Q^2 is performed. The observed good agreement of the analysed data with the Standard Model predictions allows to set constraints on various new physics models within the framework of contact interactions. Limits are derived on the compositeness scale for general contact interactions, on the ratio of mass to the Yukawa coupling for heavy leptoquark models, on the effective Plank-mass scale in the large extra dimension models and on the quark radius.

Zusammenfassung

Eine QCD Analyse des inklusiven tiefinelastischen ep Wirkungsquerschnittes, der am H1-Experiment bei HERA gemessen wurde, wird beschrieben. Die untersuchten Daten entsprechen einer totalen integrierten Luminosität von etwa $0.5\,\mathrm{fb}^{-1}$ und wurden in kinematischen Bereich von $0.5\,\mathrm{GeV}^2 - 30000\,\mathrm{GeV}^2$ des quadrierten Viererimpuls-übertrags Q^2 und von $3 \cdot 10^{-5} - 0.65$ des relativen Protonimulse x genommen. Mittels der durchgeführten QCD Analyse der einfach und doppelt differentiellen Wirkungsquerschnitte der neutralen und geladenen Ströme wird eine Reihe von Parton-Verteilungsfunktionen H1PDF 2012 bestimmt. Die präzisen HERA II Daten bei hohen Werten von Q^2, tragen wesentlichen zur Verbesserung der Genauigkeit der PDFs im Bereich-hoher x-Werte bei. Zusätzlich wird eine Suche nach Anzeichen neuer Physik bei der Analyse einfach differentieller Wirkungsquerschnitte von neutralen Strömen bei hohen Q^2 durchgeführt. Die beobachtete gute Übereinstimmung der analysierten Daten mit den Vorhersagen des Standardmodells erlaubt das Setzen von Grenzen auf diverse Modelle im Rahmen von Kontakt-wechselwirkungen. Grenzen werden dabei auf verschiedene Modelle gesetzt: Allgemeine "Compositeness"-Modelle, auf das Verhältnis von Masse zu Yukawa-Kopplung für schwere Leptoquark-Modelle, für Modelle mit grossen Extra-Dimensionen auf die effektive Plank-Masse und für den Quark-Radius.

Contents

Contents

Contents

1

Introduction

Particle physics is a branch of physics that is trying to answer the question, "What is the matter made of?" on the most fundamental level. The fundamental constituents of matter are leptons and quarks. They are arranged into generations characterised by lepton numbers and quark flavours, respectively. Leptons are free particles that can be detected. Quarks only exist in bound states – hadrons. The existence of quarks can be investigated by experimental measurements of the properties of particle interactions. There are three generations of leptons: the electron and the electron neutrino, the muon and the muon neutrino, and the tau and the tau neutrino. The quarks are grouped in three pairs: down and up, strange and charm, bottom and top. The particles interact with each other via the exchange of gauge bosons. There are four types of interaction known: gravitational, electromagnetic, weak and strong forces. Gravitation interaction is by far the weakest of the four and plays no role in particle physics. The electromagnetic interaction is mediated by the photon. The weak interaction involves the exchange of heavy gauge bosons, Z^0, W^+ and W^-. The strong interaction is mediated by gluons. Each type of the interactions is characterised by a charge (electric, weak or strong charge). Neutrinos, which carry no electric charge, interact only weakly. Charged

leptons take part in weak and electromagnetic interactions. The quarks take part in all known interactions.

The theoretical framework which describes all the particles and interactions that includes the results of experimental and theoretical investigations of many years is known as the Standard Model of particle physics (SM).The components of the SM are the electroweak theory which unifies the weak and electromagnetic interactions and Quantum Chromodynamics (QCD) that describes strong interactions. In addition the SM predicts existence of a boson responsible for the particles to have mass known as the Higgs boson. A new Higgs-like boson has recently been observed at the Large Hadron Collider (LHC). The SM is a successful theory, however there are still questions that need to be clarified.

The HERA (Hadron Electron Ring Anlage) facility located at DESY (Deutsches Elektronen-Synchroton) research centre in Hamburg was the worlds only electron-proton collider. HERA operated from 1992 to 2007 at a centre of mass energy of $319\,\mathrm{GeV}$ with integrated luminosity of $\sim 1\,\mathrm{fb}^{-1}$ delivered to two $e^{\pm}p$ collision experiments H1 [1] and ZEUS [2]. HERA gave a unique opportunity on one hand to investigate the structure of matter and the fundamental interactions described by the SM, and on the other hand to look for phenomena that are not in the scope of the Standard Model.

Both aspects are investigated in the presented work. Deep inelastic neutral and charged current cross sections measured by the H1 experiment during the whole operating period are analysed to investigate the structure of the proton. As a result a new set of parton distribution functions (PDF) H1PDF 2012 was extracted. Single differential neutral current cross sections measured by the H1 are analysed in a search for deviations from the Standard Model predictions. The concept of four-fermion contact interactions (CI) was used to describe possible effects due to new physics.

The thesis is organised in a following way:

- chapter 2 provides a short theoretical overview of the deep inelastic *ep* scattering, the cross sections of the neutral and charged current processes as well as the concept of contact interactions and the new physics models considered in this work,

- chapter 3 gives a brief overview of the HERA collider and the H1 detector,

- presents a description of the neutral and charged current cross sections measurement procedure based on various inclusive analysis by the H1 collaboration,

- contains the description of the statistical methods used in the QCD and CI analyses.

- describes the QCD analysis of the inclusive H1 data.

- shows details of the CI analysis as well as the results of the studies.

- finally summarises the presented analyses.

Chapter
2

Theoretical overview

2.1 Deep inelastic ep scattering

Deep inelastic scattering (DIS) is a process in which a lepton scatters off a nucleon with large negative four-momentum transfer Q^2. Two types of deep inelastic scattering processes are measured at HERA. The processes are classified according to the particles exchanged between the interacting electron and proton and are called neutral current (NC) or charged current (CC).

In the neutral current process, $ep \to eX$ the interaction is mediated via exchange of a neutral boson, either a photon or a Z^0. At four-momenta transferred smaller than the square of the Z boson mass ($\sim 91\,\text{GeV}^2$), $Q^2 \ll M_Z^2$, the γ exchange process is dominating. The final state contains the scattered electron and hadrons. Processes with an exchange of a charged W^+ or W^- boson are designated as charged current. In this case a neutrino is produced in the final state instead of the scattered electron $ep \to \nu_e X$. Both processes are schematically shown in the Feynman diagrams in Figure 2.1. The four-momenta vectors of the initial lepton and the scattered lepton are indicated by l and l'. The four-momentum of the
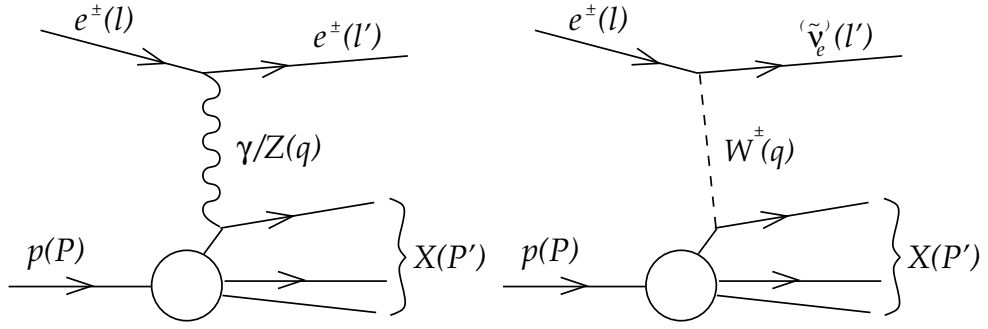
Figure 2.1: Schematic Feynman diagrams of neutral current (left) and charged current (right) deep inelastic scattering processes.

incoming proton is labelled as P. P' is the four-vector of the hadronic final state.

The following kinematic variables are used to describe the DIS process:

- Center of mass energy squared

$$s = (l + P)^2. \tag{2.1}$$

- Negative squared four-momentum transfer at the electron vertex, also referred as virtuality

$$Q^2 = -q^2 = (l - l')^2. \tag{2.2}$$

- The inelasticity is the fraction of the energy transferred from the electron to the proton via the exchanged boson

$$y = \frac{P \cdot q}{P \cdot l}. \tag{2.3}$$

- The Bjorken scaling variable

$$x = \frac{Q^2}{2P \cdot q}. \tag{2.4}$$

In the Quark Parton Model (QPM), where the proton is assumed to consist of point-like constituents called partons, x is interpreted as a fraction of the proton momentum carried by the interacting quark.

The introduced variables are related to each other via[1]

$$Q^2 = sxy. \tag{2.5}$$

This means that at a given *ep* centre of mass energy $\sqrt{s}$ any two of the x, y, Q^2 variables are enough to describe the kinematics of the DIS process. HERA was operating at the centre of mass energy of $\sqrt{s} = 319\,\text{GeV}$ and covered the kinematic range of $1 < Q^2 < 5 \cdot 10^4\,\text{GeV}^2$ and $10^{-5} < x < 0.65$.

2.2 Cross section of deep inelastic scattering

The differential cross section for the DIS process is expressed via leptonic $L^{\mu\nu}$ and hadronic $W_{\mu\nu}$ tensors [3].

$$d\sigma_{DIS} = \frac{d^3 l'}{8\pi s |\vec{l}|} \sum_a p_a \cdot L_a^{\mu\nu}(l,q) W_{\mu\nu}(p,q). \tag{2.6}$$

For the NC process index a runs over three processes: pure γ exchange, pure Z exchange and the γZ interference between these two of them. In case of the CC process there is only one term, corresponding to the $W^\pm$ exchange. The factors p_a correspond to propagator terms

$$
\begin{aligned}
p_\gamma &= \frac{1}{Q^4}, \\
p_{\gamma Z} &= \frac{1}{Q^2(Q^2 + M_Z^2)}, \\
p_Z &= \frac{1}{(Q^2 + M_Z^2)^2} \quad \text{and} \\
p_W &= \frac{1}{64 \sin^4 \Theta_W (Q^2 + W_W^2)^2},
\end{aligned} \tag{2.7}
$$

where e is the electrical charge of the incoming lepton and Θ_W is the Weinberg angel. The Weinberg angle is related to the masses of the $W^\pm$ and Z^0 via $\sin^2(\Theta_W) = 1 - M_W^2/M_Z^2$.

The leptonic tensor L is known from QED and is defined by the lepton

---

[1]This is valid only if the masses of the particles are much smaller compared to the centre of mass energy and are neglected.

momenta l and l' as [4]

$$
\begin{aligned}
L_\gamma^{\mu\nu} &= 2(l^\mu l'^\nu + l^\nu l'^\mu - ll' g^{\mu\nu} - i\lambda\epsilon^{\mu\nu\lambda\rho} l_\lambda l'_\rho), \\
L_{\gamma Z}^{\mu\nu} &= (v_e + e\lambda a_e) L_\gamma^{\mu\nu}, \\
L_Z^{\mu\nu} &= (v_e + e\lambda a_e)^2 L_\gamma^{\mu\nu} \quad \text{and} \\
L_W^{\mu\nu} &= (1 + e\lambda)^2 L_\gamma^{\mu\nu}.
\end{aligned}
\tag{2.8}
$$

Here $e = \pm 1$ is the charge of the incoming electron and $\lambda = \pm 1$ is the helicity. The vector coupling of the electron to the Z boson is $v_e = -1/2 - 2e \sin^2 \Theta_W$ and $a_e = -1/2$ is the axial coupling constant.

The hadronic tensor describes the nucleon vertex and has the form [4]

$$
\begin{aligned}
W_{\mu\nu}^a &= - \left(g_{\mu\nu} - \frac{q^\mu q^\nu}{q^2} \right) F_1^a(x, Q^2) \\
&\quad + \left(P_\mu - q_\mu \frac{P \cdot q}{q^2} \right) \left(P_\nu - q_\nu \frac{P \cdot q}{q^2} \right) \frac{1}{\nu m_p} F_2^a(x, Q^2) \\
&\quad - i\epsilon_{\mu\nu\lambda\rho} P^\lambda q^\rho \frac{1}{\nu m_p} F_3^a(x, Q^2).
\end{aligned}
\tag{2.9}
$$

The functions $F_i^a(x, Q^2)$ are the structure functions of the proton. Using these functions one can fully describe a DIS process involving a proton.

For the parity conserving photon exchange, the photon-proton cross section is given by

$$
\sigma^\gamma = \frac{4\pi^2 \alpha}{Q^2(1-x)} F_2^\gamma = \sigma_T^\gamma + \sigma_L^\gamma = \frac{4\pi^2 \alpha}{Q^2(1-x)} (2x F_1^\gamma + F_L^\gamma),
\tag{2.10}
$$

where σ_T^γ and σ_L^γ are the transverse and longitudinal photon scattering cross sections and F_L^γ is defined as $F_L^\gamma = F_2^\gamma - 2x F_1^\gamma$.

The double differential cross section of an inelastic scattering process is then given in terms of x, y, Q^2 from Equation 2.6 - Equation 2.10 by

$$
\frac{d^2 \sigma^i(e^\pm p)}{dx dQ^2} = A^i \left(Y_+ \tilde{F}_2^i \mp Y_- x \tilde{F}_3^i - y^2 \tilde{F}_L^i \right),
\tag{2.11}
$$

where $Y_\pm = 1 \pm (1-y)^2$ is called helicity factor and $i = NC, CC$ corresponds to a neutral or a charged current process. The $A^{(i)}$ coefficient functions

depend on the process

$$
\begin{aligned}
A^{NC} &= \frac{2\pi\alpha^2}{xQ^4}, \\
A^{CC} &= \frac{G_F^2}{4\pi x}\frac{M_W^4}{(Q^2 + M_W^2)^2}.
\end{aligned}
\tag{2.12}
$$

Here G_F is the Fermi coupling constant and α is the fine structure constant. $\tilde{F}_2, x\tilde{F}_3$ and $\tilde{F}_L$ are generalised structure functions, which take into account the lepton charge, helicity, exchange boson type and appropriate coefficients. In the formula above A^{NC} is given only for γ exchange. The coefficient function looks more complicated for Z exchange.

The structure functions can be measured from scattering experiments, since for given energies of the incoming particles the cross sections depend only on x and Q^2, which can be eventually reconstructed, see section 4.1.

2.3 The Quark Parton Model

The Quark Parton Model (QPM), introduced by Feynman, assumes that the proton is made of point-like constituents which are called partons [5]. The idea was based on experimental observation of Bjorken scaling [6]: by the end of the 60's in the electron-proton scattering experiment at Stanford Linear Accelerator Center (SLAC) [7,8] it was discovered that the structure function F_2 measured at a fixed value of x showed almost no dependence on the squared transferred momentum Q^2. The structure function seemed to depend only on the variable x. This behaviour was predicted by Bjorken and suggested that the proton is built of point-like particles, which correspond to partons introduced by Feynman.

In the Quark Parton Model the deep inelastic ep scattering cross section can be expressed as a sum of elastic electron-parton scattering processes. The probability to find a parton of certain flavour i that carries a fraction of the proton's momentum p in the interval of x and $x + dx$ is given by parton distribution functions (PDFs). The momentum fraction dp of the proton's momentum carried by these partons is given by $dp = xq_i(x)dx$. Since the naive QPM assumes that the proton consists of two up and one down valence quarks, the total momentum of the quarks inside the proton

should be 1. However this is inconsistent with experimental results [9] which show that quarks carry only half of the proton's momentum

$$\int_0^1 xu(x)dx + \int_0^1 xd(x)dx = 0.54. \tag{2.13}$$

From this it is concluded that half of the proton's momentum is carried by particles identified as gluons. Another inconsistency is the observation of the scaling violation of F_2, measured by different experiments. The scaling behaviour is observed only for values of about $x < 0.1$ and brakes for $x > 0.1$. The structure function F_2 as a function of Q^2 is shown in Figure 2.2 for different values of x. The plot shows measurements by the H1 experiment as well as some fixed target experiments. To explain the mentioned discrepancies the theory of Quantum Chromodynamics (QCD), described in the next section, is developed.

In addition to the constraint from momentum conservation, known as momentum sum rules, there are further constraints on the proton parton distribution functions. According to the QPM, the proton consists of two up and one down quark

$$\int_0^1 dx(u(x) - \bar{u}(x)) = 2,$$
$$\int_0^1 dx(d(x) - \bar{d}(x)) = 1, \tag{2.14}$$

where $u(x)$ ($\bar{u}(x)$) and $d(x)$ ($\bar{d}(x)$) are parton distribution functions of the (anti-)up type quark and (down-)quark respectively. These constraints are known as counting rules. Another constraint appears from the fact that the sum of the charges of the partons should be equal to the proton charge

$$\int_0^1 dx \left\{ \frac{2}{3} \left[u(x) - \bar{u}(x) \right] - \frac{1}{3} \left[d(x) - \bar{d}(x) \right] \right\} = 1. \tag{2.15}$$

2.4 Quantum Chromodynamics

The QPM does not consider the dynamics between quarks and bound states (hadrons). The field theory which describes strong interactions is called Quantum Chromodynamics (QCD) [12]. It assumes that quarks are point-like particles with 1/2 spin. They interact by an exchange of a massless gauge boson with spin 1, called gluons. Quarks and gluons have a
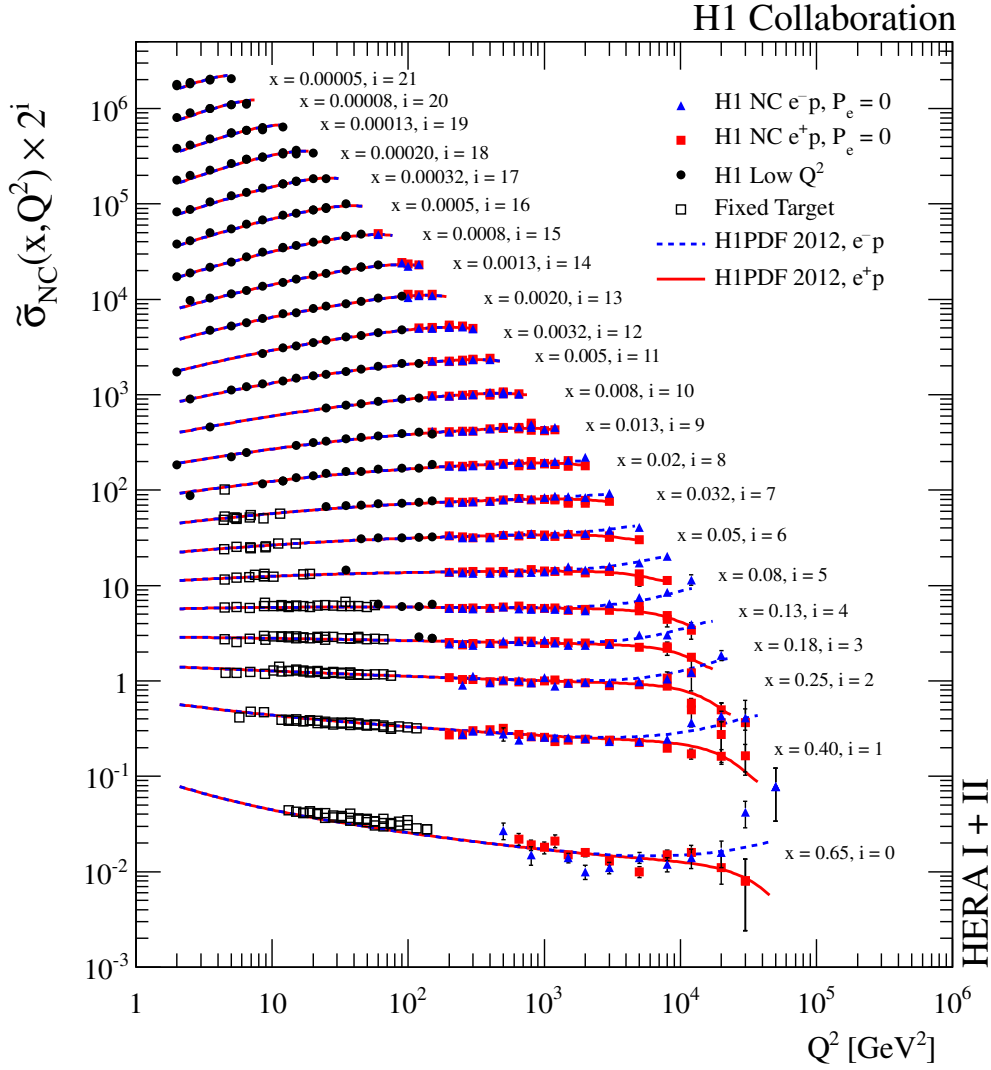
Figure 2.2: Combined HERA I+II unpolarised NC cross section as a function of Q^2 for different values of x. The triangles correspond to the $e^- p$ scattering, the solid squares correspond to $e^+ p$ scattering, the solid points correspond to low Q^2 data and the open squares correspond the measurements of the BCDMS experiment [10]. The theoretical expectations are given by the PDF fit H1PDF 2012. The plot is taken from [11].

quantum number called colour, which is described by the $SU(3)_C$ symmetry and can be represented by 3 colours red, green and blue. Quarks cannot exist as free particles, but only bound in colourless states. This effect is known as confinement. On the other hand at very high energies quarks and gluons interact very weakly and behave like free particles. This effect is called asymptotic freedom.

The interactions between quarks and gluons are described by a relativistic quantum field theory with non-Abelian gauge group $SU(3)_C$, which leads to some crucial differences between QCD and QED. In QCD gluons carry colour charge and thus can interact with each other, while this is not possible for photons in QED.

The strong interaction is characterised by the strong coupling constant α_s. In case of small values of α_s, perturbative expansions can be used to make the calculations. In lowest order α_s^0 corresponds to the Leading Order (LO) term, which does not account for any gluon vertices. In Next-to-Leading Order (NLO), interactions between quarks and gluons appear in the picture. The NLO corresponds to order α_s^1 in the perturbation series. One can go to higher orders by adding more gluon vertices. There is no common approach to make higher order calculations, instead there are various recipes. These theoretical calculations are quite challenging and usually are not higher in order than NNLO.

2.4.1 Renormalisation

At each vertex four-momentum is conserved. However, when going to higher orders, the momentum is no longer constrained in case of loops and boxes. The integration over all momentum space leads then to divergences if the momentum goes to infinity. In order to remove these divergences a procedure called renormalisation is used, which introduces a renormalisation scale μ^2 with a dimension of a mass squared. It turns out that for gauge theories all divergences cancel. However, if not all orders are included in this calculation the renormalised coupling α has a dependence on the renormalisation scale μ^2.

2.4.2 Running coupling constant

The physical observables should not depend on the arbitrary renormalisation scale, when calculated in all orders of perturbation theory. To insure, that the μ^2 dependence of any observable $R(Q^2/\mu^2, \alpha_s(\mu^2))$ cancels the following condition has to hold:

$$\mu^2 \frac{\partial R}{\partial \mu^2} + \mu^2 \frac{\partial \alpha_s}{\partial \mu^2} \frac{\partial R}{\partial \alpha_s} = 0. \tag{2.16}$$

This equation is called renormalisation group equation [13], from which the scale dependence of α_s can be calculated.

$$\alpha_s = \alpha_s(\mu^2) \left[1 - \frac{\alpha_s(\mu^2)}{12\pi}(33 - 2f) \ln(Q^2/\mu^2) + \ldots \right], \tag{2.17}$$

where f is the number of the flavours of quarks with masses smaller than Q^2. Since f can have a maximum value of 6, corresponding to the currently known types of quarks, the value of α_s drops with the increasing of Q^2. In the one-loop approximation the strong coupling constant is

$$\alpha_s(Q^2) = \frac{12\pi}{(33 - 2f) \ln(Q^2/\Lambda_{QCD}^2)}, \tag{2.18}$$

where Λ_{QCD} with a value of $300 - 500 \, \text{MeV}$ is a scale where the coupling α_s becomes large. In case of small values of Q^2, the increase of the α_s value results in confinement, while in case of large Q^2 values α_s becomes smaller leading to the asymptotic freedom.

2.4.3 Factorisation

The application of the QCD is limited to the short-distance region, where the perturbative QCD (pQCD) is used. At longer distances the DIS cross section cannot be calculated perturbatively due to large higher order corrections. The factorisation of the cross section into a short distance hard component calculable in pQCD, $\hat{\sigma}_i$, and long distance non-perturbative soft component $f_i(x, \mu_f)$ is called the factorisation theorem

$$\sigma_{ep} = \sum_i f_i(x, \mu_f) \otimes \hat{\sigma}_i. \tag{2.19}$$

The DIS electron proton cross section is calculated in pQCD with empirically parametrised parton densities $f_i(x, \mu_f)$, inside the proton. The parton densities are called parton distribution functions (PDF) and are determined experimentally. The factorisation is schematically shown in Figure 2.3 The
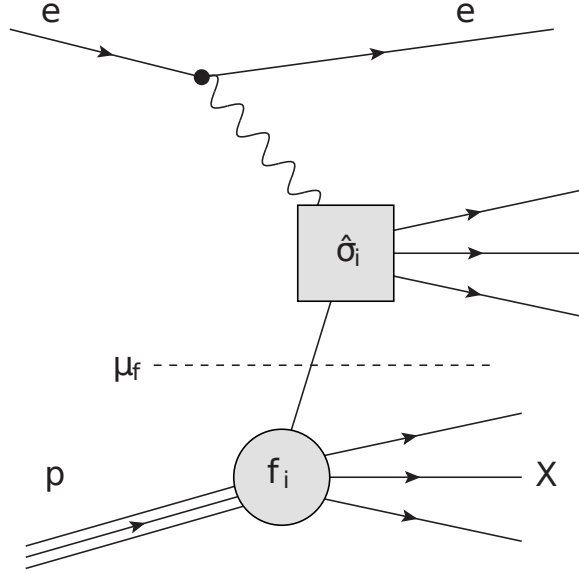
Figure 2.3: Schematic representation of factorisation. μ_f represents the factorisation scale, f_i corresponds to parton distribution functions and $\hat{\sigma}_i$ is the hard calculable part.

exact definitions of soft and hard pieces depend on the factorisation scheme and are matter of convention.

2.4.4 DGLAP evolution equations

The PDFs are determined from experiments, however the Q^2 dependence can still be calculated by the Dokshitzer-Gribov-Lipatov-Altarelli-Parisi (DGLAP) evolution equations [14–17]

$$\frac{\partial q(x,t)}{\partial t} = \frac{\alpha(t)}{2\pi} \int_x^1 \frac{dy}{y} \left[q(y,t) P_{qq}\left(\frac{x}{y}\right) + g(y,t) P_{qg}\left(\frac{x}{y}\right) \right], \qquad (2.20)$$

$$\frac{\partial g(x,t)}{\partial t} = \frac{\alpha(t)}{2\pi} \int_x^1 \frac{dy}{y} \left[q(y,t) P_{gq}\left(\frac{x}{y}\right) + g(y,t) P_{gg}\left(\frac{x}{y}\right) \right], \qquad (2.21)$$

where $t = \ln(Q^2/\Lambda_{QCD}^2)$ and P_{ij} are called splitting functions. They describe the probability of parton j with momentum fraction y to produce a parton i with momentum fraction x. For example in the case of the $q \to qg$ process the quark distributions are modified by splitting functions $P_{qq}(x/y)$ and $P_{qg}(x/y)$ and the splitting functions $P_{gg}(x/y)$ and P_{gq} correspond to the modification of gluon distributions. Figure 2.4 shows diagrams for each of this cases. The splitting functions are calculated perturbatively for a given

$$P_{qq}(x/y) \qquad P_{qg}(x/y) \qquad P_{gq}(x/y) \qquad P_{gg}(x/y)$$
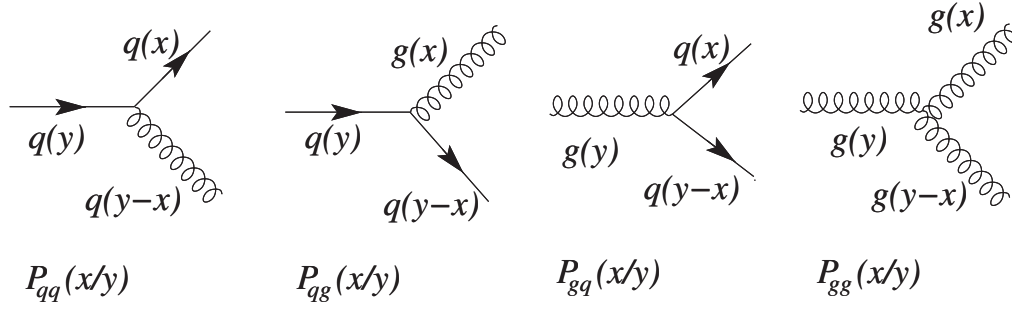
Figure 2.4: The splitting functions P_{ij}, corresponding to the probability of a parton j with momentum fraction y emitting a parton i with momentum fraction x.

factorisation scheme.

The evolution equations allow the PDFs measured at some fixed scale Q_0^2 to be evolved at given x to any Q^2 scale needed. Due to universality of the factorisation theorem, the PDFs extracted in any interaction, for instance ep, can be used in any other experiment involving proton, if the same factorisation and normalisation scheme is used.

2.4.5 QCD factorisation models

There are different approaches to factorise the structure functions into perturbatively calculable parts and soft parts (PDFs), and to take into account the production of heavy quarks in the calculations. In the following several pQCD schemes dealing with the higher order QCD calculations are briefly introduced.

2.4.5.1 Massless scheme

When dealing with the processes containing only light quarks, the masses of these quarks are assumed to be zero. They are considered to be active partons in the proton and their density distributions are used to describe the soft part of the calculation. However, this approximation does not always work in case of heavy quarks involved in the process. It is reasonable only in the cases, when factorisation scale μ_f is much larger than the mass of a heavy quark m_h. This approach is called massless or zero mass variable-flavour number scheme (ZM-VFNS) [18–22]. In this scheme the heavy quarks are treated as massless at the scale larger than the mass threshold m_h and infinitely massive below this threshold. The number of active partons in the proton increases by one as the scale passes the threshold m_h.

2.4.5.2 Massive scheme

Schemes that are treating the heavy quarks as massive at the scales $\mu_f \sim m_h$ are usually referred to as fixed-flavour number scheme (FFNS) [23, 24]. In FFNS the heavy quark contributions are included in the hard part of the cross sections. For the factorisation scale μ_f in the range of $m_h \sim \mu_f$, the production of the heavy quarks can be calculated from the hard process by including the heavy quark mass effects in the coefficient functions. This procedure is assumed to become unreliable for the scales $m_h \ll \mu_f$, since the increasing order in α_s contains large logarithms in the perturbative series.

Both VFNS and FFNS become equivalent, when the calculations are done for all orders in α_s.

2.4.5.3 ACOT scheme

The Aivazis-Collins-Olness-Tung (ACOT) scheme [25] provides a mechanism to account for the heavy quark masses in the theoretical calculations of heavy quark production. The scheme is an interpolation between the massless and massive schemes. In the limit of $\mu_f \sim m_h$, the ACOT scheme matches the FFNS, while in the limit of $m_h \ll \mu_f$ is the same as ZM-VFNS. The main ingredient provided by the ACOT scheme is the subtraction term,

which removes the double counting in the phase space regions where the LO and NLO contributions overlap. So at NLO the total result looks like

$$\sigma_{tot} = \sigma_{LO} + \{\sigma_{NLO} - \sigma_{sub}\}. \tag{2.22}$$

For the characteristic energy scale lower than a heavy quark mass $\mu_f < m_h$, the subtraction term is about the size of the LO term, which makes the total result $\sigma_{tot} \approx \sigma_{NLO}$. In case of the characteristic scale $\mu_f > m_h$, the dominant contribution to the result is made by σ_{LO} and the NLO contribution $\sigma_{NLO} - \sigma_{sub}$ is an $O(\alpha_s)$ correction.

2.4.5.4 Thorne-Roberts scheme

A scheme proposed by Thorne and Roberts (TR) [21, 26] is similar to the ACOT scheme. The main idea is for the structure functions to match the FFN for low Q^2 values and approximates the behaviour of the VFN scheme at high Q^2 region of the phase space. An additional condition in the TR scheme is that the derivatives of the structure functions in Q^2 should be continuous at the transition point.

It is expected that both TR and ACOT prescriptions should give the same results at high enough scales. An elaborate discussion of two scheme differences is discussed [27].

2.5 Neutral and charged current cross sections

In lowest order the neutral current cross section can be written as [28, 29]

$$\frac{d^2\sigma_{NC}^{\pm}}{dxdQ^2} = \frac{2\pi\alpha^2 Y_+}{xQ^4}\left(\tilde{F}_2 \mp \frac{Y}{Y_+}s\tilde{F}_3 - \frac{y^2}{Y_+}\tilde{F}_L\right), \tag{2.23}$$

where the $\pm$ sign corresponds to positron-proton and electron proton-scattering and α is the electromagnetic coupling constant. The generalised structure functions contain the information about the partonic structure of the proton.

The structure functions can be decomposed according to the contributions from pure γ exchange, pure Z change and from the interference γZ:

$$\tilde{F}_2^\pm = F_2^\gamma - (v_e \pm P_e a_e)k_Z F_2^{\gamma Z} + (v_e^2 + a_e^2 \pm P_e 2 v_e a_e)k_Z^2 F_2^Z, \qquad (2.24)$$

$$x\tilde{F}_3^\pm = -(a_e \pm P_e v_e)k_Z x F_2^{\gamma Z} + (2a_e v_e \pm P_e(v_e^2 + a_e^2))k_Z^2 x F_3^Z, \qquad (2.25)$$

where P_e can take values in the range of $[-1, +1]$ and corresponds to the longitudinal polarisation of the incoming lepton. In case of a left-handed lepton $P_e = -1$ while in case of $P_e = +1$ the lepton is right-handed. The factor k_Z indicates the ratio of the couplings and propagators of the Z^0 to the ones from the photon

$$k_z = \frac{1}{4\sin^2(\Theta_W)\cos^2(\Theta_W)}\frac{Q^2}{Q^2 + M_Z^2} \approx 1.41\frac{Q^2}{Q^2 + M_Z^2}. \qquad (2.26)$$

The exchanged boson couples to the interacting fermions via vector(axial) couplings $v_f(a_f)$. The couplings are defined using the third component of the weak isospin of the fermion $T_{3,f}$ and the Weinberg angle Θ_W

$$\begin{aligned} v_f &= T_{3,f} - 2e_f \sin^2(\Theta_W), \\ a_f &= T_{3,f}. \end{aligned} \qquad (2.27)$$

The structure functions $F_2^\gamma, F_2^{\gamma Z}$ and F_2^Z in LO in QPM are expressed as a sum of quark and anti-quark distributions

$$[F_2^\gamma, F_2^{\gamma Z}, F_2^Z] = \sum_i [e_i^2, 2e_i a_i, v_i^2 + a_i^2] x[q_i(x) + \bar{q}_i(x)] \qquad (2.28)$$

where the sum runs over the quark flavours i. Similarly for $xF_3^{\gamma Z}, xF_3^Z$

$$[xF_3^{\gamma Z}(x), xF_3^Z(x)] = \sum_i [2e_i a_i, 2v_i a_i] x[q_i(x) - \bar{q}(x)]. \qquad (2.29)$$

The measurement of all three structure functions is possible at HERA. The dominant contribution in the whole kinematic range is coming from $\tilde{F}_2$. Though the QPM predicts the F_L to be 0, in higher order QCD calculations allow a non-zero F_L, which is confirmed experimentally. The $\tilde{F}_L$ contribution is coming from gluons at the region of low x. The measurement of $x\tilde{F}_3$ is possible by comparing e^+p/e^-p scattering at HERA.

The charged current cross section can be presented in a similar form as the

neutral current cross section,

$$\frac{d^2\sigma^{e^\pm p}}{dxdQ^2} = (1 \pm P_e)\frac{G_F^2}{4\pi x}\left(\frac{M_W^2}{M_W^2 + Q^2}\right)^2 \left(W_2^\pm \mp \frac{Y_-}{Y_+}xW_3^\pm - \frac{y^2}{Y_+}W_L^\pm\right), \quad (2.30)$$

where G_F is the Fermi constant and is related to the electromagnetic and weak couplings

$$G_F = \frac{g^2}{4\sqrt{2}M_W^2}. \quad (2.31)$$

The structure functions $\tilde{W}_2, x\tilde{W}_3, \tilde{W}_L$ are analogous to the neutral current structure functions, but they do not contain electromagnetic and interference terms, since the charged current process is a purely electroweak process.

In the QPM, where $W_L^\pm = 0$, the structure functions can be expressed as a sum of quark-antiquark momentum differences

$$\tilde{\sigma}_{CC}^- = (xu + xc) + (1-y)^2(x\bar{d} + x\bar{s}), \quad (2.32)$$

$$\tilde{\sigma}_{CC}^+ = (x\bar{u} + x\bar{c}) + (1-y)^2(xd + xs). \quad (2.33)$$

From the equations above, one can see that the main contribution to the cross section at high x comes from the u quark for an electron beam and from the d in case of a positron beam. Therefore the CC cross section with different lepton beams allows to separate u and d valence quarks.

The Standard Model predicts unification of the electromagnetic and weak interactions. This is nicely illustrated in Figure 2.5, where H1 measurements of NC and CC cross sections over a large range of Q^2 are shown. Due to the heavy propagator mass, the CC cross section is suppressed for Q^2 values up to $10^4\,\mathrm{GeV}^2$ relative to the NC process. Both processes become compatible in size for $Q^2 > M_W^2$.

2.5.1 Alternative representation of the structure functions

In section 2.6 the contact interaction framework is introduced. In this framework the structure functions are modified by an additional contact term in the vector and axial couplings. For presentation convenience the
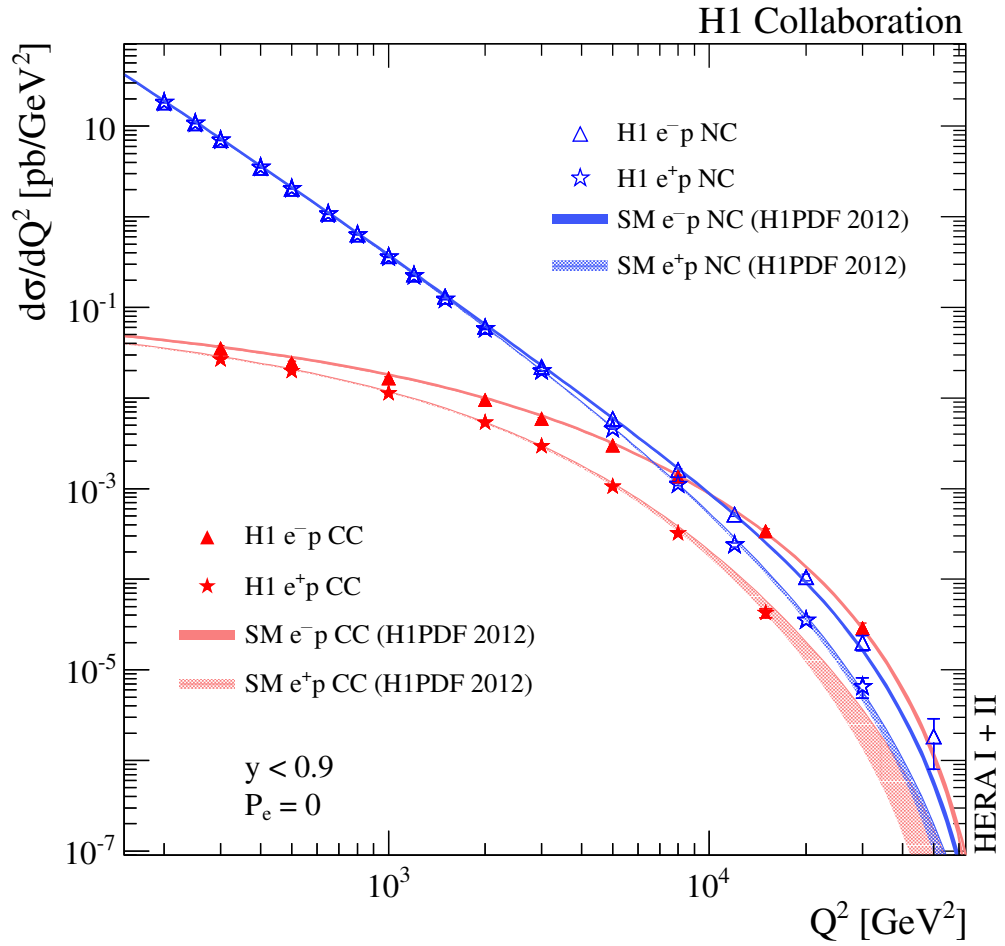
Figure 2.5: Q^2 dependence of the NC and CC cross sections $d\sigma/dQ^2$ for the combined HERA I+II unpolarised e^-p and e^+ data. The plot is taken from [11].

structure functions are separated according to the chirality of the lepton

$$\tilde{F}_2^{L,R}(x,Q^2) = x\sum_i [(V_i^{L,R}(Q^2))^2 + (A_i^{L,R}(Q^2))^2] \\ \times \{q_i(x,Q^2) + \bar{q}_i(x,Q^2)\}, \tag{2.34}$$

$$x\tilde{F}_3^{L,R}(x,Q^2) = \mp x\sum_i [-P_e 2V_i^{L,R}(Q^2)A_i^{L,R}(Q^2)] \\ \times \{q_i(x,Q^2) - \bar{q}_i(x,Q^2)\}, \tag{2.35}$$

where V_i and A_i are the vector and axial couplings

$$V_i^{L,R}(Q^2) = e_i - (v_e \pm P_e a_e)v_i k_Z(Q^2), \\ A_i^{L,R}(Q^2) = -(v_e \pm P_e a_e)a_i k_Z(Q^2). \tag{2.36}$$

2.5.2 Reduced and single differential cross section

For the convenience of presentation, the reduced cross section is introduced. For the NC the reduced cross section $\tilde{\sigma}_{NC}^{\pm}$ is defined as

$$\tilde{\sigma}_{NC}^{\pm}(x,Q^2) = \tilde{F}_2(x,Q^2) \mp \frac{Y_-}{Y_+}x\tilde{F}_3(x,Q^2) - \frac{y^2}{Y_+}\tilde{F}_L(x,Q^2). \tag{2.37}$$

For most of the kinematic region $\sigma\tilde{}_{NC}$ is essentially equal to the $\tilde{F}_2$ structure function.

The reduced CC cross section is presented as

$$\tilde{\sigma}_{CC}^{\pm} = \frac{G_F^2}{2\pi x}\left(\frac{M_W^2}{Q^2 + M_W^2}\right)^2 \frac{d^2\sigma^{\pm}}{dxdQ^2}. \tag{2.38}$$

The propagator terms and the couplings are divided out, which allows to see the effects of the parton distribution functions alone.

The single differential cross section as a function of Q^2 is extracted by integrating Equation 2.23 for neutral current or Equation 2.30 for charged current over the allowed kinematic phase space in x

$$\frac{d\sigma}{dQ^2} = \int_x \frac{d^2\sigma}{dxdQ^2}dx. \tag{2.39}$$

In the same way one can define the single differential cross section as a function of x

$$\frac{d\sigma}{dQ^2} = \int_{Q^2} \frac{d^2\sigma}{dxdQ^2} dQ^2.$$

(2.40)

2.5.3 Radiative corrections

The cross sections discussed previously are in leading-order (LO) $\mathcal{O}(\alpha_{em})$. However, higher orders in α_{em} also contribute by the exchange of additional bosons or by self energies. Therefore the measurements have to be corrected for these effects. The corrections are of two types: purely electroweak corrections, arising from vertex correction and propagators and QED corrections from the photon radiation in the initial and final states. The emission of the real photon changes the *ep* centre of mass energy and thus the kinematics of the event is also changed. QED radiation is then causing shifts in the reconstructed kinematic variables depending on the reconstruction method, described in the section 4.1. An example of QED
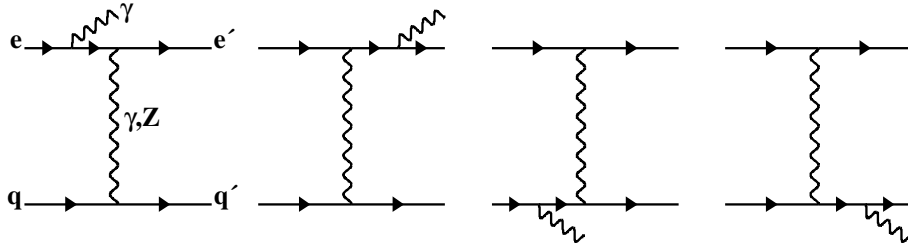
Figure 2.6: Illustration of QED corrections for the case of NC DIS with radiation of a photon from the lepton or the quark in the initial or final state.
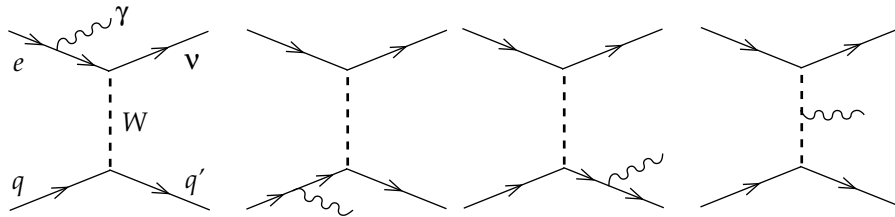
Figure 2.7: Illustration of QED corrections for the case of CC DIS with radiation of a photon from the lepton or the quark in the initial or final state.

corrections for neutral current and charged current are shown in Figure 2.6 and Figure 2.7 respectively.

2.6 Physics beyond the Standard Model

The measurement of the DIS ep cross section up to the highest achievable momentum transfer Q^2 is a sensitive probe to check the predictions of the Standard Model (SM). On the other hand, the same processes can be used to look for evidence of new phenomena. Significant deviations of cross sections measurements from the SM predictions may provide a hint for so far undiscovered physical phenomena. The measurement of the neutral current cross sections is preformed for four-momentum transfers up to about $Q^2 \approx 50000\,\text{GeV}^2$. This corresponds to a spatial resolution according to the Heisenberg uncertainty principle of

$$\delta x \approx \frac{\hbar c}{\sqrt{Q^2}} \approx \frac{200\,\text{GeV} \cdot 10^{-18}\,\text{m}}{\sqrt{50000\,\text{GeV}^2}} \approx 0.9 \times 10^{-18}\,\text{m}. \qquad (2.41)$$

In order to access the region beyond the centre of mass energy provided by the HERA collider, the concept of four fermion contact interactions can be used.

2.6.1 General contact interactions

The search for new physics effects beyond the Standard Model can follow two strategies. On the one hand there is the possibility for the direct search for new resonances by determining the invariant mass of final state objects and by looking for a characteristic resonance curve in the mass spectrum. Direct searches however, are limited by the centre of mass energy, since the resonance mass of the produced particle cannot exceed that energy. An access to a much larger mass range, on the other hand, is possible via the investigation of possible effects due to the virtual exchange of new, heavy particles. Those indirect effects can be described in analogy to Fermi's interpretation of weak interactions [30]. In low energy approximation the effects from particles with mass scales much larger than the centre of mass energy $\sqrt{s} \ll \Lambda$, are described as four-fermion point-like contact interaction. In Figure 2.8 an example of Feynman diagrams and the low energy approximation is shown. The general contact-interaction terms are
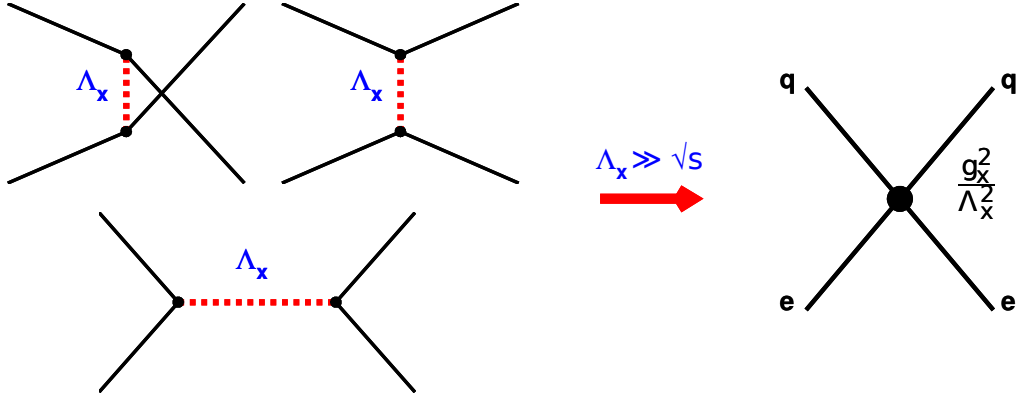
Figure 2.8: Feynman diagrams for new types of interactions and the low energy approximation as an effective four-fermion contact interaction with a coupling g_X^2/Λ_X^2.

added to Standard Model Lagrangian to form an effective theory

$$\mathcal{L} = \mathcal{L}_{SM} + \mathcal{L}_{CI}. \tag{2.42}$$

The contact interaction Lagrangian is composed of three possible Lorentz invariant fermion bilinear combinations, which can be scalar, vector or tensor. However, the contributions of scalar and tensor terms are strongly suppressed at HERA [31] and are not taken into consideration in the current analysis. The contact interaction Lagrangian then takes the form [32–34]

$$\mathcal{L}_{CI} \approx \mathcal{L}_{vector} = \sum_q \sum_{a,b} [\eta_{ab}^q (\bar{e}_a \gamma_\mu e_a)(\bar{q}_a \gamma^\mu e_q)], \tag{2.43}$$

where the indices a, b correspond to the left or right-handed fermion helicities, the first sum runs over the quark types and η_{ab}^q is the coupling coefficient that corresponds to the contact interaction. The coefficient has the dimension of an inverse mass squared and can be represented as

$$\eta_{ab}^q \equiv \epsilon_{ab}^q \frac{g^2}{\Lambda_{ab}^q}, \tag{2.44}$$

where g is the overall coupling strength. $\epsilon_{ab}^q = \pm 1$ corresponds to positive or negative interference with the Standard Model amplitude and Λ is the scale of the contact interaction.

The contributions from possible $eeqq$ contact interactions modify the Stan-

dard Model electroweak couplings for neutral current. By introducing the additional terms in Equation 2.34 and Equation 2.35 one obtains for the $A_i^{L,R}$ and $V_i^{L,R}$

$$
\begin{aligned}
V_i^L(Q^2) &= e_i - (v_e \mp P_e a_e)v_i k_Z(Q^2) + \frac{Q^2}{2\alpha}(\eta_{LL}^i + \eta_{LR}^i), \\
V_i^R(Q^2) &= e_i - (v_e \pm P_e a_e)v_i k_Z(Q^2) + \frac{Q^2}{2\alpha}(\eta_{RL}^i + \eta_{RR}^i), \\
A_i^L(Q^2) &= -(v_e \pm P_e a_e)a_i k_Z(Q^2) + \frac{Q^2}{2\alpha}(\eta_{LL}^i - \eta_{LR}^i), \\
A_i^R(Q^2) &= -(v_e \pm P_e a_e)a_i k_Z(Q^2) + \frac{Q^2}{2\alpha}(\eta_{RL}^i - \eta_{RR}^i),
\end{aligned}
\tag{2.45}
$$

where the $\pm$ and $\mp$ signs correspond to positron and electron beams. The modified cross section as a function of new coupling coefficient η is obtained from Equation 2.23, 2.34, 2.35 and 2.45.

At HERA, the contributions of the second and third quark generation to the cross section are significantly suppressed. Since the largest contributions are resulting from the u and d quark distributions, for the contact interaction coefficients only up and down type couplings are distinguished

$$
\eta_{ab}^u \equiv \eta_{ab}^u = \eta_{ab}^c, \tag{2.46}
$$

$$
\eta_{ab}^d \equiv \eta_{ab}^d = \eta_{ab}^s = \eta_{ab}^b. \tag{2.47}
$$

The top quark has no contribution at HERA due to its high mass and is not taken into consideration. The four helicity combinations of two quark types allows for a variety of models. Various kinds of new physics processes, e.g. compositeness of quarks, leptoquarks, large extra dimensions or any other new interactions mediated by heavy particles can be described in the CI framework and be constructed via appropriate choice of the η couplings.

2.6.2 Compositeness

In compositeness [35] scenarios quarks and leptons are no longer regarded as structureless, but rather composite objects built up of more fundamental constituents. Those are bound together by a new force, which is probably confined and becomes strong at a scale Λ. In order to investigate the compositeness effect at available energies considerably below Λ, the formalism of contact interactions can be used [33,34]. These effects can be expressed via

the effective coupling η as shown in Equation 2.44. The coupling strength is by convention chosen as $g = 4\pi$, both interference signs are considered. The scale Λ is assumed to be the same for all up and down-type quarks. There can be various models constructed assuming different chiral structures for the η coupling. The models are specified by the values of the coefficient ϵ. The models considered in the current analysis are summarised in Table 2.1. The coefficient ϵ, is basically showing the effective modification of the SM

Coupling	ϵ_{LL}	ϵ_{LR}	ϵ_{RL}	ϵ_{RR}
LL	±1	0	0	0
LR	0	±1	0	0
RL	0	0	±1	0
RR	0	0	0	±1
VV	±1	±1	±1	±1
AA	±1	∓1	∓1	±1
VA	±1	∓1	±1	∓1
$LL + RR$	±1	0	0	±1
$LR + RL$	0	±1	±1	0

Table 2.1: Chiral structures of different contact interaction scenarios. The $\pm$ sing correspond to different interference signs with the Standard Model amplitudes.

vector and axial couplings in Equation 2.45. For example, in case of the LL model $\epsilon_{LL} = \pm1$ the contact term contributes only to V^L and A^L by an additional term $\frac{Q^2}{2\alpha}\eta_{LL}$, while the other terms are set to zero.

2.6.3 Leptoquarks

Leptoquarks (LQ) appear in various extensions of the Standard Model, which try to establish a connection between leptons and quarks [36]. Leptoquarks combine properties and quantum numbers of leptons and quarks. The leptoquarks have the following properties:

- They are bosons with spin 1 or 0.

- Leptoquarks carry colour charge.

- The electrical charge of LQs is fractional.

- They carry both lepton and baryon numbers, which define an additional quantum number called fermion number F as $F = L + 3B$.

Leptoquarks that couple to e^+q have a fermion number of $F = 0$ and those coupling to e^-q have a fermion number of $F = 2$. In Figure 2.9 possible channels of leptoquark production in $e^{\pm}q$ interactions are shown. In
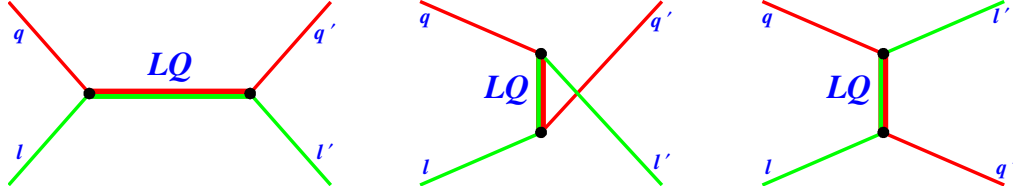
Figure 2.9: Possible scenarios of leptoquark production in lepton-quark interaction (s-, u- and t-channel).

order to describe leptoquarks Buchmüller, Rückl and Wyler [37] introduced an effective Lagrangian, which conserves the baryon and lepton numbers and is invariant with the respect to the Standard Model transformations $SU(3)_c \times SU(2)_L \times U(1)_Y$.

If the masses of leptoquarks are above of the available centre of mass energy, the effects due to the virtual exchange, can be described similarly to the compositeness scenarios. An effective low-energy approximation can be parametrised by contact interactions terms. The coupling coefficient η is related to leptoquark the mass M_{LQ} and the Yukawa coupling λ

$$\eta^q_{ab} = \epsilon^q \frac{\lambda^2}{M^2_{LQ}}. \tag{2.48}$$

According to the Buchmüller-Rückl-Wyler (BRW) framework there are 14 different types of leptoquarks. Their production and decay modes are fixed. So in contrast to the compositeness models the interference and the relative contribution ϵ^q_{ab} for each type leptoquark is clearly established [38]. The only free parameter is then the ratio λ/M_{LQ}. Table 2.2 gives an overview of the investigated leptoquark types.

LQ	ϵ_{ab}^u	ϵ_{ab}^d	F
S_0^L	$\epsilon_{LL}^u = +\frac{1}{2}$		2
S_0^R	$\epsilon_{RR}^u = +\frac{1}{2}$		2
$\tilde{S}_0^R$		$\epsilon_{RR}^d = +\frac{1}{2}$	2
$S_{1/2}^L$	$\epsilon_{LR}^u = -\frac{1}{2}$		0
$S_{1/2}^R$	$\epsilon_{RL}^u = -\frac{1}{2}$	$\epsilon_{RL}^d = -\frac{1}{2}$	0
$\tilde{S}_{1/2}^L$		$\epsilon_{LR}^d = -\frac{1}{2}$	0
S_1^L	$\epsilon_{LL}^u = +\frac{1}{2}$	$\epsilon_{LL}^d = +1$	2
V_0^L		$\epsilon_{LL}^d = -1$	0
V_0^R		$\epsilon_{RR}^d = -1$	0
$\tilde{V}_0^R$	$\epsilon_{RR}^u = -1$		0
$V_{1/2}^L$		$\epsilon_{LR}^d = +1$	2
$V_{1/2}^R$	$\epsilon_{RL}^u = +1$	$\epsilon_{RL}^d = +1$	2
$\tilde{V}_{1/2}^L$	$\epsilon_{LR}^u = +1$		2
V_1^L	$\epsilon_{LL}^u = -2$	$\epsilon_{LL}^d = -1$	0

Table 2.2: Leptoquark classification according to the BRW framework.

2.6.4 Large extra dimensions

Trying to unify electromagnetism and general gravity Kaluza and Klein (KK) postulated an additional spatial dimension [39]. This dimension has to be cylindrically compactified with radius R in order to be consistent with the observations like Newton's law of gravity. Much later Arkani-Hamed, Dimopoulos and Dvali (ADD) [40] proposed a model of large extra dimensions. They introduced extra n spatial dimensions with sizes much bigger than the electroweak scale. The SM particles are bound to 4-dimensional space, while the graviton is propagated to the extra dimensions decreasing the strength of the gravitational field in our space. The Plank scale $M_P \sim 10^{19}$ GeV in a 4-dimensional world becomes an effective scale arising from the fundamental scale M_D in $4 + n$ dimensions. The scales are related by

$$M_P^2 \sim R^n M_D^{2+n}. \tag{2.49}$$

Here R is the compactification radius R and n is the number of dimensions. For the compactification radius $R \sim 1$ mm and $n = 2$, the scale M_D can be of TeV order. The contribution from the graviton exchange in the extra dimensions can be described as an effective CI theory with an effective coupling [41]

$$\eta = \frac{\lambda}{M_S^4}. \tag{2.50}$$

Here M_S is an ultraviolet cut-off scale, taken to be equal to M_D. The coefficient λ depends on details of the theory and is taken here to be ± 1. To account for the effects due to graviton exchange, the SM $eq \to eq$ cross section has to be modified [41]

$$\frac{d\sigma}{d\hat{t}} = \frac{d\sigma^{SM}}{d\hat{t}} + \frac{d\sigma^G}{d\hat{t}} + \frac{d\sigma^{\gamma G}}{d\hat{t}} + \frac{d\sigma^{ZG}}{d\hat{t}}, \tag{2.51}$$

where G indicates the contribution from pure graviton exchange, γG corresponds to the interference between photon and graviton and ZG accounts for the interference of Z boson and graviton. The modification is usually presented in terms of Mandelstam variables [42] $\hat{t}, \hat{s}$ and $\hat{u}$ [2]. The

---

[2]Those variables are basically Lorenz invariant combinations of the 4-momenta of all particles in $eq \to eq$ or any other 2 particles $\to$ 2 particles process.

contributions have the following form

$$\frac{d\sigma^G}{d\hat{t}} = \frac{\pi\lambda^2}{32M_S^8}\frac{1}{\hat{s}}[32\hat{u}^4 + 64\hat{u}^3\hat{t} + 42\hat{u}^2\hat{t}^2 + 10\hat{u}\hat{t}^3 + \hat{t}^4],$$

$$\frac{d\sigma^{\gamma G}}{d\hat{t}} = \mp\frac{\pi\lambda}{2M_S^4}\frac{\alpha e_q}{\hat{s}^2}\frac{(2\hat{u}+\hat{t})^3}{\hat{t}}, \tag{2.52}$$

$$\frac{d\sigma^{ZG}}{d\hat{t}} = \frac{\pi\lambda}{2M_S^4}\frac{\alpha}{\hat{s}^2\sin^2 2\Theta_W}\left[\pm v_e v_q\frac{(2\hat{u}+\hat{t})^3}{\hat{t}-M_Z^2} - a_e a_q\frac{\hat{t}(6\hat{u}^2+6\hat{u}\hat{t}+\hat{t}^2)}{\hat{t}-M_Z^2}\right].$$

2.6.5 Form factor of the quark

The Standard Model assumes fermions to be point-like particles, having neither a substructure nor a spatial extension. In case of finite spatial size of leptons or quarks, deviations of the inclusive cross section from the Standard Model predictions can be expected, since the exchange of the bosons is sensitive to the electroweak charge distributions of the interacting particles [43]. The simplest way to parametrise such discrepancies is to introduce a classical form factor, $f(Q^2)$, which describes a reduction of the cross section as a function of the Q^2

$$f_q(Q^2) = 1 - \frac{1}{6}\langle r^2\rangle Q^2, \tag{2.53}$$

$$\frac{d\sigma}{dQ^2} = \frac{d\sigma_{SM}}{dQ^2}f_q^2(Q^2), \tag{2.54}$$

where f_q corresponds to the form factor of an interacting quark. The radius of the quark is defined as the root of the mean squared radius of the electroweak charge distribution $R = \sqrt{\langle r^2\rangle}$. The higher order terms in the formula above are neglected. The form factor of the electron is considered to be equal to 1, since the current experimental limits are out of achievable sensitivity at HERA.

Chapter

3

The H1 experiment at HERA

The presented analysis is based on the data taken by the H1 experiment at the HERA (Hadron Elektron Ring Anlage) electron-proton collider during its operation time from 1994 until 2007. This chapter contains a brief description of the HERA accelerator and the most important H1 detector components.

The HERA accelerator, the world's only electron-proton collider, is located at the DESY (Deutsches Elektronen-Synchrotron) laboratory in Hamburg. It has two separate storage rings for electrons (or positrons) and protons with circumferences of about 6.3 km. The electrons and protons are accelerated to an energy of 27.5 GeV and 920 GeV (820 GeV before 1998) respectively. By the end of the operation period, HERA accelerated the proton beams to lower energies of 460 GeV and 575 GeV in order to measure the longitudinal structure function F_L. The schematic view of the HERA accelerator is shown in Figure 3.1. The beams collide in two interaction points at the center-of-mass energy $\sqrt{s} \approx 318$ GeV (301 GeV before 1998). Two collider experiments H1 [1] and ZEUS [2] are located in the northern and southern interaction regions. The H1 detector is described in more details in the next section. In addition there are two fixed target experiments HERMES [44] and HERA-B in the eastern and western parts of HERA. The operation of
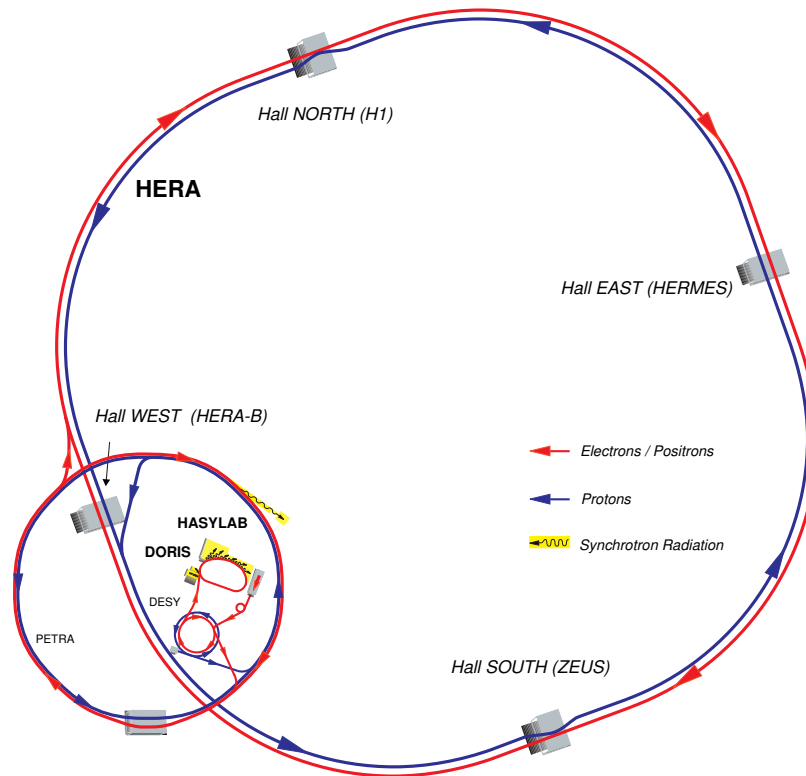
Figure 3.1: Schematic view of the HERA accelerator and its detectors.

HERA was divided in two phases. The first period between 1991 and 2000 (HERA I) was followed by an upgrade of the collider from 2000 to 2003 and the second operation period lasted from 2003 until 2007. New focusing magnets were installed during the luminosity upgrade inside the detectors in order to increase the instantaneous luminosity L which is defined in terms of accelerator quantities as

$$L = \frac{f N_e N_p}{4\pi \sigma_x \sigma_y},$$ (3.1)

where f is the bunch crossing frequency, N_e and N_p are the number of electrons and protons per bunch and σ_x and σ_y are the Gaussian transverse beam profiles in the x and y directions at the interaction point.

The luminosity accumulated over a period of time T is denoted as integrated

luminosity

$$\mathcal{L} = \int_0^T L(t)dt.$$

On the other hand, in terms of particle interactions the integrated luminosity is a coefficient of proportionality relating a specific cross section σ to the number of observed events of this type N

$$\sigma \sim \frac{N}{\mathcal{L}}.$$

The integrated luminosity collected by the H1 detector during its operation time from 1992 until 2007 as a function of operation time for both running periods is shown in Figure 3.2. The effect of the luminosity upgrade is well visible in the plot by the steep rise of the HERA II luminosity curve.
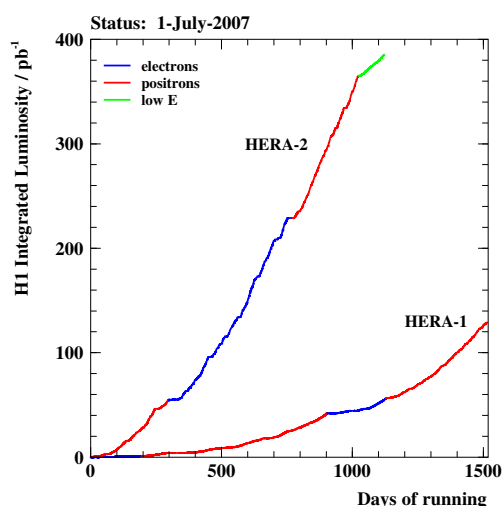
Figure 3.2: H1 integrated luminosity by the end of July 2007 as a function of the operation time for the HERA I and HERA II running periods.

In addition to the luminosity upgrade there were spin rotators installed around the interaction regions during the shut down between 2000 and 2003. This allows to provide longitudinally polarised lepton beams to the H1 and ZEUS experiments. During the shut down period the experiments were also upgraded and new components of detectors were installed.

3.1 The H1 detector

H1 is a multipurpose detector [1], which is designed to study electron-proton interactions at HERA. Due to the large difference in the energies of the lepton and proton beams the production of the particles in *ep* collision at HERA is boosted in the direction of the outgoing proton. This direction has enhanced instrumentation and is called forward direction. The H1 coordinate system is defined as a right-handed system with the x axis pointing to the centre of the HERA ring, the y axis in the upwards direction and the z axis is chosen along the beam of the protons. The origin of the coordinate system corresponds to the nominal interaction point. The polar angle θ is defined with respect to the z axis and the azimuthal angle ϕ is defined with respect to the x axis.

Figure 3.3 shows a schematic view of the H1 detector. The detector is composed of central $\boxed{2}$ and forward $\boxed{3}$ tracking chambers, which are used to record tracks of charged particles and to reconstruct the interaction point. The tracking system is surrounded by the Liquid Argon (LAr) calorimeter. The LAr calorimeter is used to measure the energy of particles in almost all solid angles. It consists of an electromagnetic $\boxed{4}$ and a hadronic $\boxed{5}$ part. The LAr calorimeter is surrounded by a superconducting coil $\boxed{6}$, which provides a magnetic field of 1.15 T. The charged particles are deflected in the magnetic field, which allows to determine their charge, as well as their momenta from the curvature.

The Spaghetti Calorimeter (SpaCal) $\boxed{12}$ is installed in the backward direction and allows detection of the scattered beam electron. The forward region is covered by the PLUG calorimeter. The Iron yoke $\boxed{10}$ is surrounded by the instrumentation responsible for muon detection, the Central Muon Detector (CMD). The components of the detector the most relevant for the neutral and charged current cross section measurement are described in more details in the followed subsections.

3.1.1 The calorimeters

The H1 detector contains four calorimeter systems in total:

- The central and forward region are covered by the Liquid Argon calorimeter.

HERA Experiment H1

1	Beam pipe and beam magnets
2	Central tracking chambers
3	Forward tracking and Transition radiators
4	Electromagnetic Calorimeter (lead)
5	Hadronic Calorimeter (stainless steel)
6	Superconducting coil (1.2T)
7	Compensating magnet
8	Helium cryogenics

Liquid Argon

9	Muon chambers
10	Instrumented Iron (iron stabs + streamer tube detectors)
11	Muon toroid magnet
12	Warm electromagnetic calorimeter
13	Plug calorimeter (Cu, Si)
14	Concrete shielding
15	Liquid Argon cryostat

Figure 3.3: Schematic representation of the H1 detector with subdetector components.

- The PLUG calorimeter is complementing the gap between the LAr calorimeters and the beam pipe in the forward direction.

- The Spaghetti Calorimeter (SpaCal) covers for the backward direction.

- The Tail Catcher is measuring the energy that leaks out of the LAr and SpaCal calorimeters.

3.1.1.1 The Liquid Argon calorimeter

The Liquid Argon (LAr) calorimeter [45] covers the angular range of $4° \lesssim \theta \lesssim 153°$, which corresponds to the central and forward region. The liquid argon technique provides good stability of the system, homogeneity of response, high granularity and is easy to calibrate. This allows a precise identification of the beam electron and a measurement of its energy and position. The calorimeter consists of an electromagnetic section followed by a hadronic one. It is divided into eight self-supporting wheels along the beam axis (z axis). They are named according to their position: Backward Electromagnetic Barrel (BBE), Central Barrels (CB1, CB2, CB3), Forward Barrels (FB1, FB2), Inner and Outer Forward Barrels (IF1, IF2 and OF1, OF2). Except for the BBE, which consists of only an electromagnetic part and the IF2/OF2, which have only a hadronic part the rest of the wheels contain a hadronic and an electromagnetic section. Each of the wheels is divided into eight identical octants in the ϕ-direction. The octants are segmented into cells, which form the smallest structure for the measurement of a particle shower from an incident particle. The information from each cell is then digitalized separately. The inactive zones of the calorimeter between the wheels are called z-cracks and those between the octants ϕ-cracks. The longitudinal and transverse view of the LAr calorimeter are shown in Figure 3.4 and Figure 3.5, where all the mentioned characteristics are well visible.

The LAr calorimeter consists of layers of steel and lead, which act as passive absorber. The space between those absorber plates is filled with liquid argon, used as the active material. The absorber plates are oriented such that the angle of incidence of particles from the ep interaction point is larger than $45°$. In the electromagnetic cells the lead absorber is $4\,\mathrm{mm}$ thick and the thickness of the active material is about $2.35\,\mathrm{mm}$. The hadronic part consists of $19\,\mathrm{mm}$ steel layers and $2.4\,\mathrm{mm}$ liquid argon gaps. There are 3
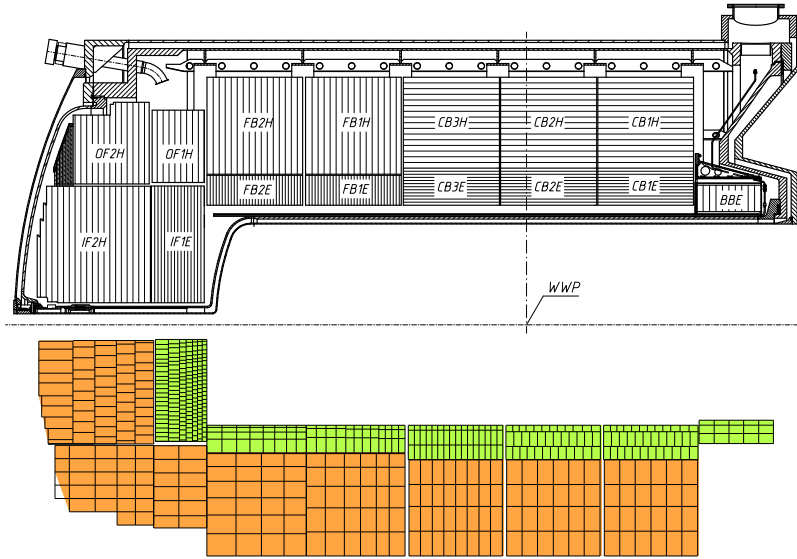
Figure 3.4: Longitudinal view of the Liquid Argon calorimeter. The upper part shows the wheel structure with the orientation of the absorber plates, indicated by horizontal and vertical lines respectively. The structure in cells is presented in the lower part.

to 4 layers in the electromagnetic part and 5 to 8 layers in the hadronic part.

The LAr calorimeter is non-compensating, i.e. the response of the detector to electromagnetic and hadronic showers is different. For the hadronic shower the response is about 30% smaller. Different methods on correcting for this difference are described elsewhere [46].

The energy resolution of the Liquid Argon calorimeter for the electrons and photons is

$$\frac{\sigma_{em}}{E} = \frac{12\%}{\sqrt{E(GeV)}} \oplus 1\%,$$

and for hadrons:

$$\frac{\sigma_{had}}{E} = \frac{50\%}{\sqrt{E(GeV)}} \oplus 2\%,$$

as measured in test beams [45, 47].
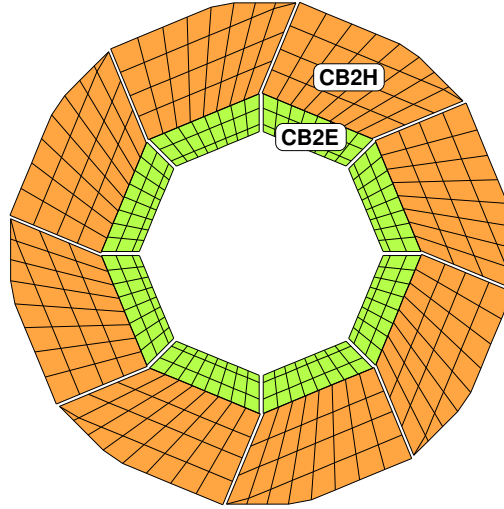
Figure 3.5: Transversal cross section of the CB2 wheel of the Liquid Argon calorimeter subdivided into the electromagnetic part (CB2E) and hadronic part (CB2H). The wheel is divided into eight octants. Only the cracks between electromagnetic parts point to the nominal interaction point.

3.1.1.2 The Spaghetti Calorimeter

The Spaghetti Calorimeter (SpaCal) [48] covers the backward region ($153° \lesssim \theta \lesssim 177.5°$). The SpaCal calorimeter consists of an inner electromagnetic and an outer hadronic part. Like the LAr calorimeter the SpaCal calorimeter is also non-compensating. The main purpose of this calorimeter is to detect the angle and the energy of the scattered beam electrons. The electromagnetic part is made of 0.5 mm thick scintillating plastic fibres. The hadronic section consists of 1.0 mm thick plastic fibres. In both parts the scintillating fibres are incorporated in a lead matrix, where the incident particle creates an electromagnetic or a hadronic shower. Scintillation light is emitted by the fibres, when the charged shower particles interact with them and this allows to detect the incident particle. The energy resolution of the SpaCal calorimeter is

$$\frac{\sigma_{em}}{E} = \frac{7\%}{\sqrt{E(GeV)}} \oplus 1\%,$$

for electromagnetic part and for hadronic part:

$$\frac{\sigma_{had}}{E} = \frac{13\%}{\sqrt{E(GeV)}} \oplus 4\%,$$

as determined in test beams measurements [49].

3.1.2 The Tracking system

The purpose of the tracking system is to accurately determine the interaction point, to identify charged particles, reconstruct their trajectories and measure their momenta. Figure 3.6 shows the structure of the H1 tracking system.
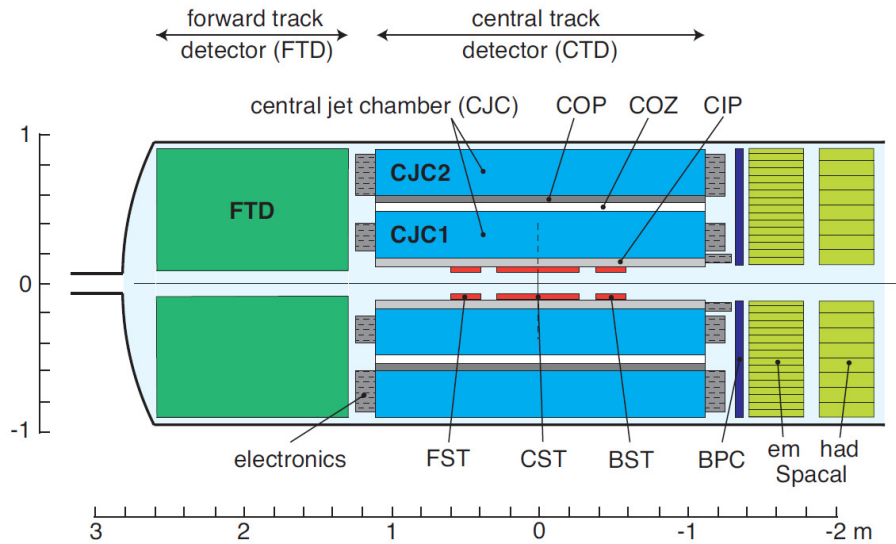
Figure 3.6: The view of the HERA II H1 detector tracking system. The picture is taken from [50].

3.1.3 Central Tracking Detector

The Central Tracking Detector (CTD) consists of two Central Jet Chambers (CJC1, CJC2), central, forward and backward silicon trackers (CST, FST, BST), the Central Outer Z-chamber (COZ), Central Inner Proportional

Chamber (CIP2k). The transverse view of the Central Tracking Detector is shown in Figure 3.7.
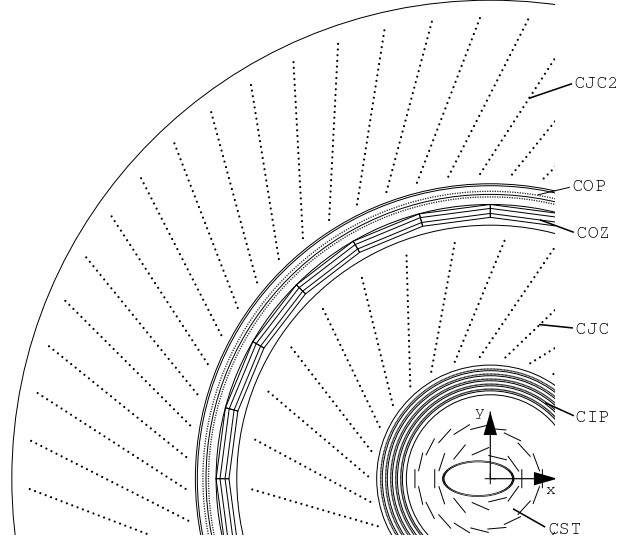
Figure 3.7: Transverse view of the Central Tracking Detector.

CJC1 and CJC2 [51] are cylindrical drift chambers located concentrically around the beam-axis. The chambers are used for precise measurement of momentum and azimuthal angle of charged particles. The detectors cover a polar angle of $15° \lesssim \theta \lesssim 165°$. Single hits are reconstructed from the measured drift time with the spatial resolution of about $170\,\mu$m in the $r - \phi$ plane and 22 mm in the z direction. The momentum resolution measured by the CJC is

$$\frac{\sigma(p_T)}{p_T} \sim 0.01 \cdot p_T(GeV)\ [52].$$

In addition the CJCs are used to determine the event timing with the precision of about 1 ns.

The Central Outer z-chamber (COZ) is located between CJC1 and CJC2 in order to complement the measurements in the $r - \phi$ plane and the z-direction. The COZ covers a range of $25° \lesssim \theta \lesssim 156°$ in polar angle. The resolution in z is typically $300\,\mu$m.

The Central Inner Proportional Chamber (CIP) is a cylindrical multi-wire proportional chamber that consists of five radial layers. The CIP is located between the CST and the CJC. The chamber can determine the

z-vertex position quite fast ($\sim 2\,\mu$s), which is very efficient in rejecting the background during the data record.

The CST [53] is the closest detector to the nominal interaction point. The spatial resolution of the tracker in the $r - \phi$ plane is approximately $14\,\mu$m. Since the resolution of the CST is an order of magnitude better than the resolution provided by the proportional chambers, it is improving the measurement of the whole CTD.

3.1.4 Luminosity system

The luminosity for the H1 experiment is usually determined from the Bethe-Heitler (BH) process $ep \rightarrow ep\gamma$ [54]. In the BH process the emitted photon and the scattered electron are almost collinear to the incoming electron, which means that they stay within the beam pipe and are escaping the main H1 detectors. These events are recorded by dedicated detectors designed for that purpose. Another possibility for the luminosity measurement is wide angle QED Compton scattering [55]. In this case, particles have a transverse momentum and are measured by the main H1 detector.

3.1.4.1 Bethe-Heitler process

The scattered photon of the BH process is detected by the photon detector located close to the beam pipe and far from the interaction region at $z = -101.8\,$m, in order to cover small angels at which the photon is scattered. The luminosity is then calculated by measuring the total rate of the bremsstrahlung events (R_{total}), correcting for the background rate in non-colliding (pilot) bunches (R_0).

$$L = \frac{R_{total} - (I_{total}/I_0)R_0}{\sigma_{vis}}, \tag{3.2}$$

where I_{total} is the colliding electron beam current, I_0 is the current of the pilot, i.e. non colliding, beam and σ_{vis} is the visible part of the $ep \rightarrow ep\gamma$ cross section.

3.1.4.2 QED Compton process

In case of the QED Compton process, the electron and photon are detected in the backward SpaCal calorimeter. This method is insensitive to the details of the beam optics.

The determination of the integrated luminosity using the QED Compton process [56] is in an agreement with the measurement using the Bethe-Heitler process.

3.1.5 Time of Flight system

The Time of Flight (ToF) system is built up of several scintillator detectors with high time resolution that are connected to photomultipliers as shown in Figure 3.8. The purpose of the ToF system is to reduce the background coming from non-ep events which occur at a different time compared to those form ep interaction.
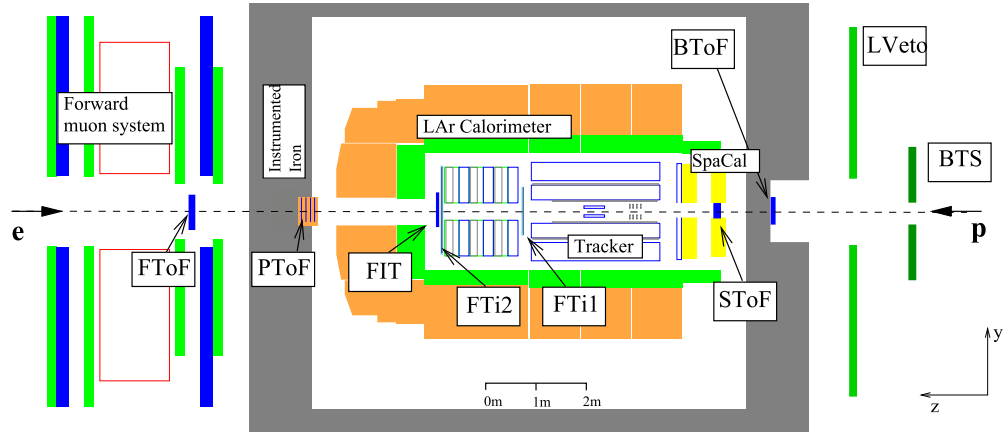
Figure 3.8: Schematic view in $y - z$ plane for different devices of the ToF system.

3.1.6 Trigger System

The HERA bunch crossing rate is about $10.4\,\mathrm{MHz}$, where the rate of ep interactions is about $1\,\mathrm{kHz}$ and the rest are events from background processes.

The frequency at which the H1 detector can readout the information is about 50 Hz, thus reduction of the event rate is required.

In order to record only interesting events a trigger system is used. The task of the trigger system is to make a quick decision on whether the event is worth to be kept or not. In order to make the trigger system more efficient, it has several levels of triggering, organized such that each higher level has a lower event recording frequency and more time to make the decision. A schematic view of the trigger system is shown in Figure 3.9.
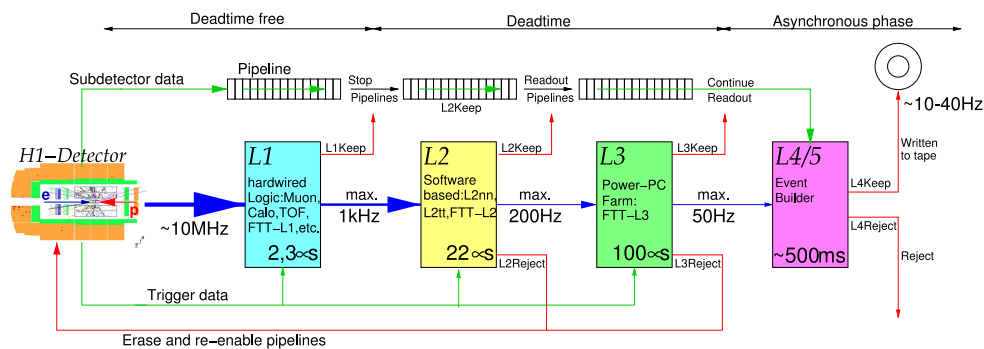
Figure 3.9: Schematic view of the trigger system of the H1 experiment.

3.1.6.1 The Level One Trigger

The level one trigger (L1) spends up to $2\,\mu$s to make a decision on whether to accept or reject an event. The decision is based on information available from scintillation counters, proportional and drift chambers as well as on muon detector and calorimeters as trigger elements. These trigger elements are passed to the Central Trigger Logic (CTL), which then combines them logically into subtriggers. The CTL decides to keep an event (L1Keep), if at least one subtrigger was set. The information is then passed to the next level trigger (L2), the data pipelines are stopped and the dead time starts to accumulate. If no subtrigger is set the information is dropped and no dead time is generated. The first level trigger has an output rate of about 1 kHz. The trigger elements important for charged and neutral current cross section measurements are the Liquid Argon trigger elements, the CIP chamber trigger elements as well as SpaCal triggers. A brief description for

those elements is given in Table 3.1 and Table 3.2. The SpaCal trigger is mainly used for the low Q^2 cross section measurements.

Name	Description
CIP_sig	Significance in the central part of the interaction vertex determined from the CIP track elements.
CIP_T0	A timing signal set if there is at least one central CIP track element in coincidence with the interaction time.
CIP_MUL	High multiplicity of the CIP track elements.

Table 3.1: List of tracking system trigger elements used for the charged current event triggering. Table adopted from [57].

Name	Description
LAr_Etmiss	The threshold on the transverse energy imbalance.
LAr_IF	The energy deposit belonging to the IF region.
	a deposit of energy in the electromagnetic part of the LAr calorimeter.
LAr_T0	An "OR" of the TT timing signals T_0 determined by a constant fraction discriminator technique.

Table 3.2: List of trigger elements provided by the LAr calorimeter trigger used for the charged current event triggering. Table is taken from [57].

3.1.6.2 Level Two Trigger

The level two trigger (L2) is a combination of three independent trigger system, the neural network trigger (L2NN), the topological trigger (L2TT) and the second level of the Fast Track Trigger (FTT). The decision on the second level is taken in $20\mu s$. The L2NN trigger [58] consists of neural networks, which are trained with *ep* and background events. The L2TT trigger [59] makes decision based on the topological signature of the event

taken from subdetector signals. The FTT [60–63] trigger decision on the second level is based on tracks in CJC1 and CJC2. Again, like in case of L1 trigger, if accepted (L2keep) the event information is being passed to the next level. Otherwise the event information is deleted and the dead time accumulation is stopped.

3.1.7 Level Three Trigger

The third level trigger (L3) is based on the third level of the FTT. It performs a partial event reconstruction during the allowed time window of $100\,\mu$s. In case of a positive (L3Keep) decision, the event information is completely read out, otherwise the readout is aborted.

3.1.8 Level Four and Five Triggers

On this level the full detector information is available. The information is used by farm processors to reconstruct the event, using the H1 reconstruction algorithm H1REC, and classify the event. If the events are passing the classification, they are written to tapes for permanent storage and offline analysis.

Chapter
4

Neutral and charged current cross section measurement

This chapter gives an overview of the experimental procedures of the neutral current (NC) and charged current (CC) cross section measurements performed by the H1 collaboration [57, 64–70].

The description of different methods used for the reconstruction of the kinematic variables is followed by the discussion of the neutral and charged current event reconstruction and event selection. The last section presents a brief description of the systematic uncertainties on the measurements.

The information should be sufficient to understand the origins of various uncertainties on the NC and CC cross section measurements discussed in the last section of this chapter.

Displays of high Q^2 NC and CC events recorded by the H1 detector are shown in Figure 4.2 and Figure 4.1 correspondingly. The NC event shows a compact energy deposit in the electromagnetic part of the LAr calorimeter from the scattered electron. The transverse momentum of the scattered electron is kinematically balanced by the hadronic final state (HFS) on

the opposite side of the detector. The CC shows only the HFS, since the scattered neutrino is escaping undetected, which causes the energy imbalance in the LAr calorimeter.
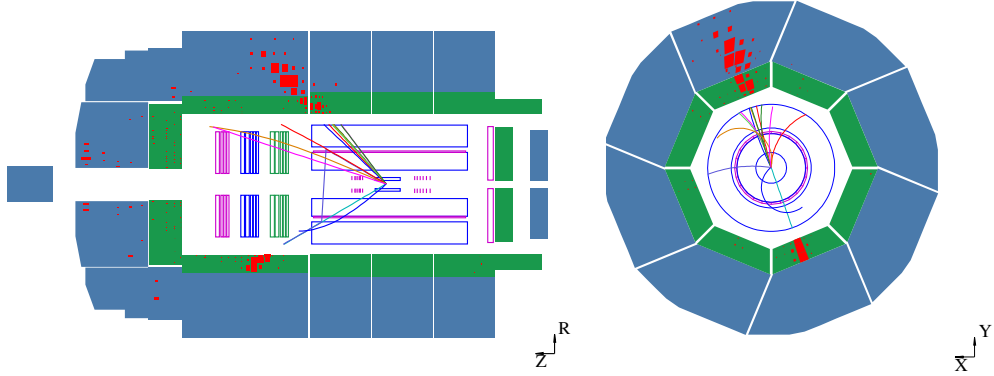
Figure 4.1: Cross section of a high Q^2 NC event in the H1 detector shown in longitudinal (left) and transverse (right) plane.
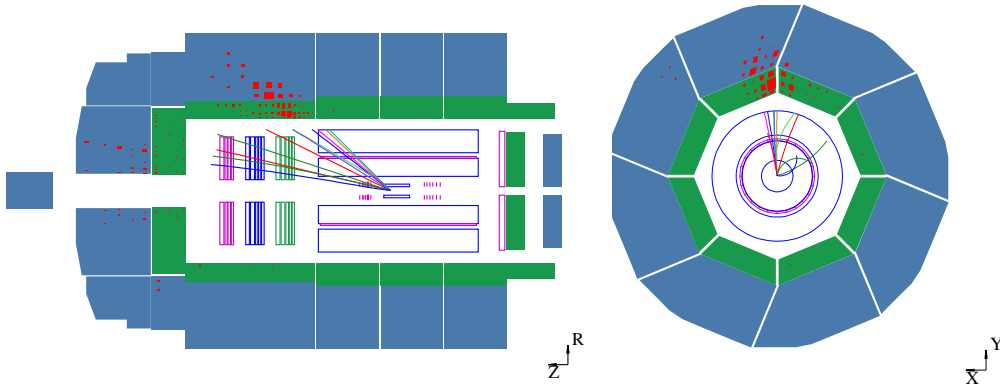
Figure 4.2: Cross section of a high Q^2 CC event in the H1 detector shown in longitudinal (left) and transverse (right) plane.

4.1 Kinematic reconstruction

For cross section measurements it is crucial to reconstruct the kinematics of the events precisely. The DIS kinematics can be reconstructed either using only the hadronic final state or the scattered electron or the combination

of both. In case of CC events the hadronic reconstruction method is used, while the other methods are applied in case of NC events. Different reconstruction methods for the kinematic variables Q^2, y and x, described in section 2.1, are shortly discussed below.

4.1.1 Electron method

The electron method [71] is based on the measurement of the electron energy, E'_e, and its polar angle, θ_e. The variables Q^2, x and y are then calculated as

$$y_e = 1 - \frac{E'_e}{E_e} \sin^2(\frac{\theta_e}{2}), \tag{4.1}$$

$$Q_e^2 = \frac{(E'_e \sin \theta_e)^2}{1 - y_e} \tag{4.2}$$

and

$$x_e = \frac{Q_e^2}{s y_e}. \tag{4.3}$$

The electron method is the most precise reconstruction method for $y \gtrsim 0.1$. The x resolution is getting worse at small values of y, where the relative uncertainty on y becomes large. The method is sensitive to initial state QED radiation, shown in the first diagram of Figure 2.6 and Figure 2.7. The initial state radiation decreases the collision energy, which leads to wrong determination of the kinematic variables.

4.1.2 Hadron method

The kinematic variables can also be reconstructed from the hadronic final state [72]. They are calculated from the measured energy E_h, transverse momentum $p_{T,h}$ and momentum component parallel to the beam axis $p_{z,h}$. The index h runs over all the particles belonging to the hadron final state.

$$y_h = \frac{1}{2E_e} \sum_h (E_h - p_{z,h}), \tag{4.4}$$

$$Q_h^2 = \frac{p_{T,h}^2}{1 - y_h}, \tag{4.5}$$

$$x_h = \frac{Q_h^2}{sy_h}. \tag{4.6}$$

The transverse momentum $p_{T,h}$ is defined as

$$p_{T,h} = \sqrt{\left(\sum_h p_{x,h}\right)^2 + \left(\sum_h p_{y,h}\right)^2}. \tag{4.7}$$

This method has a moderate precision over the whole y range, due to particles with small transverse momentum escaping the detector through the beam-pipe.

4.1.3 Double Angle method

The method for the kinematic reconstruction using the polar angle of the scattered electron θ_e and the hadronic final state γ_h is called Double Angle (DA) method [71]. The hadronic final state angle γ_h is defined as

$$\tan\frac{\gamma_h}{2} = \sum_h \frac{E_h - p_{z,h}}{p_{T,h}} \tag{4.8}$$

and corresponds to the angle of a scattered quark in quark-parton model (QPM) assuming that the quark is massless. The kinematic variables are given by

$$y_{DA} = \frac{\sin\theta_e(1 - \cos\gamma_h))}{\sin\gamma_h + \sin\theta_e - \sin(\theta_e + \gamma_h)}, \tag{4.9}$$

$$Q_{DA}^2 = \frac{4E_e^2 \sin\gamma_h(1 + \cos\theta_e)}{\sin\gamma_h + \sin\theta_e - \sin(\theta_e + \gamma_h)}, \tag{4.10}$$

$$x_{DA} = \frac{Q_{DA}^2}{sy_{DA}}. \tag{4.11}$$

The method is independent from the energy measurement by the calorimeter and thus can be used to calibrate the LAr calorimeter.

4.1.4 Sigma method

The sigma (Σ) method [73] is based on energy and momentum conservation.

$$p_T^{in} = p_T^{out} = E'_e \sin \theta_e + \sum_h (E_h \sin \theta_h), \tag{4.12}$$

$$2E_e = \sum_h (E_h - p_{h,z}) + (E'_e - p_{e,z}) = \sum_h (E_h - p_{h,z}) + E'_e (1 - \cos \theta_e), \tag{4.13}$$

where the sum runs over the particles in hadron final state. The variable y is calculated from the formula as for the hadron method

$$y_\Sigma = \frac{\sum_h (E_h - p_{h,z})}{\sum_h (E_h - p_{h,z}) + E'_e (1 - \cos \theta_e)}. \tag{4.14}$$

The other kinematic variables are calculated by

$$Q_\Sigma^2 = \frac{P_{T,e}^2}{1 - y_\Sigma} = \frac{E'^2_e \sin^2 \theta_e}{1 - y_\Sigma}, \tag{4.15}$$

$$x_\Sigma = \frac{Q_\Sigma^2}{s y_\Sigma} \tag{4.16}$$

The Σ method has a reduced sensitivity to hard initial state radiation and to the particle losses in the beam pipe. This method provides a good resolution at moderate values of y.

4.1.5 Electron-sigma method

The electron and Σ methods are combined in order to exploit the advantages from each of the methods [74]. The variable Q^2 is determined using the electron method and the variable x using the Σ method.

$$y_{e\Sigma} = \frac{2E_e}{E - p_z} y_\Sigma, \tag{4.17}$$

$$Q_{e\Sigma}^2 = \frac{P_{T,e}^2}{1 - y_e}, \tag{4.18}$$

$$x_{e\Sigma} = \frac{P_{T,e}^2}{s y_\Sigma (1 - y_\Sigma)}. \tag{4.19}$$

The electron-Σ method has a good resolution in the whole kinematic range.

The methods described above are used in the NC cross section measurements, according to their performance in different kinematic regions. The double angle method is also used to calibrate the calorimeters.

4.2 Event reconstruction

In order to precisely measure the NC inclusive cross sections, it is important to identify reliably the scattered electron, to measure with good resolution the electron energy and scatter angle and the properties of the hadronic final state. In case of the CC cross section determination only the properties of hadronic final state are measured. An accurate determination of the *ep* interaction position is also important, since the measurement of the scattered electron polar angle as well as the polar angle of the hadronic final state depends on this information.

4.2.1 Electron identification

The identification of the scattered electron is based on the information from the electromagnetic part of LAr and SpaCal calorimeter. A candidate for the scattered electron is defined as a compact and isolated energy deposit.

The electron identification is using the information from the shape of the shower in the calorimeter to distinguish between electromagnetic particles and hadrons. In the LAr calorimeter, an electron candidate is defined in a cone of 7.5°around an axis that originates from the interaction vertex to the centre of gravity of an energy cluster in the electromagnetic part of the LAr calorimeter. The cone also contains the first layer of the hadronic part of the calorimeter. Any cluster with barycentre inside this cone is merged with the initial cluster as shown in Figure 4.3. There are several characteristics used to differentiate an electromagnetic shower from a hadronic one and to define an electron.

- The electromagnetic energy fraction defined as $f_{em} = E_{em}/E_{tot}$ and will later be referred as EAEM. Here E_{em} is the energy measured in the electromagnetic part of the calorimeter and E_{tot} is the total
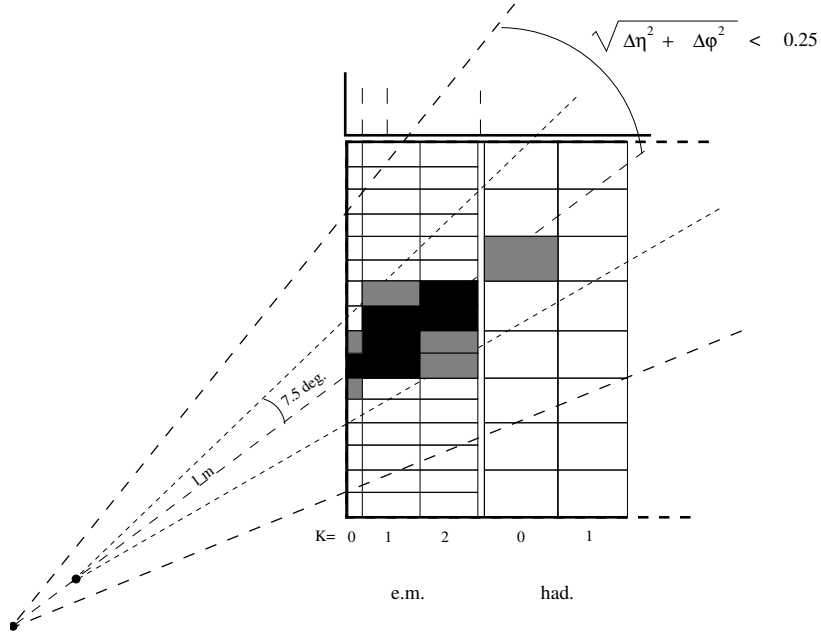
Figure 4.3: Schematic view of isolated cones used for the electron identification.

energy deposited in both electromagnetic and hadronic parts of the calorimeter.

- The transverse radius, calculated from the energy weighted transverse distance r_i of all cells in the cluster $\sigma(R) = \sqrt{<r^2> - <r>^2}$. The requirement on this variable, referred as EATR, depends on θ.

- The energy fraction in the "hottest" neighbouring cells $EAHN = E^N_{Hot}/E_{em}$, where E^N_{Hot} is the energy of the most energetic neighbouring cells. The value of N is defined according to the cluster position in the LAr calorimeter.

- Isolation criteria: first a cone is defined in the $\eta - \phi$ space with the radius $R_{\eta-\phi} = \sqrt{(\Delta\eta)^2 + (\Delta\phi)^2} = 0.25$. The estimator $EAIF = E_{tot}/E_{iso}$ has to be at least 0.98. Here E_{iso} is the total energy in the cone with $R_{\eta-\phi}$ and E_{tot} is the energy of the cluster. Candidates are also accepted if the $EAIF > 0.95$ and the total energy deposited in the hadronic section of the isolation cone $EAHD$ is below 300 MeV.

In the SpaCal calorimeter, the electron identification criteria are similar to the one for LAr calorimeter. The minimal energy of the cluster is required

to be at least $5\,\mathrm{GeV}$. The transverse radius of the clusters, calculated using a logarithmic weighting must be less than $4\,\mathrm{cm}$.

4.2.1.1 Electron identification efficiency

The electron finding efficiency is determined using an independent track-based electron finder [75]. The track based electron finder looks for isolated tracks within an isolated cone of radius $R_{\eta-\phi} = 0.5$ around the axis originating from the interaction vertex to an electromagnetic cluster in the LAr calorimeter. A track with $P_T > 1.2\,\mathrm{GeV}$, associated with the electromagnetic cluster is required to be in this cone.

The inefficiencies are found to be small except for the cases, where the energy of the electron candidate is small. The identification is less efficient due to the z and ϕ-cracks, where the electron is passing through the dead material. In some cases electrons may even enter the hadronic section of the LAr calorimeter via cracks, which is making the identification of the electron more difficult. For this reasons z-cracks in CB1 and CB2 as well as all ϕ-cracks are not considered in the measurement. The details of the electron finding efficiency are described in [66, 70]. The electron finding efficiency for HERA II data and Monte Carlo simulation is shown in the Figure 4.4. The uncertainty on the electron identification is considered to be $0.2\% - 1\%$ depending on the kinematic region.

4.2.2 Electron angle measurement

The polar angle θ_e and azimuthal angle ϕ_e of the scattered electron are determined from the position of its energy cluster in the LAr calorimeter with respect to the interaction vertex, measured using the information from the tracker. Due to the good resolution of the tracking detectors in the $r - \phi$ plane, the tracker information is used for the ϕ_e measurement. This is possible if a track is associated with the scattered electron, otherwise the azimuthal angle is calculated from the position of the energy cluster in the LAr calorimeter and the interaction vertex. Since the detector has an axial symmetry, the measured cross section is almost not sensitive to the ϕ_e determination. Thus, no uncertainty due to the azimuthal angle determination is assigned to the cross section.
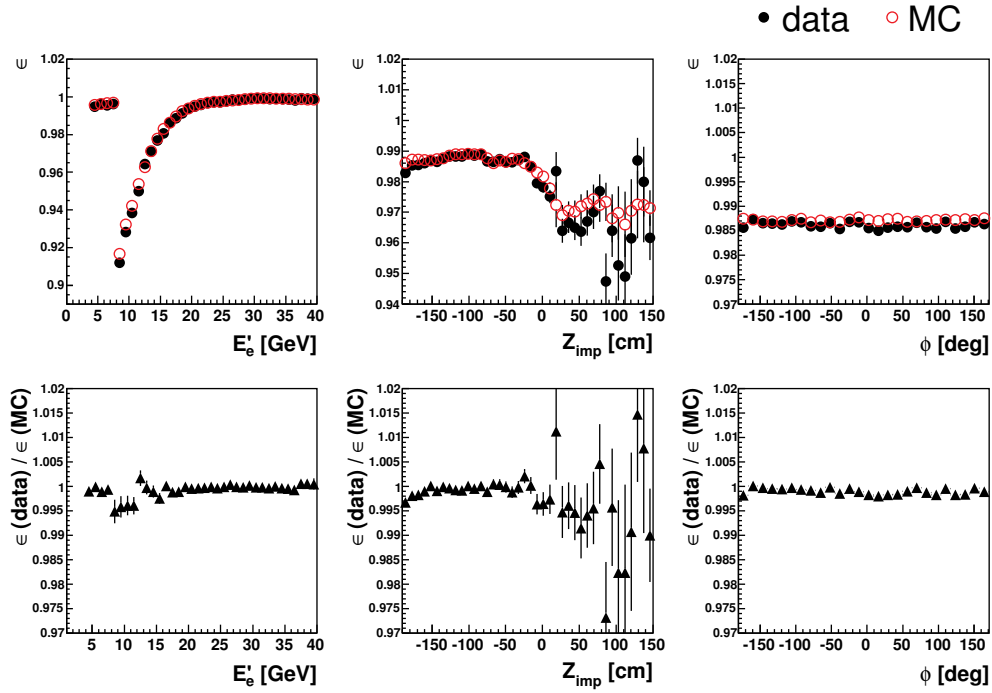
Figure 4.4: Electron finding efficiency as a function of the electron energy E'_e, azimuthal angle ϕ and z coordinate of the electron impact position on the surface of the LAr calorimeter for the HERA II events. The plot is adapted from [70].

For the θ_e measurement, the position information from the LAr cluster is taken. The uncertainty on the polar angle measurement is estimated to be 1 mrad. More details on the scattered electron azimuthal and polar angel determination can be found in [70].

4.2.3 Vertex-track-cluster matching

To determine the position of the primary interaction vertex as well as to correctly assign a track to the energetic cluster deposited in the LAr calorimeter, an accurate track reconstruction is required. The reconstruction is done by fitting a helical trajectory to the hits in the CJC. The hits are either associated with the track or removed as noise. Then, precise information from the CIP, COZ and CST detectors is added for an accurate

estimation of the track. In addition, the information from the known coordinates x and y of the beam line can be used to improve the track fitting. The z coordinates of the vertex is determined from those tracks fitted to this vertex. At least one track is required to reconstruct a vertex and to reduce non-ep background.

For the systematic studies the extrapolated track impact position on the LAr calorimeter is compared to the position of the electron cluster projected to the calorimeter surface. A fit is performed to minimise the difference between the compared positions. This procedure takes into account the fact that the geometrical dimensions of the calorimeter are determined at room temperatures, while in fact the parts of LAr calorimeter are cooled to temperature of liquid argon $72\,\mathrm{K}$. The calorimeter shrinkage is taken into account by allowing the calorimeter to move and rotate along the x, y and z axis. The corrections are applied to the data, since in Monte Carlo simulations, the detectors are aligned.

After corrections are applied, the remaining differences between data and the Monte Carlo simulation are assigned as systematic uncertainty. Depending on the kinematic region the uncertainty varies in a range of $0.5\% - 1\%$ [70].

4.2.4 Electron energy measurement

The precise measurement of the scattered electron energy is crucial for the NC measurement. In order to calibrate the electron energy, the double-angle (DA) reconstruction method is used. This method relies on the measured angles of the scattered electron and hadronic final state, as well as the initial beam energies and is independent from the energy measurement. The calibration is done by comparing the energy measured by the calorimeter E'_e to the amount of energy estimated from the double-angle method E_{DA}. To ensure a good precision of the double-angle method, the NC events used in the calibration procedure have several selection criteria in addition to those described in subsection 4.3.2 [70]. The mean values of the E'_e/E^{DA} ratio are taken as calibration factors. The impact of the E'_e/E^{DA} distribution tails is reduced by considering the mean values from the events only in the region of $0.85 < E'_e/E^{DA} < 1.15$. The calibration procedure is done iteratively in two steps.

The first step is the wheel- and octant-wise calibration, where a calibration factor is derived for BBE, CB1, CB2, CB3, FB1 and FB2. The second

step is the z-wise calibration, where calibration factors are determined as function of z_{imp} of the electron impact point in the LAr calorimeter. Those two steps are repeated iteratively with narrowing of the calibration window to $0.9 < E'_e/E^{DA} < 1.1$.
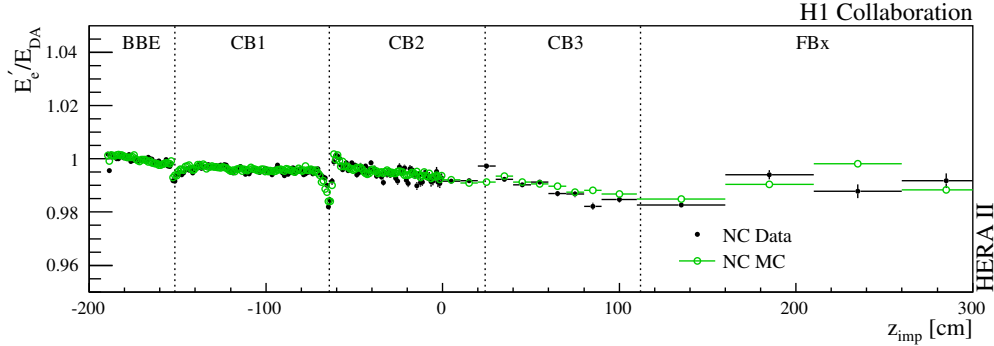
Figure 4.5: The mean value of the E'_e/E^{DA} as a function of z coordinate of the electron impact position on the surface of the LAr calorimeter for the complete HERA II data sample. BBE, CB1, CB2, CB3 and FBx stand for Backward Barrel Electromagnetic, Central Barrel and Forward Barrel wheels. The plot is taken from [11].

The effect of the electromagnetic calibration is shown in the Figure 4.5. The estimated uncertainty on the electron energy scale is $0.5\% - 1\%$ depending on the region of LAr calorimeter. An additional correlated uncertainty of $0.3\% - 0.5\%$ due to possible biases of the calibration method is added.

4.2.5 Hadronic Final State

The hadronic final state (HFS) is identified using an energy flow algorithm HADROO2 [76]. The algorithm is using the information from the tracking detectors and the calorimeters. The uncertainties on the track measurement are compared to the resolution of the calorimeter measurement. The algorithm then chooses the more precise information to reconstruct the particle candidate.

Since the LAr is a non compensating calorimeter, a weighting algorithm is used to compensate for the lower response of hadrons compared to electrons. A first weighting procedure is already applied at the reconstruction level, in

H1REC [77], where electromagnetic and hadronic clusters are reconstructed. In HADROO2 the procedure is modified. All the clusters with at least 95% of their energy in the electromagnetic part and with at least 50% of its energy in the first two layers of the electromagnetic calorimeter are taken at the electromagnetic scale. All the other clusters are considered as originating from hadrons and the hadronic energy scale, determined by the H1REC weighting algorithm, is considered.

4.2.5.1 Noise suppression

The energy measurements of the LAr calorimeter are affected by a relatively large amount of noise due to detector effects, like noise in the electronics or energy deposits coming from $non-ep$ interactions, a few GeV per event [69]. In particular, the distribution of y_h is affected. Not identified noise clusters will count in the sum of Equation 4.4 with a weight increasing with the θ. So even a cluster with relatively low noise in the barrel part of the LAr will strongly bias the y_h distribution. There is a set of noise finders applied in order to suppress it [78, 79]. After correcting for the noise, a systematic uncertainty of about 10% is assigned to the estimation of the noise energy, which is later propagated to the cross section measurement.

4.2.5.2 Calibration of the hadronic energy

The hadronic part of the calorimeter is calibrated by comparing the transverse momentum estimated by the double-angle method $P_{T,DA}$ to the measured one. The procedure is more complex compared to the electron energy scale calibration, however the same concept is applied. The detailed description of the HFS calibration can be found in [50, 70].

In Figure 4.6 the measured y_h/y_{DA} ratio is compared to the simulation as a function of the inclusive hadronic angle γ_h after applying the calibration procedure. The uncorrelated uncertainty on the hadronic energy scale in the LAr (SpaCal) calorimeter is estimated to be 1%(0.5%). An additional correlated uncertainty of 0.3% is assigned due to possible biases introduced by the calibration method.
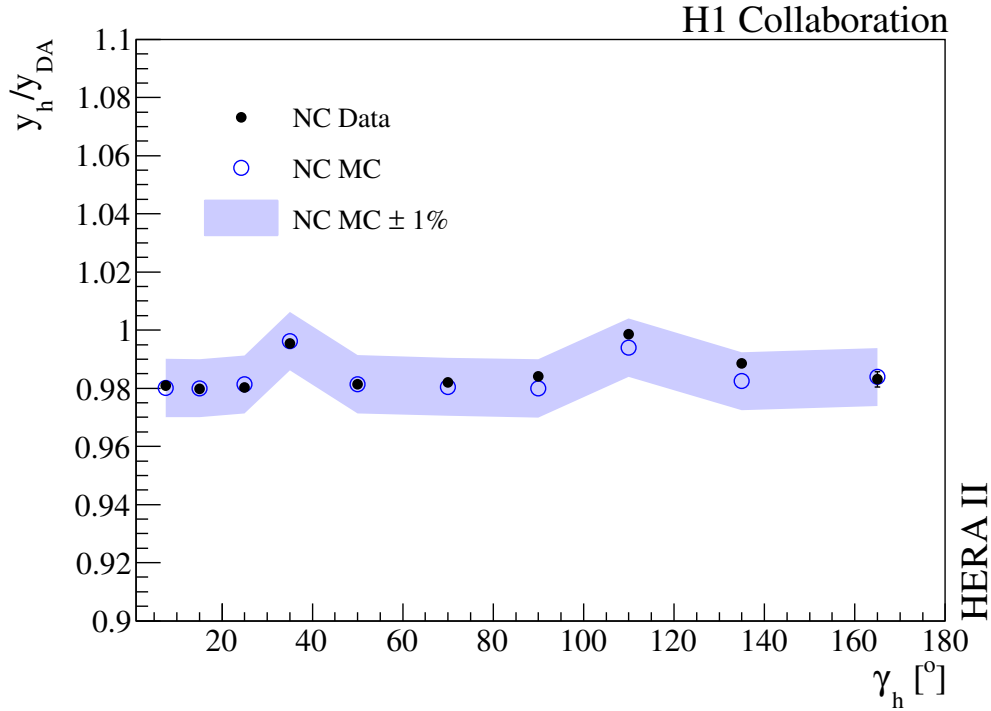
Figure 4.6: The mean value of the y_h/y_{DA} as a function of γ_h for the full neutral current HERA II data set. The solid points correspond to the data and the open circles correspond to the Monte Carlo simulation. The band corresponds to a ± 1 variation around the simulation. The plot is taken from [11].

4.3 Event selection

A first selection of the neutral and charged current events candidates is done online, using various triggers during the data taking. Offline, more refined selection criteria are applied.

4.3.1 Online selection

The online event selection is performed by triggers. After fulfilling certain requirements, the neutral or charged current event candidate is recorded.

The main characteristics of the charged current events is the missing transverse momentum due to the undetected neutrino. The triggering of a

CC event is based on the information on the imbalance of the transverse energy in the LAr calorimeter and event timing information. The selection of the neutral current events is based on the identification of the scattered electron in the LAr or SpaCal calorimeter. This condition is also efficient to select the CC events, since the detected electromagnetic clusters energy can also be produced in the hadronic final state.

4.3.2 Offline selection

The offline selection of events for the inclusive cross section measurement starts with requiring quality conditions on the run selection. The events recorded in a certain period of time are divided into runs. The runs are then classified according to the overall detector performance to "good", "medium" or "poor". Only "good" and "medium" runs are selected. Another criterium is the operating status of the detector components. A "HV on" requirement is applied for the LAr calorimeter, the central drift chambers, the proportional chambers, the luminosity system and the time of flight system. Some of the HV requirements are included in the run classification. To ensure that the detector was stable during a run, a minimal luminosity of $0.2\,\mathrm{nb}^{-1}$ is required for each run.

4.3.2.1 Interaction vertex

The beam position in the x, y plane may vary for different runs, which may cause variations of the ep interaction vertex position. The interaction vertex position in the z direction (z-vertex) is distributed around $z = 0$ point according to Gaussian distribution. Since the acceptance of the detector is better in the region close to the nominal interaction point, the reconstructed z-vertex should correspond to the region $-35\,\mathrm{cm} < z_{vertex} < 35\,\mathrm{cm}$. This range corresponds to one σ of the vertex distribution.

4.3.2.2 Kinematic phase space

The cuts on the kinematic variables are connected to the detector acceptance and efficiencies of the triggers. In case of the charged current measurements a cut on the missing transverse momentum is set to $P_{T,miss} > 12\,\mathrm{GeV}$. Below this value the trigger efficiency is dropping drastically which causes

an increase of the *ep* induced background. The variable y is restricted to the range of $0.03 < y < 0.85$. The upper bound is set due to the bad kinematic resolution and the lower band is set in order to have a high enough trigger efficiency.

The energy and momentum conservation requires that $\sum(E - p_z) = 2E_e$ and in case of HERA $2E_e = 55.2\,\mathrm{GeV}$. However, the measured energy of the final state has a certain accuracy, so a cut on this variable is introduced according to the detector performance. In case of neutral current events the following cut is applied $35\,\mathrm{GeV} < E - P_z < 75\,\mathrm{GeV}$. To ensure good kinematic resolution and low trigger efficiencies the variable y should be in $0.05 < y < 0.9$ region. Since the identification of the electron is essential for the neutral current measurement, the events with an electron candidate pointing to the crack in the LAr calorimeter (ϕ-cracks) as well as the cracks between CB2 and CB3 (z-cracks) are rejected. The electrons at the backward part of the BBE are also rejected.

4.3.3 Background rejection

The background processes that might impact the CC and NC cross section measurements can be sorted in two groups depending on their origins. The first group is background from *ep* processes and the second group is built of the events from non-*ep* processes.

The main *ep* induced background sources for CC measurements are NC DIS events and photoproduction, which give the largest contribution, as well as events from QED Compton, lepton pair production or W production. In case of the NC measurements, the main background processes are photoproduction and QED Compton events. Most of these events are suppressed by the selection cuts.

Non-*ep* background events can be produced from either highly energetic cosmic particles interacting with the detector, or the interaction of the proton beam with residual gas in the beam pipe. Those are suppressed using timing information from the detector or by exploiting topological cuts against the topology of the background events [57, 80].

4.4 Cross section measurement

The differential cross section in a bin of (x, Q^2) is measured by counting the selected number of events N, divided by the integrated luminosity $\mathcal{L}$ is known

$$\sigma = \frac{N}{\mathcal{L}}. \tag{4.20}$$

However, the formula has to be corrected to take into account the presence of the background, the acceptance of the detector, composed of the geometrical acceptance and the selection efficiency effects, and QED radiative effects. After modification the Equation 4.20 takes form

$$\sigma(x_c, Q_c^2) = \frac{N - N_{bg}}{\mathcal{L} \cdot \mathcal{A}} \cdot \mathcal{C} \cdot (1 + \Delta^{QED}). \tag{4.21}$$

Here, N_{bg} corresponds to the number of background events estimated using Monte Carlo simulations, $\mathcal{A}$ is the acceptance. The index x in variables x_c and Q_c^2 indicates that the values are taken at the centre of the bin. To take finite bin size effects into account, a bin size correction is applied. The factor $\mathcal{C}$ corresponds to the bin centre correction estimated using theoretical cross section. It scales the cross section integrated in the bin to a differential cross section at the bin centre x_c, Q_c^2

$$\mathcal{C} = \frac{\sigma^{th}(x_c, Q_c^2)}{\iint_{bin} dx_i dQ_i^2 \sigma^{th}(x, Q^2)}. \tag{4.22}$$

The effect of radiative corrections is represented by the factor Δ^{QED}.

4.4.1 Acceptance, purity, stability

To control the quality of the cross section measurement the variables acceptance $(\mathcal{A})$, purity$(\mathcal{P})$ and stability$(\mathcal{S})$ are introduced. The variables are determined from Monte Carlo simulations and are defined as

$$\mathcal{A}^i = \frac{N_{rec}^i}{N_{gen}^i}, \tag{4.23}$$

$$\mathcal{P}^i = \frac{N_{rec+gen}^i}{N_{gen}^i}, \tag{4.24}$$

$$\mathcal{S}^i = \frac{N^i_{rec+gen}}{N^i_{gen+sel}}, \tag{4.25}$$

where

- N^i_{rec} is the number of events reconstructed in the ith bin,

- N^i_{gen} is the number of generated events in the ith bin,

- $N^i_{rec+gen}$ is the number of events generated and reconstructed in the ith bin,

- $N^i_{rec+sel}$ is the number of events generated in the ith bin and fitting the selection criteria.

The acceptance contains all detector effects, like resolution and efficiencies. Purity and stability account for smearing effects. Purity represents the fraction of events reconstructed in the ith bin, which where generated in the same bin. The stability is the fraction of the events generated in the bin i and selected in the same bin.

For the HERA II NC and CC cross section measurements, both purity and stability are required to be larger than 30%. In addition, the acceptance of the events entering the cross section measurement is required to be more than 40% [69].

4.5 Systematic uncertainties

The uncertainties due to the detector performance result in systematic uncertainties on the measurement. Those errors are split into a correlated and an uncorrelated part. The correlated errors may cause a correlated systematic shift for all of the measurements. An example is the electron or hadronic energy scale uncertainty, which may be different from the true energy scale value by the same amount all over the detector. Uncorrelated errors occur if detector effects in different regions of the detector are uncorrelated. The correlated uncertainties are considered to be symmetric. The total systematic error is obtained by adding the individual uncertainties in quadrature.

The sources of the systematic uncertainties, their size and region of applicability are summarised in table 4.1. Some details on the main sources of the uncertainties are given below.

Source		Uncertainty
Electron energy scale	$z_{\text{imp}} \leq -150 \,\text{cm}$	0.5% unc. $\oplus$ 0.3% corr.
	$-150 < z_{\text{imp}} \leq -60 \,\text{cm}$	0.3% unc. $\oplus$ 0.3% corr.
	$-60 < z_{\text{imp}} \leq +20 \,\text{cm}$	0.5% unc. $\oplus$ 0.3% corr.
	$+20 < z_{\text{imp}} \leq +110 \,\text{cm}$	0.5% unc. $\oplus$ 0.3% corr.
	$z_{\text{imp}} > +110 \,\text{cm}$	1.0% unc. $\oplus$ 0.3% corr.
Electron scale linearity	$E'_e < 11 \,\text{GeV}$	0.5%
Hadronic energy scale	LAr & Tracks	1.0% unc. $\oplus$ 0.3% corr.
	SpaCal	5.0% unc. $\oplus$ 0.3% corr.
Polar angle	θ_e	1 mrad corr.
Noise	NC $y < 0.19$	5% energy not in jets , corr.
	NC $y > 0.19$	20% corr.
	CC	20% corr.
NC trigger efficiency	e^+p 2003-2004	0.5%
	e^-p 2004-2005	0.6%
	e^-p 2006	0.5%
	e^+p 2006-2007	0.3%
	NC *high y*	$0.5 - 1.2\%$
Electron track and vertex efficiency	$\theta_e > 50°$	0.2%
	$\theta_e < 50°$, NC *high y*	1.0%
Electron charge determination	NC *high y*	0.5%
Electron ID efficiency	$z_{\text{imp}} < 20 \,\text{cm}$ ($\geq 20 \,\text{cm}$)	0.2% (1.0%)
Background	NC, CC: γp	30% corr.
	CC: NC (others)	10% (20%) corr.
Background γp charge asymmetry	NC *high y*	1.03 ± 0.05 corr.
CC trigger efficiency (ϵ)		$15\% \cdot (1 - \epsilon) \oplus 0.2\%$
CC vertex efficiency	$y \geq 0.15$ (< 0.15)	1.5% (3.0%)
CC background finder efficiency	$y \geq 0.08$ (< 0.08)	1.0% (2.0%)
CC V_{ap}/V_p bg suppression cut		± 0.02 corr.
QED radiative corrections	NC $x < 0.1$, $0.1 \leq x < 0.3$, $x \geq 0.3$	0.3/1.0/2.0%
	NC *high y*	1.0%
	CC kinematics dependent	$\sim 1.0 - 2.0\%$
Acceptance corrections	NC $e^\pm p$: $Q^2 \leq 5000$ (> 5000) GeV^2	0.2% (1.0%)
	CC e^-p: $Q^2 \leq 5000$ (> 5000) GeV^2	0.2% (1.0%)
	CC e^+p: $Q^2 \leq 5000$ (> 5000) GeV^2	0.5% (3.0%)
Polarisation	LPOL (TPOL)	2.0% (1.9%)
Luminosity		2.3% corr. $\oplus$ 1.5% unc.

Table 4.1: Table of applied systematic uncertainties and regions of applicability. Uncertainties which are considered point-to-point correlated are labeled corr. All other sources are considered uncorrelated. The table is adapted from [11].

An important part of the NC and CC measurements is the reconstruction of the scattered electron energy and the hadronic final state energy. Uncertainties on the measurement of the electron energy using the LAr calorimeter appear mainly due to the calibration procedure. They may be different for different wheels of the calorimeter. The correlated part of the energy uncertainty of the NC cross section is estimated to be of up to 0.3%, which results in a correlated uncertainty of 4% depending on the Q^2 region. An uncertainty on the measurement of the hadronic energy has an uncorrelated part of about 1% for the LAr calorimeter and about 5% for the SpaCal calorimeter. This results in an uncorrelated uncertainty on the NC and CC cross section measurements of up to 5%. The correlated part of the uncertainty on the measurement of the hadronic energy is estimated to be 0.3% and results in a correlated uncertainty on the measured NC and CC cross sections of less than 1%.

In order to determine the kinematic variables a precise measurement of the polar angle of the scattered lepton is essential. A correlated uncertainty of 1 mrad on the polar angle θ results in correlated uncertainty on the NC cross section of less than 1%. The uncertainty increases for high values of x.

The noise in the LAr calorimeter may influence the energy measurements. A 20% uncertainty due to noise subtraction results in a 0.3% error on the measured cross section.

The uncertainty on the NC trigger efficiency is about 1% for the high y region and less than 1% for the other regions.

The vertex finding efficiency for the NC measurements results in an uncertainty of 15% for $y < 0.05$, 6% for $0.05 < y < 0.15$ region and 1% for $0.15 < y < 0.1$ region. This yields an uncertainty of 2% on the total cross section. In case of CC measurements uncertainty is up to 3% depending on the y region.

The background subtraction is another source of uncertainties. An uncertainty of 30% is assigned to the photoproduction background subtraction for both CC and NC measurements. The NC events may be misidentified as CC events due to a poorly measured scattered electron. An uncertainty of 10% is assigned to the subtraction of this background in case of CC measurements. The non-*ep* background finders introduce a 2% uncertainty for $y < 0.1$ and 1% for $y > 0.1$.

Theoretical uncertainties arising from QED radiative corrections and the choice of the PDFs in the simulations. The QED radiative corrections yield to 2% uncertainty in the CC measurements and up to 1% for the NC measurements [81]. The selection of the PDF for the Monte Carlo simulation results in 0.5% uncertainty.

There are also global uncertainties related to luminosity and polarisation measurements affecting the full data periods. A global uncertainty on the luminosity measurement for different data samples is estimated to be up to 2.3% with a correlated part of about 1.1%. In addition there is a 1.5% theoretical Bethe-Heitler cross section normalisation uncertainty. An uncertainty on the lepton beam polarisation up to 2.3% is assigned, depending on the particular dataset. More details on the estimation of the uncertainties can be found [11].

Chapter
5

Analysis overview and techniques

The precisely measured DIS NC and CC cross sections provide important information about the structure of the proton. The large kinematic region offered by the H1 data, 5 orders of magnitude in Q^2 and 5 in x, allows simultaneously for tests of QCD as well as for searches of physics beyond the SM. Figure 5.1 shows the kinematic coverage in x and Q^2 of the measured DIS neutral and charged current double differential cross sections used in the presented analysis. Signs of new physics are expected in the region of highest Q^2, whereas at low Q^2 and low x the cross sections are expected to be well described by QCD.

The precisely measured cross sections allow to accurately extract the parton distribution functions (PDFs) of the proton. Since for the extraction of the PDFs the shape dependence as function of x is crucial, double differential cross section is used. While for searches only the Q^2 dependence of the cross section is used in the presented analysis.

Various processes and data sets can be combined to determine the PDFs. DIS $e^\pm p$ data access the low x region, while fixed target DIS data constrain
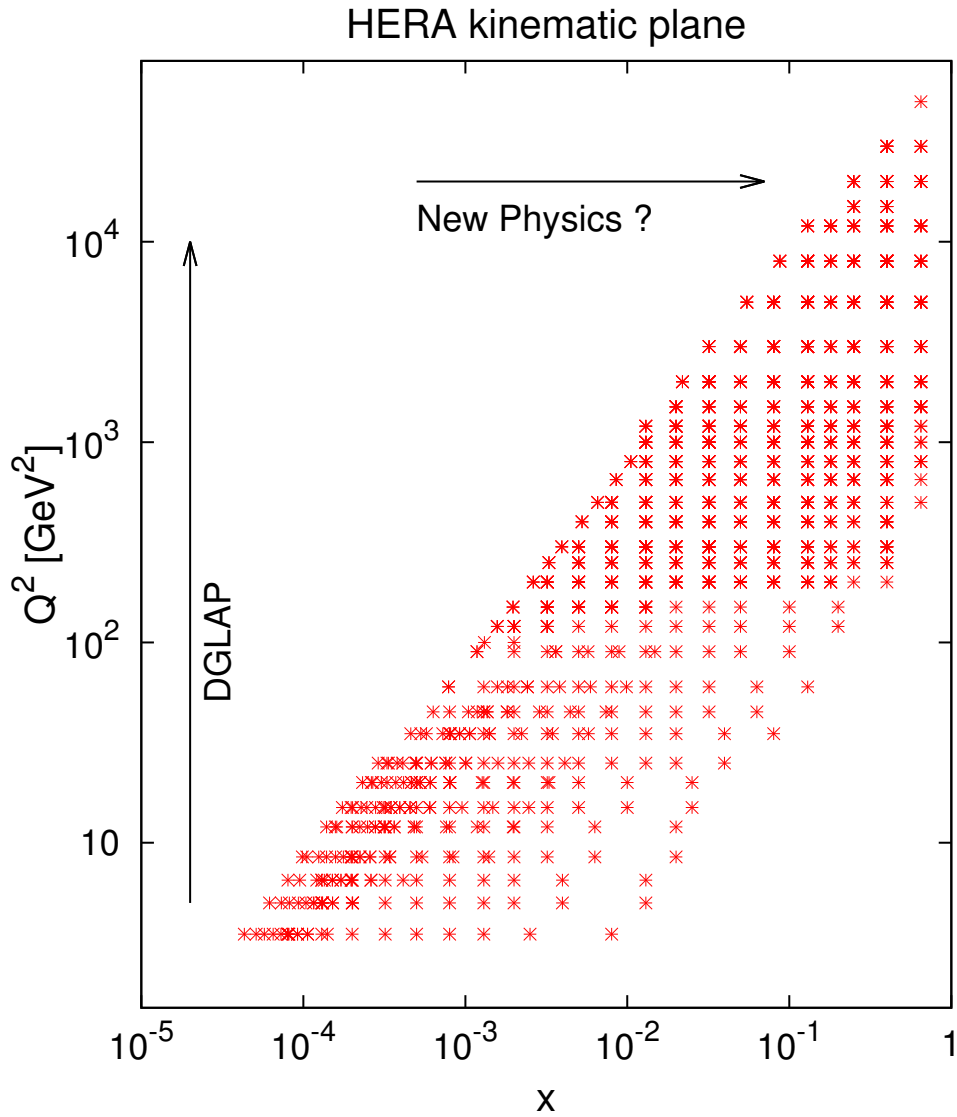
Figure 5.1: The inclusive cross section measurements as a function of x and Q^2. The DGLAP evolution equations are describing the Q^2 dependence of quark momentum densities. The signs of new physics are expected in the region of highest Q^2 values, in the upper right corner of the kinematic plane. The PDFs are constrained by the data at low Q^2 and x, located in the lower part of the plot.

quarks and gluons in the region of high x and low Q^2. The fixed target Drell-Yan data are sensitive to the sea quarks at high x and jet production[1] data contribute to the gluon distribution in the same region. W and Z boson production cross section data provide information about the different quark contributions. The CTEQ/CT, MSTW and NNPDF collaborations use a large amount of data from a variety of fixed target and colliding experiments as an input to their global analyses. Those global fits result in PDF sets like CTEQ6m [82], CT10 [83], MSTW08 [84] and NNPDF2.1 [85].

Despite the fact that all of the earlier mentioned processes provide sensitivity to the PDFs, they may not necessarily be included in the QCD analysis. Tensions between data sets from different experiments and processes may lead to technical difficulties and result in an increase of the PDF uncertainties [86]. The PDF determination is also possible based only on HERA DIS $e^{\pm}p$ data. An example of such a PDF set is HERAPDF1.0 [87]. This PDF set is based on combined measurements of the H1 and ZEUS experiments from the HERA I running period. Its comparison to the global PDFs determined by other groups provides a universality check.

The PDFs can also be extracted using the data from the H1 experiment alone. This was already done previously by introducing the PDF sets H1PDF 2000 [88] and H1PDF 2009 [89], which are based on HERA I low and high Q^2 data. The result of the current analysis, referred to as H1PDF 2012, includes the full sample of HERA I and HERA II inclusive DIS data and represents the most recent and final input of the H1 experiment in the PDF determination, based on H1 data only.

In section 5.1 a brief description of the statistical methods used in the current analysis is provided. The section includes the definition of the χ^2 function taking into account the treatment of the experimental uncertainties.

The chapter 6 contains the description of the performed QCD analysis, which results in the final set of parton distribution function from the H1 collaboration H1PDF 2012 [11]. The section describes the analysis framework, the procedure of the choice of the parton distributions parametrisation. It is followed by the discussion of the uncertainties and their treatment in the analysis. The last part of this section presents the results obtained from the fit and their comparison to data, as well as a comparison to existing

---

[1]Jet is a highly directed spray of particles originating from a certain quark or gluon.

sets of parton distribution functions[2].

The precise measurement of the inclusive DIS cross sections also allows to search for physics beyond the Standard Model at large scales. Indirect signs of new phenomena may be observed as deviations of the data from the SM predictions. The concept of contact interactions (CI), described in chapter 2, provides a convenient framework to describe indirect signatures of new physics. The main idea of the presented CI analysis is to fix the SM parameters, which are constrained mainly by measurements at low Q^2, and to look for possible deviations of the single differential NC cross section in the high Q^2 region. The description of the CI analysis and results are given in section chapter 7.

5.1 Definition of the χ^2 function

In order to quantify the consistency between a measurement and a theoretical prediction on a statistical basis and to estimate unknown parameters from a set of measurements the method of least squares can be used. This method has its own right of existence [90], but also can be derived from the maximum likelihood principle. Assuming there are a set of measured pair values $\{y_i, x_i\}$, given by a probability density function $f(x_i, \boldsymbol{\theta})$, where $\boldsymbol{\theta}$ is a set of unknown parameters. Then the method of maximum likelihood consists of finding a set of estimators $\boldsymbol{\theta}$, which maximises the likelihood function $\mathcal{L} = \prod_i f(x_i, \boldsymbol{\theta})$. The measurements y_i, for given x_i, are Gaussian distributed with mean $m(x_i, \boldsymbol{\theta})$ and variance σ_i, the negative logarithm of the likelihood function can be related to a standard χ^2 function by

$$- 2 \ln \mathcal{L} = \underbrace{\sum_i \left[\frac{y_i - m(x_i, \boldsymbol{\theta})}{\sigma_i} \right]^2}_{\chi^2(\boldsymbol{\theta})} + \underbrace{2 \sum_i \ln \sigma_i \sqrt{2\pi}}_{\text{const.}} . \qquad (5.1)$$

The best estimate of the parameter values corresponds to maximising the likelihood function and is equivalent to minimising the χ^2 function of Equation 5.1.

---

[2]The results of the presented analysis are published, so the majority of plots and tables from the section 6.5 correspond to ones used in the publication [11].

5.1.1 χ^2 with systematic errors

Equation 5.1 neglects all correlation between the measurements y_i. If the measurements are not independent, the full covariance matrix must be used

$$\chi^2 = [\mathbf{Y} - \mathbf{M}(\boldsymbol{\theta})]^T V^{-1} [\mathbf{Y} - \mathbf{M}(\boldsymbol{\theta})], \tag{5.2}$$

where $\mathbf{Y}$ corresponds to the vector of all measurements y_i and the vector $\mathbf{M}(\boldsymbol{\theta})$ to the predictions $m(x_i, \boldsymbol{\theta})$. $V_{ij} = cov[y_i, y_j]$ is the covariance matrix. Equation 5.2 can be found in different textbooks on statistics [90, 91].

An alternative representation of the Equation 5.2 is introduced in case the covariance matrix fulfils certain conditions. The mathematical derivation presented here is inspired by the Appendix C of [92]. Assume that the covariance matrix V has two components V^{sys} and V^{stat} originating from a systematic and statistical uncertainty, such that $V = V^{sys} + V^{stat}$. Assuming that V^{sys} is a correlated systematic uncertainty originating from one source, V^{sys} is defined to be of rank 1. It can be composed from a vector $\mathbf{w}$ as

$$V^{sys} = \mathbf{w}\mathbf{w}^T. \tag{5.3}$$

Then, using the Sherman-Morison formula [93], the Equation 5.2 can be reformulated to

$$\chi^2 = [(\mathbf{M} - \beta\mathbf{w}) - \mathbf{Y}]^T (V^{stat})^{-1} [(\mathbf{M} - \beta\mathbf{w}) - \mathbf{Y}] + \beta^2. \tag{5.4}$$

Here β is defined as

$$\beta = -\frac{[\mathbf{Y} - \mathbf{M}]^T (V^{stat})^{-1} \mathbf{w}}{1 + \mathbf{w}^T (V^{stat})^{-1} \mathbf{w}}. \tag{5.5}$$

Assuming now that the total systematic covariance matrix is a sum of covariance matrices originating from K sources of systematic uncertainties, the previous formula can be rewritten in the form of

$$\chi^2 = \sum_{i,j} [y_i - \alpha_i m_i](V_{ij}^{stat})^{-1}[y_j - \alpha_j m_j] + \sum_k (\beta^k)^2, \tag{5.6}$$

by replacing $\beta\mathbf{w}$ and β^2 with $\sum_k \beta^k \mathbf{w}^k$ and $\sum_k (\beta^k)^2$ respectively. Here

$$\alpha_i = 1 - \sum_k \beta^k \gamma_i^k \tag{5.7}$$

and

$$\gamma_i^k = \frac{w_i^k}{m_i}. \tag{5.8}$$

The γ^k vectors are relative errors of the systematic uncertainty of the source k and must be estimated in the data analysis. The set of variables $\sum_k \beta^k \gamma_i^k m_i$ are called systematic shifts of the data points i and β^k are the nuisance parameters of the systematic errors k. The shifts are usually represented in terms of σ, where 1 σ shift corresponds to the case $\beta^k = 1$. One unit of shift means that the data point i is shifted by a size of the experimental uncertainty $\gamma_i^k m_i$.

When neglecting the correlations within statistical uncertainties, the Equation 5.6 is equivalent to

$$\chi^2 = \sum_i \left[\frac{y_i - m_i \alpha_i}{\sigma_{i,stat}} \right]^2 + \sum_k (\beta^k)^2. \tag{5.9}$$

As a next step, the uncorrelated systematic errors are added to the statistical uncertainties in quadrature $\sigma_{i,stat}^2 + \sigma_{i,unc}^2$. The Equation 5.9 then takes the form

$$\chi^2 = \sum_i \frac{[y_i - m_i \alpha_i]^2}{\sigma_{i,stat}^2 + \sigma_{i,unc}^2} + \sum_k (\beta^k)^2. \tag{5.10}$$

The variables β^k can be used as fitting parameters to account for the systematic uncertainties [94]. The estimated set of parameters β^k resulting in the smallest χ^2 value would be the best model to correct for the systematic error of type k. Moreover, the minimisation of the β^k parameters can be done analytically [94]. This helps to solve technical problems when having too many fitting parameters β^k, accounting to all the sources of systematic errors in addition to the theory parameters $\boldsymbol{\theta}$. The value of the $\sum_k (\beta^k)^2$ will be latter referred to as χ^2 due to the correlations or as total correlated χ^2 value. An extensive discussion on the χ^2 function including the correlations can be found in [94, 95],

5.1.2 Bias corrections

The χ^2 function as defined in Equation 5.10 is known to suffer from biases in the region, where data has low statistics. The representation shown below

is the result developed during studies within the H1 collaboration [96, 97] in order to correct for this bias.

Many of the systematic uncertainties for cross section measurements have multiplicative nature, i.e. these are proportional to the cross section values. For multiplicative errors, measurements with smaller values have smaller uncertainties, which can introduce a bias in the χ^2 function. The absolute statistical uncertainty $\sigma_{i,stat}$ from Equation 5.9 is obtained from the relative $\delta_{i,stat}$ one, by scaling it with a measured value y_i. The relative statistical uncertainty is defined as

$$\delta_{i,stat} = \sigma_{i,stat}/y_i. \tag{5.11}$$

Usually the statistical uncertainty for the cross section measurement is calculated as

$$\sigma_{i,stat} = \sqrt{y_i}, \tag{5.12}$$

which gives a biased result. In order to correct for this bias the uncertainty should be calculated from the expected value

$$\sigma_{i,stat}^{corrected} = \sqrt{m_i}. \tag{5.13}$$

The corrected relative uncertainty is then

$$\delta_{i,stat}^{corrected} = \frac{\sqrt{m_i}}{\sqrt{y_i}}\frac{\sqrt{y_i}}{y_i} = \frac{\sqrt{m_i}}{\sqrt{y_i}}\delta_{i,stat} \tag{5.14}$$

From which one gets

$$\sigma_{i,stat}^{corrected} = y_i\delta_{i,stat}^{corrected} = y_i\frac{\sqrt{m_i}}{\sqrt{y_i}}\delta_{i,stat} = \sqrt{y_i m_i}\delta_{i,stat} \tag{5.15}$$

The number of observed events can also be modified by the effect of the correlated systematic uncertainties α_i. The Equation 5.10 takes the form of

$$\chi^2 = \sum_i \frac{[y_i - m_i\alpha_i]^2}{\delta_{i,stat}^2 y_i m_i \alpha_i + \delta_{i,unc}^2 m_i^2} + \sum_k (\beta^k)^2. \tag{5.16}$$

Since, σ_i from the Equation 5.1 is no longer constant with respect to $m(\boldsymbol{\theta})$, one should take into account also the logarithmic term in the χ^2 expression in Equation 5.16. The final form of the χ^2 function is given by the following

formula

$$\chi^2 = \sum_i \frac{[y_i - m_i\alpha_i]^2}{\delta_{i,\text{stat}}^2 y_i m_i \alpha_i + \delta_{i,\text{unc}}^2 m_i^2} \tag{5.17a}$$

$$+ \sum_k (\beta^k)^2 \tag{5.17b}$$

$$+ \sum_i \ln(\delta_{i,\text{unc}}^2 m_i^2 + \delta_{i,\text{stat}}^2 y_i m_i) \tag{5.17c}$$

$$- \sum_i \ln(\delta_{i,\text{unc}}^2 y_i^2 + \delta_{i,\text{stat}}^2 y_i^2). \tag{5.17d}$$

Here the terms Equation 5.17a and Equation 5.17b are equal to the formula Equation 5.16 and the non-constant logarithmic the term Equation 5.1 is given by term Equation 5.17c. While improving the χ^2 one would like not to shift the χ^2 value from the minimum, but rather to keep it close to the minimum of the unmodified χ^2. In order to compensate for the shift of the χ^2 minimum due to the additional logarithmic term, a compensating term given by Equation 5.17d is subtracted [97].

It is worth to repeat once again, that the χ^2 is minimised with the respect to the set of parameters $\boldsymbol{\theta}$ and β^k. So the β^k are considered to be nuisance parameters in the fit. The minimisation of the β^k variables can be and is done analytically, which restricts the problem to an effective χ^2 minimisation with respect to the theory parameters $\boldsymbol{\theta}$ only.

In case of the QCD analysis, the y_i correspond to the measured double differential NC and CC cross sections. The $\boldsymbol{\theta}$ parameters correspond to the PDF parameters, that are estimated by minimisation of the χ^2 function from Equation 5.17.

In case of the CI analysis, the y_i corresponds to the measured single differential NC cross section. The $\boldsymbol{\theta}$ parameters correspond to the CI effective coupling η. The CI analysis is using the χ^2 function from the Equation 5.16, since the modification made in Equation 5.17 was introduced after the analysis was published.

Chapter

6

QCD analysis

The QCD analysis is performed using the HERAFitter framework which is, among other contributions, based on the studies developed during this thesis. The HERAFitter framework is based on the QCDNUM [98] package, which describes the evolution of the PDFs and the MINUIT [99] package, which is used for the numerical minimisation of the χ^2 function. In addition to the mentioned software packages, there are modules responsible for the calculation of the structure functions taking into account state of the art treatment of the heavy quarks.

HERAFitter provides many tools to work with various physics processes, but the presented analysis focuses on DIS data only.

6.1 Data sets

The QCD analysis is based on 19 data sets, each containing double differential cross sections in x and Q^2. All of the low Q^2 ($Q^2 < 150\,\mathrm{GeV}$) data are combined into one data set, 7 sets correspond to the high Q^2 HERA I data, 10 to high Q^2 HERA II data and one set includes the data collected at the

end of the HERA II run with reduced energy of the proton beams. The total number of data point used in the fit is 1475. The data sets are listed in the Table 6.1. Data points are shown in Figure 5.1 kinematic ranges. As can be seen from the table, the data collected by the H1 detector covers a wide kinematic region. It covers the domain of x starting from a few 10^{-5}, mostly unexplored by the fixed target experiments, up to 0.65. In terms of Q^2 the data reaches very low values, down to $0.5\,\text{GeV}^2$, and very high values, more than $10^4\,\text{GeV}^2$.

6.1.1 Treatment of the data uncertainties

Along with the cross sections, the measurements provide a detailed information on the systematic uncertainties. The uncertainties on the measured cross sections are divided into three parts: statistical, uncorrelated and correlated systematic errors[1]. The statistical error is dominant for the high Q^2 region, while for the low Q^2 region, where the $e^{\pm}p$ cross section is largest, the impact of the systematic errors is usually larger. Due to the larger luminosity the high Q^2 measurements from the HERA II have a better statistical precision compared to those from HERA I. The systematic uncertainties are also considerably decreased compared to previous measurements. The main contribution to the total uncorrelated uncertainty is coming from the measurement of the electron and hadron energy. A crucial part of the correlated uncertainties is originating from the electron and hadron energy measurements, the determination of the angle of the scattered electron θ, background subtraction as well as luminosity and normalisation uncertainties. The exact numbers and detailed descriptions of the uncertainties on the measured inclusive cross sections can be found in [11, 64, 65, 67, 88].

The systematic uncertainties, which are correlated through the different data sets and taken into account in the fit are presented in the Table 6.2. A typical example of these systematic errors is the uncertainty on the luminosity. To account for the effect of correlations, the same nuisance parameter is used across the HERA II data sets. In the example of the luminosity uncertainty for the HERA II measurements, the same variable

---

[1]The uncorrelated and correlated systematic uncertainties may have the same origin. An error on the scattered lepton energy measurement is split to an uncorrelated and a correlated part and each of these parts contributes to the total uncorrelated and correlated uncertainties respectively.

Data set	$x_{\min}$	$x_{\max}$	$Q^2_{\min}$ (GeV^2)	$Q^2_{\max}$ (GeV^2)	Ref.	Centre of mass energy
e^+ low Q^2	0.00004	0.20	0.5	150	[67]	$\sqrt{s} = 301, 319$ GeV
e^+ low E_p	0.00003	0.003	1.5	90	[67]	$\sqrt{s} = 225, 252$ GeV
e^+ NC 94-97	0.0032	0.65	150	30 000	[64]	$\sqrt{s} = 301$ GeV
e^+ CC 94-97	0.013	0.40	300	15 000		
e^- NC 98-99	0.0032	0.65	150	30 000	[65]	$\sqrt{s} = 319$ GeV
e^- CC 98-99	0.013	0.40	300	15 000		
e^- NC 98-99 high y	0.00131	0.0105	100	800		$\sqrt{s} = 319$ GeV
e^- NC 99-00	0.0032	0.65	150	30 000	[88]	$\sqrt{s} = 319$ GeV; incl. high y
e^+ CC 99-00	0.013	0.40	300	15 000		$\sqrt{s} = 319$ GeV
e^- NC high y	0.0008	0.0105	60	800		$\sqrt{s} = 319$ GeV
e^- NC high y	0.0008	0.0105	60	800		$\sqrt{s} = 319$ GeV
e^+ NC L	0.002	0.65	120	30 000		
e^+ CC L	0.008	0.40	300	15 000		
e^+ NC R	0.002	0.65	120	30 000	[11]	$\sqrt{s} = 319$ GeV
e^+ CC R	0.008	0.40	300	15 000		
e^- NC L	0.002	0.65	120	50 000		
e^- CC L	0.008	0.40	300	30 000		
e^- NC R	0.002	0.65	120	30 000		$\sqrt{s} = 319$ GeV
e^- CC R	0.008	0.40	300	15 000		

Table 6.1: Table of data sets used in the QCD fit as well as the kinematic ranges in x and Q^2. Data sets with polarised lepton beam are indicated with L and R, which correspond to left or right polarisation. The table is adapted from the publication [11].

$\delta^{\mathcal{L}5}$ is used to represent the uncertainty for all HERA II data sets. The total number of sources of correlated uncertainties is 85.

Another challenge to deal with, is the treatment of polarised lepton beams at HERA II. HERA II data with polarised lepton beam. The measurement of the polarisation is another source of an experimental uncertainty to be taken into account. Since the polarisation affects the construction of the theoretical differential cross sections, it is treated differently than the other experimental systematics. The polarisation uncertainties are not entering the fit via β_i^j nuisance parameters, but have a separate set of free parameters assigned to them. Those parameters enter the calculation of the prediction and are fitted together with the PDF parameters. The effect is taken into account by allowing the polarisation to fluctuate within its uncertainties as

$$P_e^i = P_e^i \cdot (1 \pm \delta^{Pi}) \quad \text{with}$$
$$\delta^{Pi} = \delta_{\text{unc}}^i \cdot b_{\text{unc}}^i \oplus \gamma_{\text{TPOL}}^i \cdot b_{\text{TPOL}} \oplus \gamma_{\text{LPOL}}^i \cdot b_{\text{LPOL}}, \tag{6.1}$$

where index i represents the four different data running periods, δ_{unc} corresponds to the uncorrelated part of the uncertainty, γ_{TPOL} and γ_{LPOL} correspond to uncertainties of the two independent polarisation measurements[2], which are correlated across the HERA II data sets. One should note, that the uncorrelated uncertainties δ_{unc} are still correlated between different measurements within the same data set. The values of the uncertainty components δ_{unc}, γ_{TPOL}, and γ_{LPOL} are given in table 6.3. The parameters b_{unc}^i, b_{TPOL} and b_{LPOL} are free parameters of the QCD fit.

6.2 QCD settings

The differential cross sections are constructed from the proton structure functions, which in their turn are given by a sum of quark momentum distribution functions. At NLO the structure functions are obtained by convolution of the PDFs and calculable coefficient functions. There are various schemes of calculating the structure functions at NLO or NNLO. In the current analysis the calculation is done using Thorne-Roberts (TR) [21, 102] prescription in the variable-flavour number scheme (VFNS). This choice is later cross checked against the Aivazis-Collins-Olness-Tung (ACOT) scheme [25]. The PDFs are claimed to be independent of the chosen scheme,

---

[2]LPOL and TPOL indicate two independent polarimeters: Longitudinal Polarimeter [100] and Transverse Polarimeter [101].

Data set	$\delta^{\mathcal{L}}$		δ^E	δ^θ	δ^h	δ^N	δ^B	δ^V	δ^S	δ^{pol}
e^+ low Q^2	$\delta^{\mathcal{L}1}$									
e^+ low E_p	$\delta^{\mathcal{L}1}$									
e^+ NC 94-97	$\delta^{\mathcal{L}1}$	$\delta^{\mathcal{L}2}$	δ^{E1}	$\delta^{\theta1}$	δ^{h1}	δ^{N1}	δ^{B1}	—	—	—
e^+ CC 94-97	$\delta^{\mathcal{L}1}$	$\delta^{\mathcal{L}2}$	—	—	δ^{h1}	δ^{N1}	δ^{B1}	δ^{V1}	—	—
e^- NC 98-99	$\delta^{\mathcal{L}1}$	$\delta^{\mathcal{L}3}$	δ^{E1}	$\delta^{\theta2}$	δ^{h1}	δ^{N1}	δ^{B1}	—	—	—
e^- NC high y	$\delta^{\mathcal{L}1}$	$\delta^{\mathcal{L}3}$	δ^{E1}	$\delta^{\theta2}$	δ^{h1}	δ^{N1}	—	—	δ^{S1}	—
e^- CC 98-99	$\delta^{\mathcal{L}1}$	$\delta^{\mathcal{L}3}$	—	—	δ^{h1}	δ^{N1}	δ^{B1}	δ^{V2}	—	—
e^+ NC 99-00	$\delta^{\mathcal{L}1}$	$\delta^{\mathcal{L}4}$	δ^{E1}	$\delta^{\theta2}$	δ^{h1}	δ^{N1}	δ^{B1}	—	δ^{S1}	—
e^+ CC 99-00	$\delta^{\mathcal{L}1}$	$\delta^{\mathcal{L}4}$	—	—	δ^{h1}	δ^{N1}	δ^{B1}	δ^{V2}	—	—
e^+ NC high y	$\delta^{\mathcal{L}5}$	$\delta^{\mathcal{L}6/\mathcal{L}7}$	δ^{E2}	$\delta^{\theta3}$	δ^{h2}	δ^{N2}	—	—	δ^{S2}	—
e^- NC high y	$\delta^{\mathcal{L}5}$	$\delta^{\mathcal{L}8/\mathcal{L}9}$	δ^{E2}	$\delta^{\theta3}$	δ^{h2}	δ^{N2}	—	—	δ^{S2}	—
e^+ NC L	$\delta^{\mathcal{L}5}$	$\delta^{\mathcal{L}6}$	δ^{E2}	$\delta^{\theta3}$	δ^{h2}	δ^{N2}	δ^{B1}	—	—	δ^{P1}
e^+ CC L	$\delta^{\mathcal{L}5}$	$\delta^{\mathcal{L}6}$	—	—	δ^{h2}	δ^{N3}	δ^{B1}	δ^{V3}	—	δ^{P1}
e^+ NC R	$\delta^{\mathcal{L}5}$	$\delta^{\mathcal{L}7}$	δ^{E2}	$\delta^{\theta3}$	δ^{h2}	δ^{N2}	δ^{B1}	—	—	δ^{P2}
e^+ CC R	$\delta^{\mathcal{L}5}$	$\delta^{\mathcal{L}7}$	—	—	δ^{h2}	δ^{N3}	δ^{B1}	δ^{V3}	—	δ^{P2}
e^- NC L	$\delta^{\mathcal{L}5}$	$\delta^{\mathcal{L}8}$	δ^{E2}	$\delta^{\theta3}$	δ^{h2}	δ^{N2}	δ^{B1}	—	—	δ^{P3}
e^- CC L	$\delta^{\mathcal{L}5}$	$\delta^{\mathcal{L}8}$	—	—	δ^{h2}	δ^{N3}	δ^{B1}	δ^{V3}	—	δ^{P3}
e^- NC R	$\delta^{\mathcal{L}5}$	$\delta^{\mathcal{L}9}$	δ^{E2}	$\delta^{\theta3}$	δ^{h2}	δ^{N2}	δ^{B1}	—	—	δ^{P4}
e^- CC R	$\delta^{\mathcal{L}5}$	$\delta^{\mathcal{L}9}$	—	—	δ^{h2}	δ^{N3}	δ^{B1}	δ^{V3}	—	δ^{P4}

Table 6.2: Correlation of systematic error sources across different data sets. The table entries indicate the correlation of the error sources across the data sets, where each numerical index corresponds to a fit parameter for the given error source. For each of the nine correlated systematic error sources one or more parameters are included in the fit procedure. The sources considered are due to the luminosity uncertainty ($\delta^{\mathcal{L}}$), the electron energy uncertainty (δ^E), the electron polar angle measurement (δ^θ), the hadronic energy uncertainty (δ^h), the uncertainty due to noise subtraction (δ^N), the background subtraction error (δ^B), the uncertainty in the measurement of the ratio V_{ap}/V_p (δ^V), the error of the background charge asymmetry (δ^S), and the error of the polarisation measurement (δ^{pol}). The table is adapted from the publication [11].

δ^{Pi} (Period)	δ_{unc} (%)	γ_{LPOL} (%)	γ_{TPOL} (%)
δ^{P1} (e^+L)	1.7	0.34	0.36
δ^{P2} (e^+R)	2.0	0.48	0.37
δ^{P3} (e^-L)	2.6	0.59	0.53
δ^{P4} (e^-R)	2.7	0.55	0.58

Table 6.3: Uncorrelated and correlated uncertainties on the polarisation measurement for each of the HERA II running periods.

which is true for very high orders. In this case the determination and interpretation of the PDFs has to be done in the frame of the chosen scheme, whereas the available orders are NLO and NNLO. While presenting the method and results of the QCD analysis the RT scheme is meant by default unless a different one is mentioned.

The evolution equations yield the PDFs at all values of Q^2, if they are given as a function of x at some starting scale of Q_0^2. The evolution starts with three active flavours, u, d, s. Their number increases as the value of the four-momentum transferred reaches the thresholds $Q_{c,b,t}^2$ equal to the mass of the particular quark. In the current analysis the input scale is chosen to be $Q_0^2 = 1.9\,\text{GeV}^2$, which is below the mass of the charm quark. On the other hand, one would not like to choose the starting scale much lower in order to stay in the region, where perturbative QCD is applicable. So the chosen value is kind of a compromise.

The main QCD parameters are the coupling constant α_s and the masses of the quarks. In order to determine the PDFs some assumptions for these parameters are needed. For the current analysis the light quarks, u, d, s, are considered to be massless, since the starting scale is chosen much higher than the masses of the quoted quarks. The heavy quark masses are chosen to be $m_c = 1.4\,\text{GeV}$ for charm and $m_b = 4.75\,\text{GeV}$ for beauty[3]. The strong coupling constant is fixed to the world average $\alpha_s = 0.1176$ [4].

The minimum invariant mass of the hadronic final system W of the HERA data is $15\,\text{GeV}^2$, so that corrections due to the mass of the target can be neglected. The maximum value for x is 0.65, such that data are insensitive

---

[3]One should note, that the mass of the top quark is high with respect to the four-momentum transferred at HERA and thus the top quark contribution is neglected in the current analysis.

to large x higher twist effects [103]. To insure that the perturbative QCD is applicable, only the data with a minimum Q^2 value of $3.5\,\mathrm{GeV}^2$ is used in the analysis.

6.3 PDF extraction

6.3.1 Parametrisation

The choice of the parametrisation generally depends on the sensitivity of the data. In the current analysis the parametrised PDFs are chosen to be the valence quark distributions xu_v, xd_v, the up-type, $xU = x(u+c)$, down-type, $xD = x(d + s + b)$ distributions along with the anti-quark distributions $x\overline{U} = x\overline{u} + x\overline{c}$ and $x\overline{D} = x\overline{d} + x\overline{s} + x\overline{b}$ and the gluon distribution $xg(x)$. The sensitivity to the gluon and sea distribution is coming from the NC data, while the CC data is sensitive to the valence quark distribution (difference if q and $\overline{q}$).

A simple generic functional form is chosen for the parametrisation

$$xf_i(x, Q_0^2) = A_i x^{B_i}(1 - x)^{C_i} P_i(x), \tag{6.2}$$

where the index i runs over all parametrised partons. The parameter A is responsible for the normalisation, the parameter B describes the low x behaviour, suggested by Regge phenomenology, where the behaviour of the sea and gluon distribution is $1/x$-like and the valence distributions have approximately $\sqrt{x}$ dependence. The fact that at high x all of the distributions drop to 0 is ensured by the C parameter. The intermediate region is a result of interpolation between the low and high x shapes. The $P_i(x)$ is a polynomial correction function, which allows an additional freedom for the parametrisation to insure a better description of the data.

The following functional forms are considered for the quark and gluon distributions:

$$\begin{aligned} xf(x) &= A_f x^{B_f}(1 - x)^{C_f}(1 + D_f x + E_f x^2), \\ xg(x) &= A_g x^{B_g}(1 - x)^{C_g}(1 + D_g x + E_g x^2) - A'_g x^{B'_g}(1 - x)^{C'_g}, \end{aligned} \tag{6.3}$$

where f corresponds to the $u_v, d_v, \overline{U}, \overline{D}$ and A, B, C, D, E are the parameters of the fit.

The functional form for the gluon allows extra flexibility in the low x region. C'_g is set to 25 in order to suppress a negative contribution at high x. This number is used as suggested by the MSTW2008 fit [84], since this fit only based on the H1 $e^{\pm}p$ data shows no sensitivity to the C'_g and releasing this parameter brings no change to the results.

The PDFs must satisfy the sum rules, which are described in chapter 2, however the H1 data have a limited kinematic coverage and little sensitivity to the flavour decomposition of the sea. Thus additional assumptions are required and are discussed in the following.

In order to find the optimal parametrisation a scan in the parameter space is performed. The scanning procedure starts from a basic functional form with 9 free parameters $A_{\overline{D}}, B_g, B_{u_v}, B_{\overline{D}}, C_g, C_{u_v}, C_{d_v}, C_{\overline{U}}, C_{\overline{D}}$. The normalisation parameters, A_{u_v} and A_{d_v}, are constrained by the quark number sum rules and A_g by the momentum sum rule that are discussed in chapter 2 and are not treated as free parameters in the fit. In the low x region the valence quark distributions are expected to vanish and the distributions of up-type and down-type to be equal. To ensure it, the parameters B for $x\overline{U}$ and $x\overline{D}$ distributions are required to be equal. The parameters B for the valence distributions are also set equal at the beginning, however this assumption is released during the parameter scan. Further constraints are required for further disentangling the individual contributions of different flavours. The strange quark distribution is expressed as an x-independent fraction to reduce the number of free parameters, f_s, of the d-type sea, $f_s = x\overline{s}/x\overline{D}$, at the starting scale, with $f_s = 0.31$ as preferred by neutrino-induced di-muon production [104]. The normalisation parameters of the sea distributions are than constrained by the relation $A_{\overline{U}} = A_{\overline{D}}(1 - f_s)$. The parameters D and E are fixed to 0. The fit with the smallest χ^2 value is considered to have the best set of 9 parameters.

To improve the description of the data additional parameters are then introduced in the fit one at a time in an iterative procedure. The fit resulting in the lowest χ^2 is chosen as the best 10 parameter fit. An additional 11th parameter is added into the fit and so on. The scanning procedure is repeated by iteratively adding one parameter at a time and finding the best set of parameters. The process is continued until no significant improvement in χ^2 is obtained. However, the central fit should not only have the smallest χ^2 value, but also satisfy the criteria that the structure functions are positive and $xd_v > x\overline{d}$ at large x.

N_{DoF}	N_{param}	Parameters	E_{u_v}	D_{u_v}	D_g	$D_{\overline{D}}$	$D_{\overline{U}}$	D_{d_v}	B_{d_v}	A'_g, B'_g
1464	10	$9p+$	**1584**	1625	1665	1628	1674	1617	1665	1603
1463	11	$9p + E_{u_v}+$	—	1583	1584	1583	1583	1578	**1574**	1576
1462	12	$9p + E_{u_v} + B_{d_v}+$	—	1574	1574	1574	1574	1574	—	$\boxed{\textbf{1569}}$
1460	14	$9p + E_{u_v} + B_{d_v} + A'_g + B'_g+$	—	1568	1569	1568	1569	1569	—	—

Table 6.4: The χ^2 values resulting from the parametrisation scan starting from 10 parameters fit. The first column shows the number of degrees of freedom corresponding to the number of free parameters given in the second column. In the third column $9p$ indicates a minimal set of free parameters, which are $A_{\overline{D}}$, B_g, B_{u_v}, $B_{\overline{D}}$, C_g, C_{u_v}, C_{d_v}, $C_{\overline{U}}$, $C_{\overline{D}}$. The smallest χ^2 value for each row is highlighted. The χ^2 value for the central fit is indicated by a box.

The results of the parametrisation scan in terms of χ^2 values are summarised in Table 6.4. The scanning procedure includes all the possible combinations of the available parameters, while the table contains only the parameters, to which the fit is the most sensitive. One should also note, that the negative gluon condition contains two free parameters, A'_g and B'_g. So in the Table 6.4, the column corresponding to the negative gluon condition has actually one more parameter than the other fits in the same row. The first row of the table shows the χ^2 values of various ten parameter fits. The best result is achieved by adding E_{u_v} parameter, which considerably improves the fit compared to the others. The E_{u_v} parameter is then used together with the basic nine parameters in the next steps. The second row corresponds to eleven parameters fit, where the best result is achieved by varying B_{d_v} parameter in addition to the basic ten. From the χ^2 one can see that the fits have much closer results (in terms of χ^2) than in the previous step, although the best fit is still up to 10 units better. This is due to the fact that the parametrisation is more flexible compared to the one with only ten free parameters. In the next step, where twelve free parameters are fitted, the results are almost identical for most of the cases except for the condition with a negative gluon. Giving additional flexibility to the gluon noticeably improves the fit, in the case where other parameters have reached the limit of their sensitivity.

It becomes clear from the fourth row of the Table 6.4, that fit has reached its maximum level of flexibility and shows no more improvement. The best fit contains 9 basic parameters, which were mentioned previously plus E for the valence up quark, B for the valence down quark and the condition allowing a negative contribution for the gluon at low x region, which contains the two additional parameters A'_g and B'_g. The more flexible parametrisation of the valence distributions indicates the sensitivity of the H1 data to the valence and especially to the up quark. The resulting parametrisation at the starting scale Q_0^2 are

$$xg(x) = A_g x^{B_g}(1-x)^{C_g} - A'_g x^{B'_g}(1-x)^{25} , \tag{6.4a}$$

$$xu_v(x) = A_{u_v} x^{B_{u_v}}(1-x)^{C_{u_v}} \left(1 + E_{u_v} x^2\right) , \tag{6.4b}$$

$$xd_v(x) = A_{d_v} x^{B_{d_v}}(1-x)^{C_{d_v}} , \tag{6.4c}$$

$$x\overline{U}(x) = A_{\overline{U}} x^{B_{\overline{U}}}(1-x)^{C_{\overline{U}}} , \tag{6.4d}$$

$$x\overline{D}(x) = A_{\overline{D}} x^{B_{\overline{D}}}(1-x)^{C_{\overline{D}}} . \tag{6.4e}$$

After finding the optimal values for the fitted parameters, the uncertainties

of the PDFs have to be determined. The next subsection is dedicated to various sources of the PDF uncertainties and methods of their estimation.

6.4 Uncertainties on PDFs

Uncertainties on the determined PDFs occur due to different reasons. A considerable part of the errors originate from the precision of the analysed data and is usually denoted as experimental uncertainty. The assumptions made for the QCD parameters, like quark masses, are also potential sources of errors. Those are called model uncertainties. Another principal source of inaccuracy is the choice of parametrisation. The used methods for the determination of each of the uncertainty types are described below. The total PDF uncertainty is obtained by the square root of the experimental, model and parametrisation uncertainties added in quadrature.

6.4.1 Experimental uncertainties

There is no unique approach to study uncertainties in the QCD analysis. In the current analysis two different methods were considered. One of the efficient ways of the study is known as Hessian method. The method is based on a Taylor expansion of the χ^2 function up to second order near its global minimum. The details of the method are given in [105, 106]. However this method is based on the assumption that the uncertainties have a Gaussian shape, which is not necessarily true.

An alternative method of error estimation is based on Monte Carlo toy studies [107]. The technique consists of generating a set of toy cross sections by fluctuating the measured cross sections within their systematic errors. The advantage of the method is, that for each error source, the data points can be fluctuated according to any kind of distribution. This works perfectly for statistical and uncorrelated uncertainties, however for the correlated systematics one should take into account that the random shifts of one data point may affect all the other points as well. So in case of the correlated systematics, the random shifts occur with the same probability for each of the data points.

The procedure is repeated N times for each of the data sets used in the central QCD fit. The larger the number of toy replicas is, less is the

room for possible fluctuations. For the currents analysis $N = 400$ is used, which provides a stable and reliable result. For each of the toy replica a complete NLO QCD fit is performed and, as a result, N number of PDFs are determined. The experimental uncertainties are obtained by calculating the root-mean-squared (rms) of the PDF sets extracted from the toy replicas.
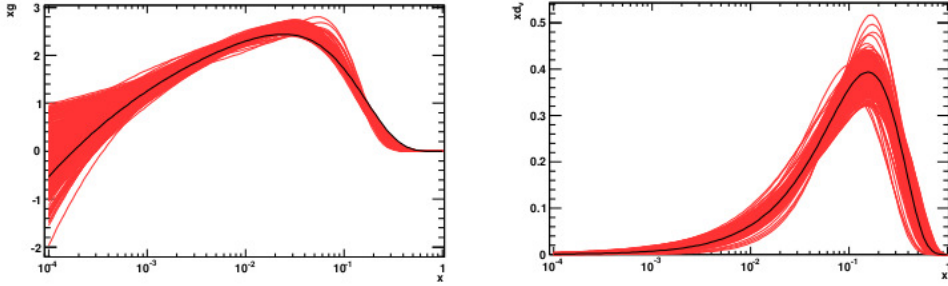

Figure 6.1: Distributions of the d quark and gluon obtained from fits to toy replicas (red lines). The black lines indicate the distributions obtained from the central fit to data.

An example of distributions for the d quark and the gluon obtained from fits to toy replicas is shown in Figure 6.1. Fits to individual toy replicas are indicated by the red lines, while the black line corresponds to the central fit to data. The study of the individual replicas shows that they are grouped around two different solutions. One of the solutions prefers a slightly suppressed d_{val} distribution and increased contribution of the $\overline{D}$.

The mean distributions obtained from the fit to smeared replicas do not necessarily match the distribution obtained from the fit to data. A comparison of the mean distributions obtained from the toys and the distributions from the data for the gluon and u quark distributions is shown in Figure 6.2. If the mean distributions match the central distributions the rms is obtained as an experimental uncertainty around the central distribution. If the mean distributions and the central distributions do not match, the uncertainties form an asymmetric error band around the central parton distributions.

By construction, the Hessian method is not sensitive to multiple minima. This leads to an underestimation of the experimental errors by the Hessian method, while the Monte Carlo technique shows a more reasonable result. Therefore for the estimation of experimental uncertainties on the PDFs the
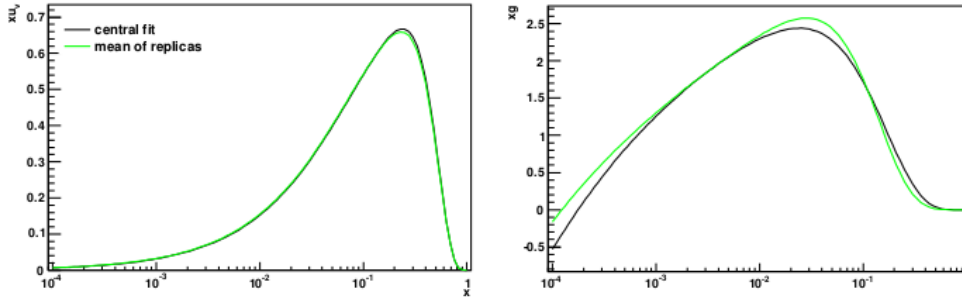
Figure 6.2: Distributions of the u quark and gluon obtained from fits to toy replicas (green lines) and from the data (black lines).

Monte Carlo method is used and the Hessian is considered only as a cross check.

6.4.2 Model uncertainties

In section 6.2 assumptions concerning the QCD parameters are made. These assumptions are based on the current experimental and theoretical knowledge. However, as more measurements are done, the values for the QCD parameters might appear to be different from the ones obtained before. This is taken into account by assigning a model uncertainty to the determined PDFs.

Model uncertainties are evaluated by varying the input assumptions up and down. Each of the input parameters is varied separately and for each of the variations the fit procedure is repeated. The values of the parameters chosen for the central fit, as well as their variations are summarised in Table 6.5. PDFs are determined for the model parameters varied within their variances. To calculate the total model uncertainty, the difference between the central fit and the fit corresponding to the model variations are added in quadrature. The procedure is done for the up and down variations separately.

The effect of the individual variations is summarised in the Table 6.6 in terms of χ^2 values[4]. As can be seen from the table, the variation of the minimum cut on the Q^2 value has the dominant impact on the fit. The

---

[4]The variation of the starting scale is rather considered to be a parametrisation uncertainty than a model one and thus is discussed together with parametrisation uncertainties

Parameter	Central Value	Lower Limit	Upper Limit
f_s	0.31	0.23	0.38
$m_c\,(\mathrm{GeV})$	1.4	1.35	1.65
$m_b\,(\mathrm{GeV})$	4.75	4.3	5.0
$Q^2_{\min}\,(\mathrm{GeV}^2)$	3.5	2.5	5.0
$Q^2_0\,(\mathrm{GeV}^2)$	1.9	1.5	2.5

Table 6.5: Central values of input parameters to the QCD fit and their variations. For the m_c variation downwards the starting scale Q^2_0 should also be changed to a lower value of $1.8\,\mathrm{GeV}^2$ for consistency. For the Q^2_0 starting scale variations, the values of the parameters f_s and m_c should also be changed.

minimum Q^2 value of the data mainly affects the region of low x values, where the largest deviation from the central fit is observed. Figure 6.3 shows distributions for $\overline{D}$ and gluon for up and down variations of the Q^2_{min} cut.
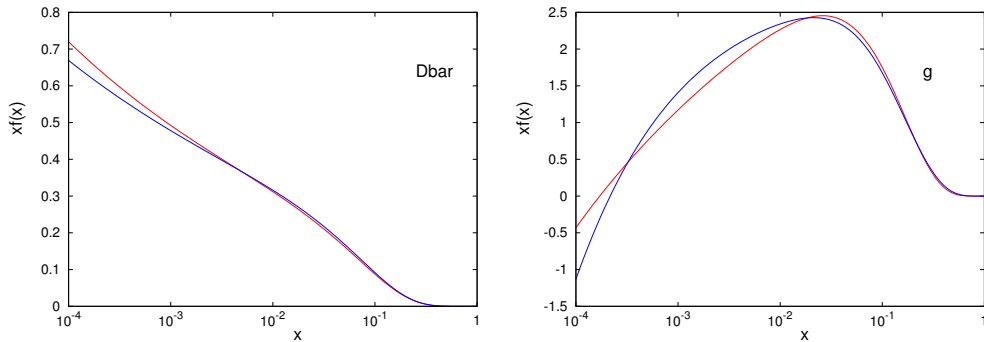
Figure 6.3: Distribution of the $\overline{D}$ and gluon for variations of the Q^2_{min} cut. The red line corresponds to the variation down and the blue line corresponds to the upwards variation.

The strange quark fraction is varied between 0.23 and 0.38 [84]. The variation is mainly affecting the sea distribution, but shows a small impact on the uncertainties. The very recent results from the ATLAS collaboration [108] showed that the strange quark is less suppressed than was assumed. The

Parameter	χ^2_{up}	χ^2_{down}	$\chi^2_{central}$
f_s	1570	1568	1569
m_c	1581	1566	1569
m_b	1570	1567	1569
$Q^2_{\min}$	1515	1604	1569

Table 6.6: The χ^2 values corresponding to the up and down variations of the model parameters. One should note, that number of degrees of freedom for the variation of the Q^2_{min} cut is different. For variation up there are less data points included in the fit than in down case.

strangeness fraction is found to be $f_s = 0.5$, which exceeds the variation range for f_s considered in the presented analysis. This value of f_s is also studied in order to check the impact on the fit. Using the value $f_s = 0.5$ has a noticeable impact on the sea distribution. However, the results of the fit are still in an agreement with the H1PDF 2012 fit within the total uncertainties.

The variation of charm and bottom quark masses has very small impact on the distributions. The total model uncertainty is built by adding up the difference between the central fit and the fits corresponding to variations of f_s, $Q^2_{\min}$, m_c and m_b parameters in quadrature. The positive and negative deviations are added separately.

6.4.3 Parametrisation uncertainties

As was shown in the subsection 6.3.1, the central parametrisation contains 13 parameters. Adding one more parameter does not bring significant improvement, but 14 parameter fits are considered as possible variations. Together with the variation of the starting scale Q^2_0, they are considered as parametrisation uncertainty. The uncertainties are constructed as an envelope built from the maximal deviation at each x value from the central fit.

The results of the 14 parameter fits do not differ much from the central 13 parameter fit. The dominant source of the parametrisation uncertainty is the variation of Q^2_0. It mostly affects the PDF uncertainties of the sea and

gluon distributions at small x. The effect of the variation of the starting scale is illustrated in the Figure 6.4 for $\overline{D}$ and gluon distributions.
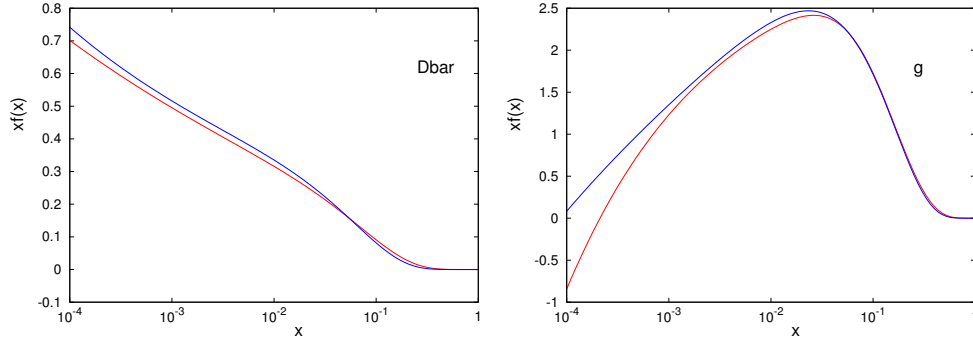

Figure 6.4: Distribution of the $\overline{D}$ and gluon for variations of the starting scale Q_0^2. The red line corresponds to the variation down and the blue line corresponds to the upwards variation.

6.4.4 Total uncertainties

The total uncertainties on the determined parton distributions are estimated by adding the experimental, model and parametrisation uncertainties in quadrature. The uncertainties are largest at the starting scale. Due to the evolution, the total uncertainties considerably decrease at the low x with increasing of the Q^2.

6.5 Fit results and comparisons

6.5.1 The χ^2 values

The measured CC and NC cross sections show a good agreement with the performed fit in the whole kinematic space. The QCD fit results in a total χ^2 per degree of freedom 1569.6/1461. In Table 6.7 the χ^2 values for individual data sets are summarised. One should note that values given in the table correspond to the statistical and uncorrelated systematic uncertainties and do not include the value that corresponds to the correlated systematic uncertainties. The total correlated χ^2 value, as defined in subsection 5.1.1, is 67.4.

Data Set	Number of data points	χ^2 (unc. err.)
e^+ low Q^2	171	196
e^+ low E_p	124	132
e^+ NC 94-97	130	92
e^+ CC 94-97	25	22
e^- NC 98-99	126	113
e^- NC 98-99 *high y*	13	5.4
e^- CC 98-99	28	19
e^+ NC 99-00	147	144
e^+ CC 99-00	28	29
e^+ NC *high y*	11	5.6
e^- NC *high y*	11	7.7
e^+ NC *L*	137	124
e^+ CC *L*	28	46
e^+ NC *R*	138	138
e^+ CC *R*	29	40
e^- NC *L*	139	174
e^- CC *L*	29	27
e^- NC *R*	138	142
e^- CC *R*	28	16

Table 6.7: Results of the H1PDF 2012 fit. For each data set the number of data points are given, along with the χ^2 contribution. The table is taken from [11].

6.5.2 Correlated shifts

As an example Table 6.8 lists luminosity normalisation factors for each data period obtained from the QCD fit. The factors are calculated from the systematic shifts, as defined in subsection 5.1.1. The table shows the effect of individual and global normalisation shifts, as well as the combination of those two.

The fit requires the luminosity of the HERA I data to be globally lowered by 0.7% and the HERA II data to be raised by 2.9%, which corresponds to $1.3\,\sigma$ systematic shift. Most of the other systematic shifts are less than 1σ. However some of the systematic shifts of the combined low Q^2 data and

Data Period	Global Normalisation	Per Period Normalisation	Total Normalisation
e^+ Combined low Q^2	0.993	–	0.993
e^+ Combined low E_p	0.993	–	0.993
HERA I e^+ 94-97	0.993	0.999	0.992
HERA I e^- 98-99	0.993	1.003	0.996
HERA I e^+ 99-00	0.993	1.005	0.998
HERA II e^+ L	1.029	0.991	1.020
HERA II e^+ R	1.029	1.013	1.042
HERA II e^- L	1.029	1.010	1.039
HERA II e^- R	1.029	1.014	1.043

Table 6.8: Factors corresponding to the global luminosity normalisations ($\mathcal{L}1$, $\mathcal{L}5$), the normalisation for each data period ($\mathcal{L}2$, $\mathcal{L}3$, $\mathcal{L}4$ for HERA I and $\mathcal{L}6$, $\mathcal{L}7$, $\mathcal{L}8$, $\mathcal{L}9$ for HERA II), and the overall combined normalisation of the data sets as determined by the QCD fit [11].

combined low proton beam energy data result in 1.7 to $2.9\,\sigma$ shifts. The large shifts for these data sets are caused by the TR scheme, which is not describing the low Q^2 data very well. This effect has been already observed in the F_L structure function measurement by the H1 collaboration [67]. The distribution of the systematic shifts is presented in Figure 6.5.

The cross checks done using the ACOT scheme show a better description of particularly low energy and Q^2 data sets. The systematic shifts in this case are about 0.5 to 1.5 standard deviations. More details on the cross check with the ACOT scheme are presented in subsection 6.5.6.

6.5.3 Pull distributions

In order to quantify the results of the fit a variable p_i named pull is introduced. The pull of a point i is defined as

$$p_i = \frac{y_i - m_i \alpha_i}{\sqrt{\delta_{i,\mathrm{unc}}^2 m_i^2 + \delta_{i,\mathrm{stat}}^2 y_i m_i \alpha_i}}. \tag{6.5}$$
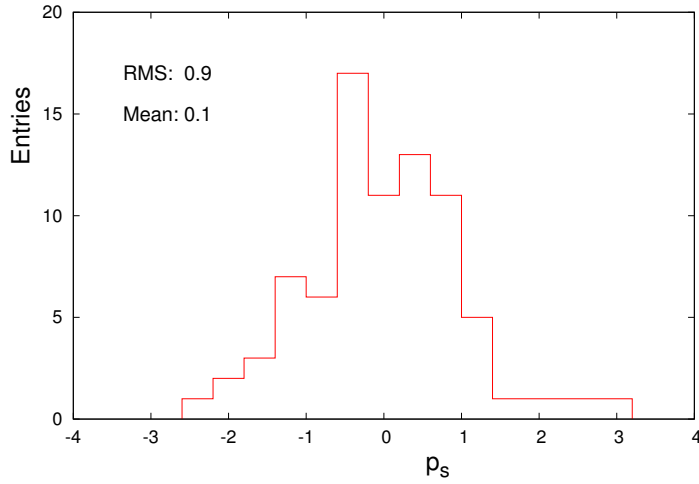
Figure 6.5: Distribution of the systematic shifts including normalisation, as defined in subsection 5.1.1, of the full H1 inclusive data sample used in the fit.

Ideally, if the data is perfectly described by the scaled theoretical predictions $m_i\alpha_i$, the expected distribution of the pulls is Gaussian around 0 with a RMS of 1. The Figure 6.6 and Figure 6.7 show the distribution of the pulls for the individual data sets of the HERA I and HERA II running periods respectively. As can be seen from Figure 6.6, for measurements of HERA I the distributions of pulls is almost Gaussian with mean values of 0 or very close to it and RMS values close to 1. In case of the NC e^-p high y data sample the mean is shifted a bit more than for the other data sets. However this measurement as well as CC HERA I measurements, has very few data points, which makes it difficult to quantify the pull distribution statistically. The same situation is with HERA II data pull distributions. The pulls have Gaussian like shape with RMS very close to 1 and mean close to 0. The CC and NC high y measurements have less data points compared to other NC measurements, which results in non Gaussian shape of the pull distributions. However, the fit results show no serious tensions for the full kinematic range of NC and CC measurements.
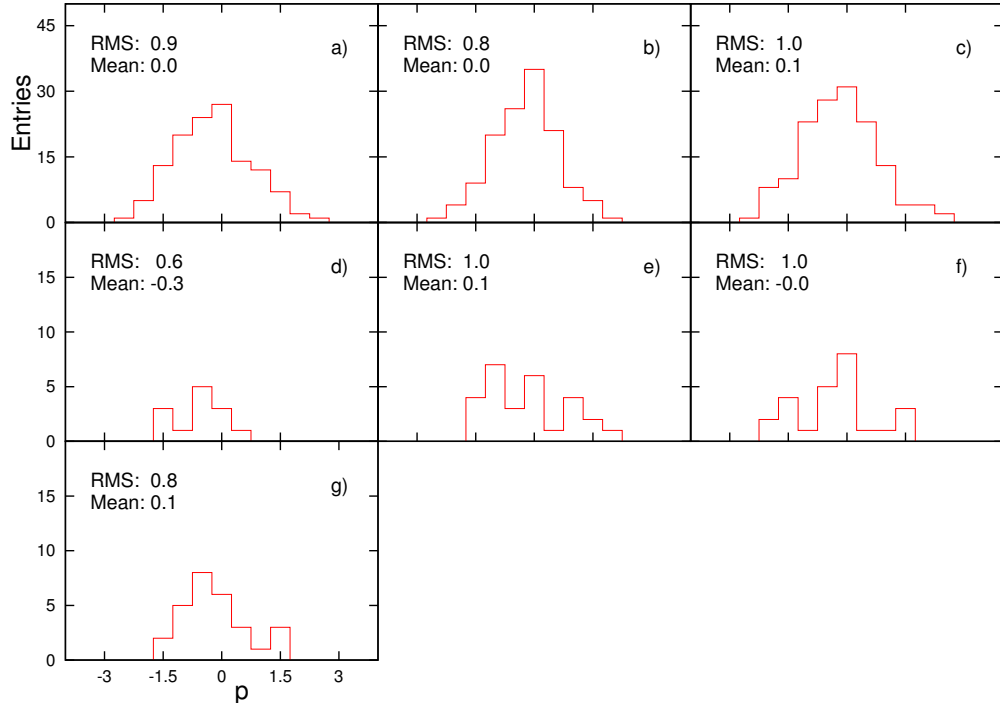
Figure 6.6: Distribution of pulls p for the HERA I data sample. The data sets are the following: a) e^- NC 98-99, b) e^+ NC 94-97, c) e^+ NC 99-00, d) e^- NC 98-99 high y, e) e^- CC 98-99, f) e^+ CC 94-97, g) e^+ CC 99-00.

6.5.4 Effect of polarisation

The measured polarisation values are also varied within their uncertainties in the fit. The corresponding shift parameters are minimised together with the PDF parameters and are shown in table Table 6.9. The polarisation shifts show very small impact on the results and a weak correlation with the actual PDF parameters.

6.5.5 PDF results

The PDF parameters obtained from the fit are presented in Table 6.10.

The correlations between parameters obtained from the fit are given in Table A.1. The parton distribution functions obtained from the fit are presented in Figure 6.8 and Figure 6.9. The valence quark distributions as well
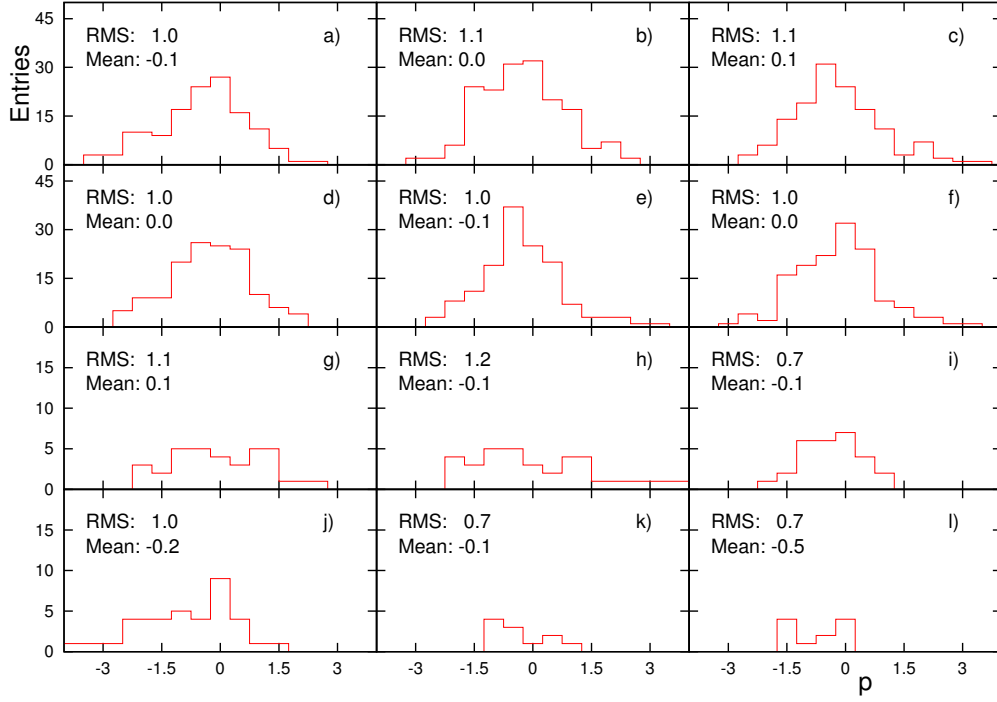
Figure 6.7: Distribution of pulls p for the HERA II data sample. The data sets are the following: a) e^+ low E_p, b) e^+ low Q^2, c) e^- NC LH, d) e^- NC RH, e) e^+ NC LH, f) e^+ NC RH, g) e^+ CC RH, h) e^+ CC LH, i) e^- CC RH, j) e^- CC LH, k) e^+ NC high y, l) e^- NC high y. Labels LH and RH indicate the left and right polarisation of the lepton beam.

Parameter	Central value	Global correlation
$b_{\text{unc}}^{1(e^+pL)}$	0.16	0.07
$b_{\text{unc}}^{2(e^+pR)}$	0.19	0.09
$b_{\text{unc}}^{3(e^-pL)}$	-0.32	0.10
$b_{\text{unc}}^{4(e^-pR)}$	0.50	0.09
b_{TPOL}	0.11	0.05
b_{LPOL}	0.11	0.05

Table 6.9: Central values of the parameters corresponding to the polarisation shifts together with the correlation coefficients. The global correlation coefficients represent the level of correlation between the polarisation parameters and the PDF parameters. The definition of the global correlation coefficient is given in Appendix A.

as the gluon and the see distributions are presented at the starting scale $Q_0^2 = 1.9\,\text{GeV}^2$ and evolved to $Q^2 = 10\,\text{GeV}^2$. The experimental, model and parametrisation uncertainties are shown separately by the red, yellow and green bands respectively. In addition, the fit result with a strangeness fraction $f_s = 0.5$ is presented by the dashed blue line. The variation of the parameter f_s for the determination of the model uncertainties did not include the value of 0.5, however the PDFs from this fit still shows an agreement with the H1PDF 2012 set within the uncertainties of the latter.

By using the precise information of the HERA II inclusive NC and CC cross sections in addition to already studied HERA I data in the QCD analysis, one would expect to increase the accuracy of the obtained PDFs. In order to check the impact of the HERA II data, a QCD fit of the HERA I data alone is performed using the same settings and repeating the same procedure as for H1PDF 2012 fit. The experimental uncertainties are determined using the MC method. The toy replicas are generated from the expected cross sections by fluctuating them within uncertainties of the HERA I and once within the uncertainties of HERA II data. The obtained experimental errors are compared in the Figure 6.10, where the ratio of different PDFs obtained from the fit to the HERA I toy data only and the H1PDF 2012 set is shown. The new high Q^2 data have a visible impact on all distributions, especially in the xD distribution.

Parameter	Central value	Experimental uncertainty
B_g	0.02	0.03
C_g	6.40	0.31
A'_g	0.30	0.09
B'_g	-0.27	0.03
B_{u_v}	0.70	0.02
C_{u_v}	4.90	0.07
E_{u_v}	12.27	1.17
B_{d_v}	0.97	0.07
C_{d_v}	5.19	0.41
$C_{\bar{U}}$	3.41	0.41
$A_{\bar{D}}$	0.17	0.01
$B_{\bar{D}}$	-0.15	0.01
$C_{\bar{D}}$	9.73	2.24

Table 6.10: Parameters of the central fit and experimental uncertainties obtained as an RMS from the monte carlo replicas.
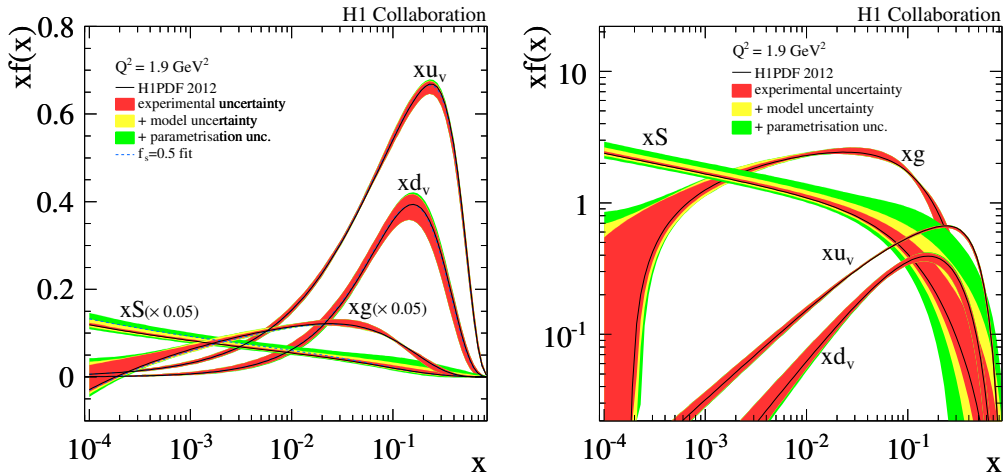
Figure 6.8: Parton distribution functions of H1PDF 2012 at the starting scale $Q^2 = 1.9\,\mathrm{GeV}^2$. The gluon and sea distributions in the linear scale plot (left) are scaled by a factor 0.05. The PDFs with $f_s = 0.5$ are also shown (dashed). The uncertainties include the experimental uncertainties (inner), the model uncertainties (middle) and the parametrisation variation (outer). All uncertainties are added in quadrature. The plots are taken from [11].
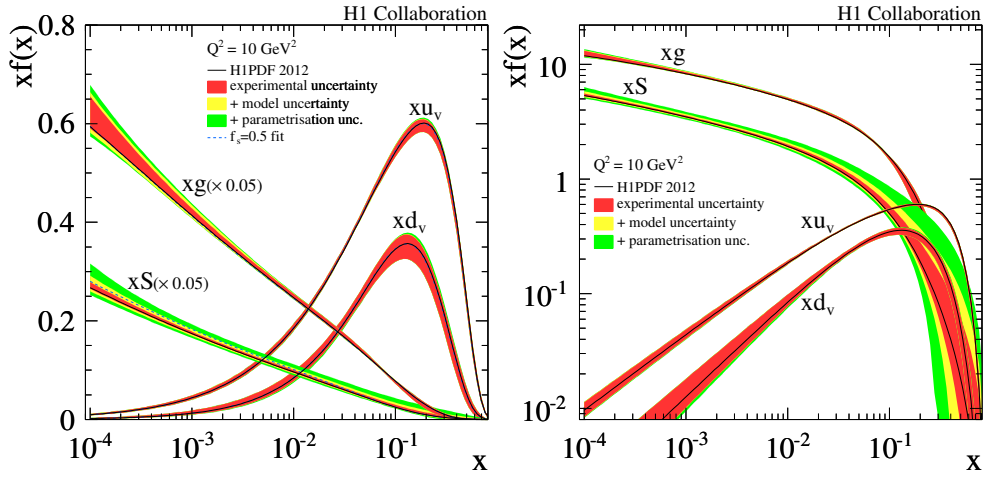
Figure 6.9: Parton distribution functions of H1PDF 2012 at the evolved scale of $10\,\text{GeV}^2$. The gluon and sea distributions in the linear scale plot (left) are scaled by a factor 0.05. The PDFs with $f_s = 0.5$ are also shown (dashed). The uncertainties include the experimental uncertainties (inner), the model uncertainties (middle) and the parametrisation variation (outer). All uncertainties are added in quadrature. The plots are taken from [11].
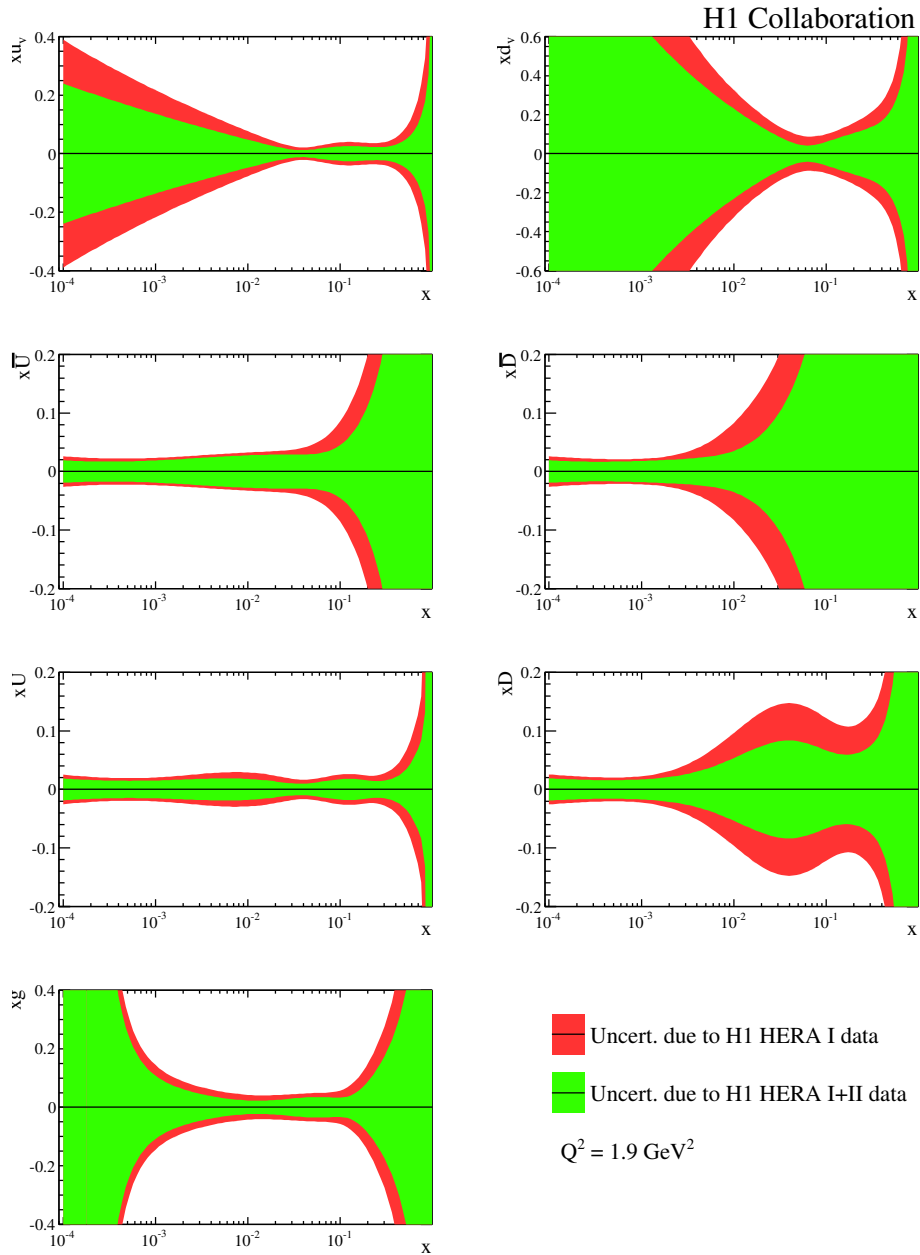
Figure 6.10: Comparison of relative experimental uncertainties of the PDFs extracted from HERA I (outer) vs HERA I+II (inner) data sets under the same fit conditions to better assess the effect of the new high Q^2 measurements. The plots are taken from [11].

6.5.6 Cross check of different schemes

The comparison of the TR and ACOT schemes shows, that the ACOT scheme gives a better description of the low Q^2 data resulting in a smaller χ^2 value. The χ^2 value is smaller compared to the TR by about 30 units. This effect has been already observed in the F_L structure function measurement by the H1 collaboration [67]. It also has a visible impact on the systematic shifts of those data sets. The shifts of the cross sections are in the range of $0.5 - 1.5\sigma$, while in case of the TR the systematic shifts are about $1 - 2.9\sigma$. For of the high Q^2 data sets the ACOT scheme shows no systematic improvement compared to the TR-based results, and generally TR results have slightly better χ^2 value.

6.5.7 Comparison with global PDFs

In Figure 6.11 the H1PDF 2012 set is compared to the parton distribution sets MSTW08 [84], CT10 [83] and HERAPDF1.0 [87]. H1PDF 2012 parton distribution functions show a good agreement with the CT10 set of PDFs for low and medium values of x, within the uncertainties. Disagreement is found for the valence d quark at high values of x, where the uncertainty bands do not even overlap. CT10 fit prefers a less enhanced d_v, with a peak shifted towards higher x compared to the d_v obtained from H1PDF 2012. This is caused by the fixed target data used as an input to the CT10 fit, which constrains the region of high x values.

Contrary to CT10, the valence quark distributions of H1PDF 2012 and MSTW08 are quite different in the whole range of x. MSTW08 prefers a much steeper rise of the u_v at the medium values of x and drops much slower at the lower x region. The distribution of d_v in case of MSTW08 has a not very well understood shape, which seems to have some artificial origins.

One would expect to see a good agreement when comparing H1PDF 2012 and HERAPDF1.0. Indeed, H1PDF 2012 follows the approach developed for HERAPDF1.0 and both are using DIS data as an input. But the Figure 6.11a shows quite some disagreement, especially for the valence d. The reason is that an amount of more precise HERA II data used in the H1PDF 2012 allows to release some constraints and assumptions made for HERA-PDF1.0. For example, the at the low x values the d_v is no longer bounded to u_v and gluon has a more flexible parametrisation. Thus the H1PDF 2012

fit is much more flexible, and leads to noticeable differences when compared to the HERAPDF1.0.

The differences are enhanced at the starting, however with evolved PDFs at higher scales the differences are reduced due to the symmetric $q\bar{q}$ production. The treatment of different PDF assumptions is still an important ongoing issue and becomes a dominant source of uncertainty for precision measurements at the LHC.

6.5.8 Data and fit comparison

Double differential cross sections as function of x and Q^2 are compared to the predictions obtained from the H1PDF 2012 fit. In Figure 6.12 and Figure 6.13 the prediction obtained from H1PDF 2012 is compared to the measured reduced cross section of NC e^-p and CC e^+p respectively. The measurements and the data are in a very good agreement in the full kinematic range. The NC cross sections rise rapidly with decreasing x. It originates from the rise of the sea quark distribution, which dominates in the structure function F_2 at low x. As Q^2 increases the rise in the cross section becomes stronger. At high values of Q^2 the e^+p cross section for right handed polarised positron is higher than for the left handed one. The e^-p cross section for the left handed polarised electrons is higher than for the right handed one. The same kind of differences are observed in the CC cross section due to the difference in the lepton charge and the polarisation.

The single differential NC and CC cross sections are compared to the prediction from the H1PDF 2012 are shown in Figure 6.14 and Figure 6.15. The Standard Model expectations are given by the H1PDF 2012. The error bands originate from the total uncertainty on the PDFs as obtained by the QCD analysis. The cross sections are dropping by four orders of magnitude in the measured Q^2 range. At moderate Q^2 the CC cross section is suppressed by the $W^{\pm}$ propagator term $1/(Q^2 + M_W^2)$, compared to the NC cross section dominated by the contribution from the γ exchange. Both processes become compatible for the values of $Q^2 > M_{W/Z}^2$.

Many phenomena beyond the Standard Model are expected at high Q^2 values. The measured single differential cross section present a good sample that can be probed for deviations of the SM predictions. The chapter 7 presents a search for new physics effects using those measurements.

(a) Comparison to HERAPDF1.0 (b) Comparison to CT10
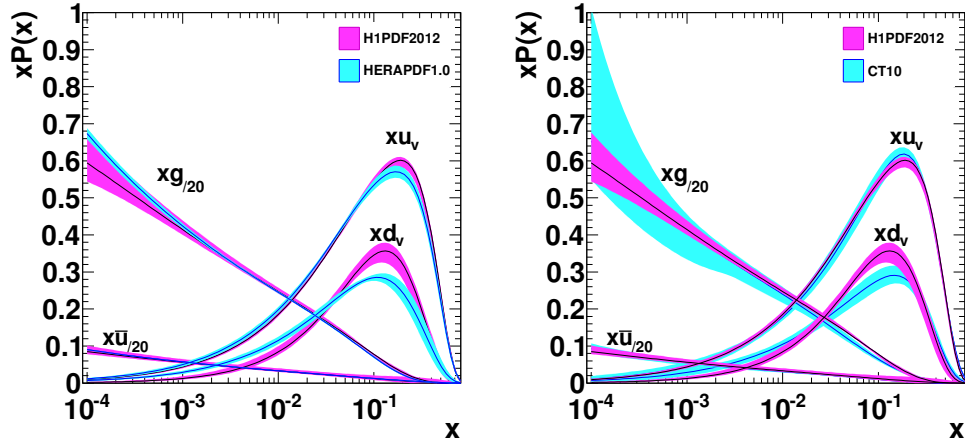
(c) Comparison to MSTW08
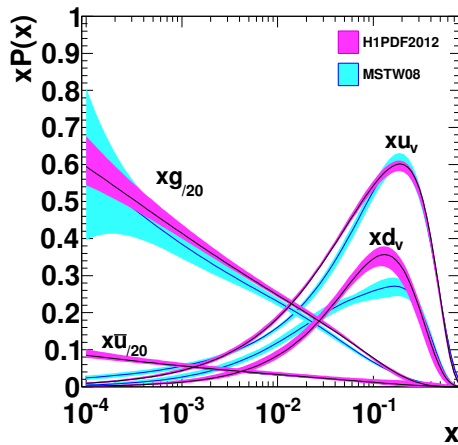
Figure 6.11: Comparison of parton distributions at $Q^2 = 10\,\text{GeV}^2$. The results of H1PDF 2012 fit are presented in magenta. The blue line and band correspond to the HERAPDF1.0 (a), CT10 (b) and MSTW2008 (c). The error bands indicate the total uncertainties on the PDFs.
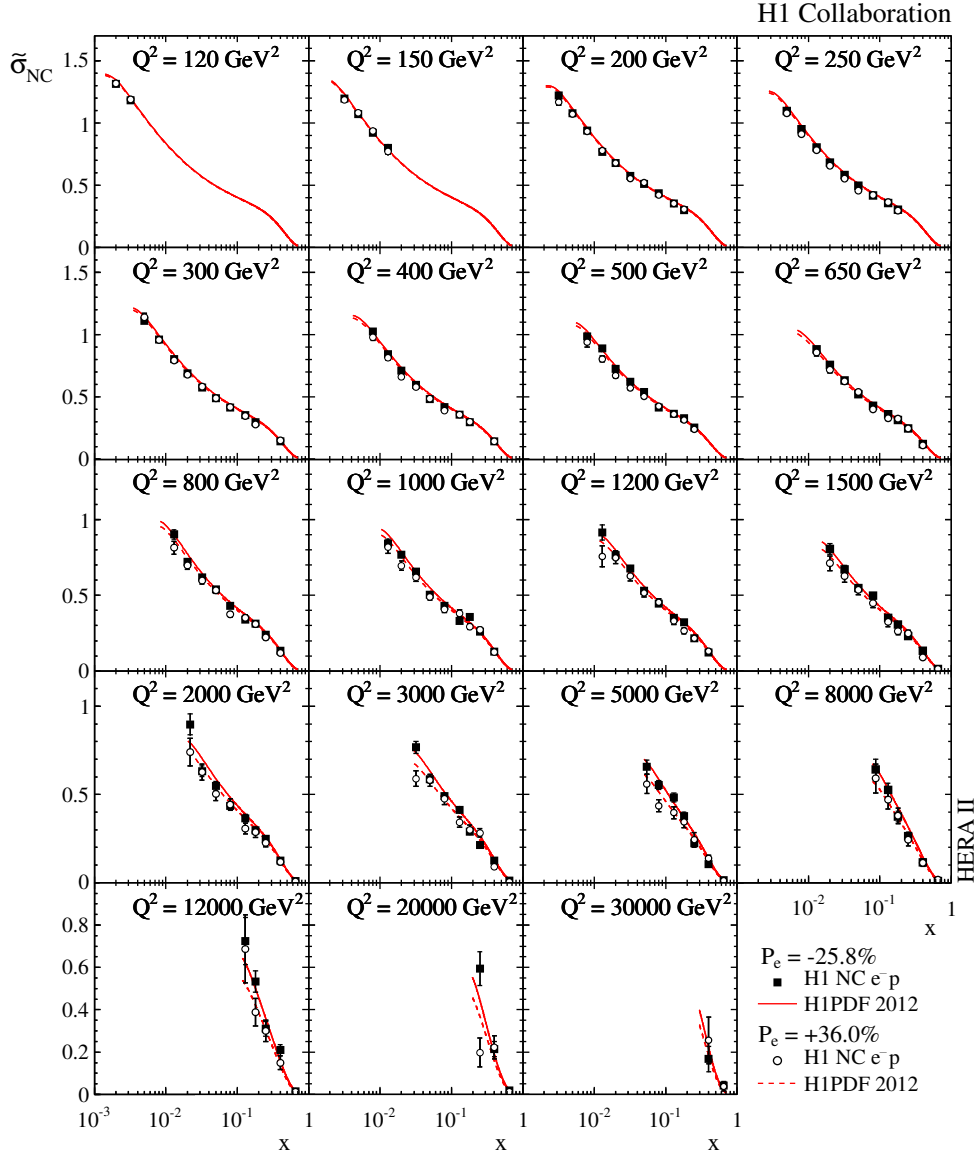
Figure 6.12: NC reduced cross sections $\tilde{\sigma}_{NC}$ for e^-p L (solid squares) and e^-p R (open circles) data sets shown for various fixed Q^2 values as a function of x. The inner and outer error bars represent the statistical and total errors, respectively. The luminosity and polarisation uncertainties are not included in the error bars. The curves show the corresponding expectations from H1PDF 2012. The plots are taken from [11].

103
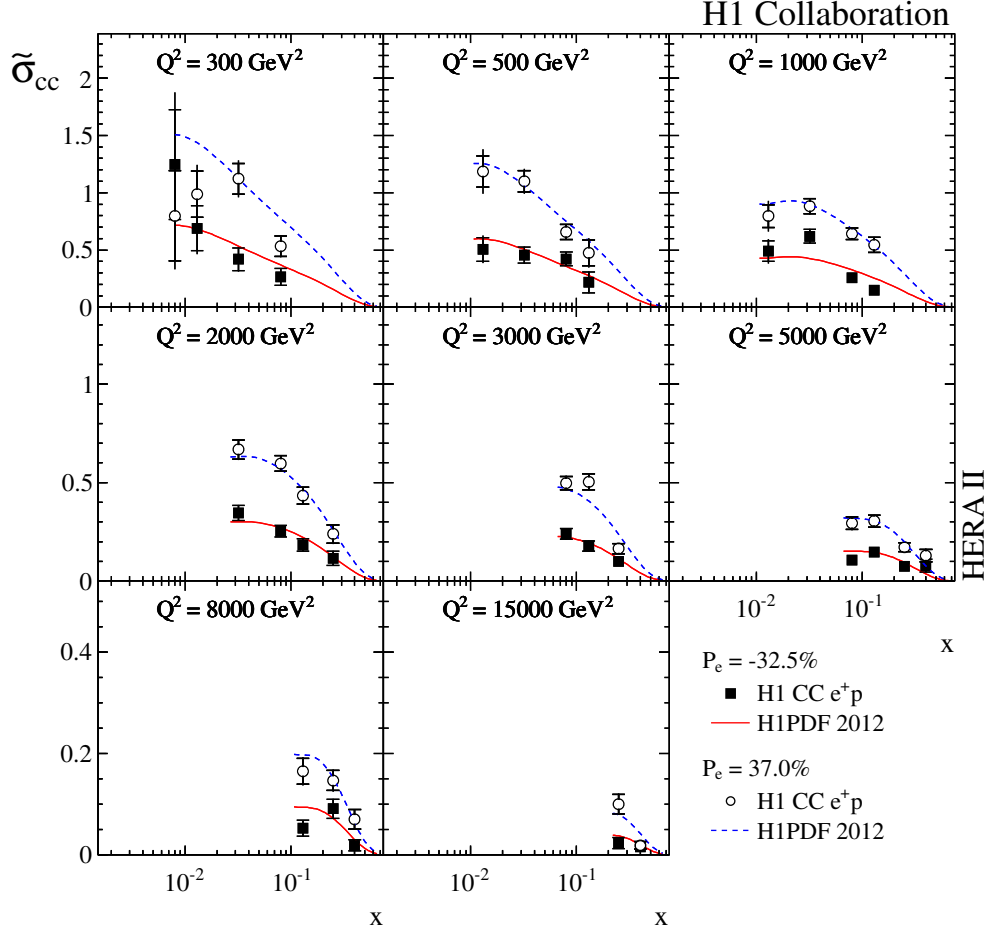
Figure 6.13: CC reduced cross sections $\tilde{\sigma}_{CC}$ for e^+p L (solid squares) and e^+p R (open circles) handed data sets shown for various fixed Q^2 values as a function of x. The inner and outer error bars represent the statistical and total errors, respectively. The luminosity and polarisation uncertainties are not included in the error bars. The curves show the corresponding expectations from H1PDF 2012. The plots are taken from [11].
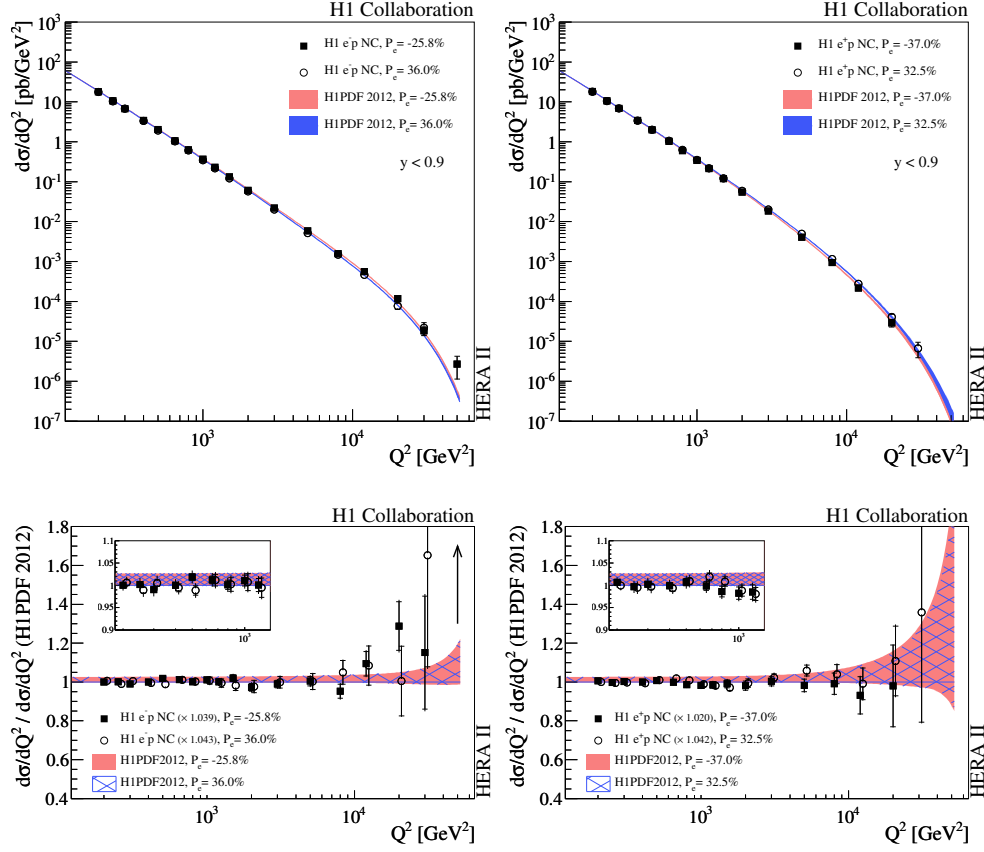
Figure 6.14: Q^2 dependence of the NC cross sections $d\sigma/dQ^2$ for the e^-p (top left) and e^+p (top right) L and R data sets. The ratios of the L and R cross sections to the corresponding Standard Model expectations are shown for the e^-p (bottom left) and e^+p (bottom right) data, where the normalisation shifts as determined from the QCD fit are applied to the data (see Table 6.7). The inner and outer error bars represent the statistical and total errors, respectively. The luminosity and polarisation uncertainties are not included in the error bars. The plots are taken from [11].
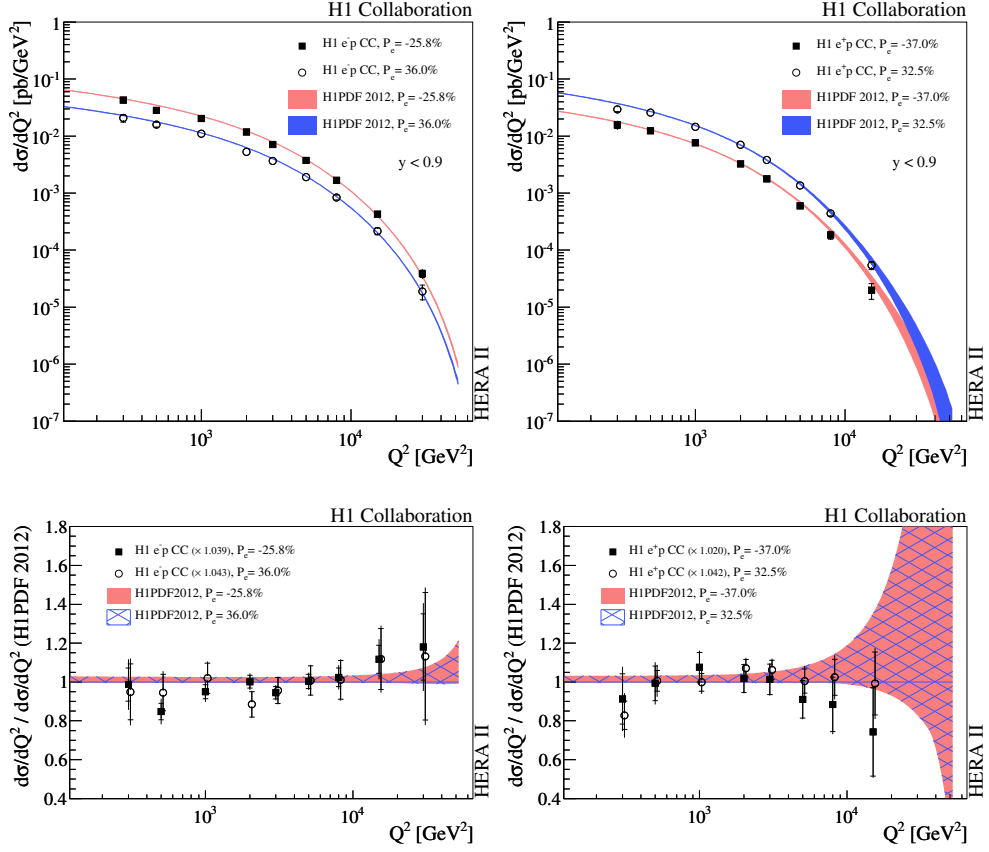
Figure 6.15: Q^2 dependence of the CC cross sections $d\sigma/dQ^2$ for the e^-p (top left) and e^+p (top right) L and R data sets. The ratios of the L and R cross sections to the corresponding Standard Model expectations are shown for the e^-p (bottom left) and e^+p (bottom right) data, where the normalisation shifts as determined from the QCD fit are applied to the data (see Table 6.7). The inner and outer error bars represent the statistical and total errors, respectively. The luminosity and polarisation uncertainties are not included in the error bars. The plots are taken from [11].

Beyond the SM analysis

7.1 Introduction

Before searching for new physics effects the consistency of the SM predictions, which is the basics for this search, and the data is checked. In the current analysis SM predictions are based on the CTEQ6m set of parton distribution functions [82].

The motivation of the PDF choice as well as the test of the SM is described in details in section 7.2. For cross checking purposes an alternative set of parton distribution functions was extracted and used in the full analysis chain. A description of this PDF set is given in section 7.2. The studies show that the results of the analysis based on both CTEQ6m and the alternative PDF are compatible.

Limits are derived for various CI scenarios and the constrains are set on the CI parameter η specific to each of the tested models. For this limit setting procedure the frequentist method is used, which is described in subsection 7.3.1. The results on the obtained limits are discussed in section 7.3.

7.2 The Standard Model test

The χ^2 function used in the presented contact interaction analysis is defined as in Equation 5.16.

The individual sources of the experimental uncertainties on the neutral current cross section measurement are discussed in chapter 4. Here a short summary of the statistical and systematic uncertainties relevant for the contact interaction analysis is presented.

The impact of the statistical uncertainty on the measured differential cross section varies from 1% for the values of transferred four-momenta less than $1200 \, \mathrm{GeV}^2$ up to 25% for the highest Q^2 values. The uncorrelated errors are about 2% in the region of $Q^2 < 5000 \, \mathrm{GeV}^2$ and rise up to 13% for the higher values of Q^2. The correlated systematic uncertainties have the following effect on the cross sections: the electromagnetic energy scale uncertainty varies from 0.3% for low Q^2 to 1.3% for the highest Q^2 bins, lepton polar angle uncertainty is in the range of $0.1 - 0.5\%$ and the error on luminosity measurement about $1.5 - 3.8\%$ depending on the data period. The uncertainties due to theoretical cross section predictions appear to be $1 - 8\%$ depending on value of the Q^2.

The correlated sources mainly affect the region with relatively small Q^2, while the region of high Q^2 is completely dominated by the statistical uncertainty and the total uncorrelated error. The dominant source of the correlated uncertainties is the error due to the theoretical cross sections predictions. They are estimated from the error sets provided by the CTEQ6m set of parton distribution functions.

7.2.1 PDF choice

As mentioned previously, the CTEQ6m set of parton distribution functions is used for the contact interaction analysis. What are the criteria that bring up this choice?

The motivation is based on several points. The parton distribution functions themselves are based on the information extracted from a variety of experimental measurements, like fixed target and collider experiments, and are evolving as new precise data is available and included in the extraction. One would expect that more precise and up to date measurements used in

the PDFs extraction, would originate in more precise theoretical predictions. On the other hand one would like to avoid potential biases, which may appear since the used PDFs are extracted with help of the same data that is actually being analysed for CI effects.

It is important to note that parton distribution functions in general are not precise, and consequently the theoretical cross section prediction has an uncertainty originating from the uncertainty on the PDFs used to derive it. The consistent way of taking those uncertainties into account, is to use the set of PDFs that provides not only the central values for parton distributions but also error sets, which can be used to estimate the uncertainty on the theoretical cross section predictions. The PDF set CTEQ6m is a good candidate to be used for theoretical predictions. The set contains not only the central PDFs but also a set of error parton distributions, which is later used to calculate the uncertainty on the predictions.

Another advantage of CTEQ6m set is that only a small amount of high Q^2 HERA data was used as an input to derive it. CTEQ6m includes HERA I $e^{\pm}p$ scattering data at high Q^2 from the H1 ($L = 52\,\mathrm{pb}^{-1}$) and ZEUS ($L = 30\,\mathrm{pb}^{-1}$) experiments, while the $e^+p(e^-p)$ data sets analysed here are 6(10) times larger. Therefore the correlations between the analysed data and the CTEQ6m PDF set are small and are neglected.

Nevertheless, in order to cross check the results achieved using CTEQ6m an alternative set of parton distributions is extracted within this thesis. The main idea is to have a set of PDFs completely independent from the analysed data i.e. a set that does not contain any H1 NC measurement at high values of Q^2. To obtain a PDF set a next-to-leading order QCD fit to the following data is performed:

- H1 neutral current data excluding the measurements for the values of $Q^2 > 200\,\mathrm{GeV}^2$,

- full H1 charged current data set,

- data from the fixed target BCDMS experiment [10].

In case of HERA data, high values of Q^2 imply also high values of x. In other words, excluding high Q^2 values implies also exclusion of high x values. However the fixed target BCDMS measurements are covering the high x region. The fixed target measurements from the BCDMS experiment are used in order to compensate the missing information from the unused H1

high Q^2 neutral current measurements, by including its data into the PDF fit.

The extraction of this PDF set is identical to the procedure for the H1PDF 2012 set of parton distribution functions as described in details in chapter 6. The results of the cross check are discussed later in this section.

7.2.2 Comparison of the data with the SM prediction

After choosing a PDF set one can test the compatibility of the prediction and the available data. The single differential NC cross section $d\sigma/dQ^2$ is compared to the Standard Model predictions using the χ^2 method. The analysed data is the H1 NC single differential cross section as a function of Q^2. Table 7.1 summarizes the data sets with corresponding luminosity and polarisation.

Reaction	$\mathcal{L}_{int}$ [pb^{-1}]	$\sqrt{s}$ [GeV]	Polarisation (P_e [%])	
$e^+p \to e^+X$	36	301	Unpolarised	
$e^-p \to e^-X$	16	319	Unpolarised	
$e^+p \to e^+X$	65	319	Unpolarised	
$e^-p \to e^-X$	46	319	Right	($P_e = +37$)
$e^-p \to e^-X$	103	319	Left	($P_e = -26$)
$e^+p \to e^+X$	98	319	Right	($P_e = +33$)
$e^+p \to e^+X$	82	319	Left	($P_e = -38$)

Table 7.1: Data samples recorded in the years 1994-2007 with corresponding integrated luminosities, centre-of-mass energies and average longitudinal polarisations [109].

The comparison of the data to the predictions obtained from PDF set CTEQ6m is presented in Figure 7.1. The measured single differential NC cross section to the SM prediction ratio given by CTEQ6m PDF as a function of Q^2 is shown. The top figure shows the comparison of the SM predictions and combined HERA I+II data with an average longitudinal polarisation of $P = 0$. The other two plots show the H1 NC cross section measurements from the HERA II running period for different lepton charges
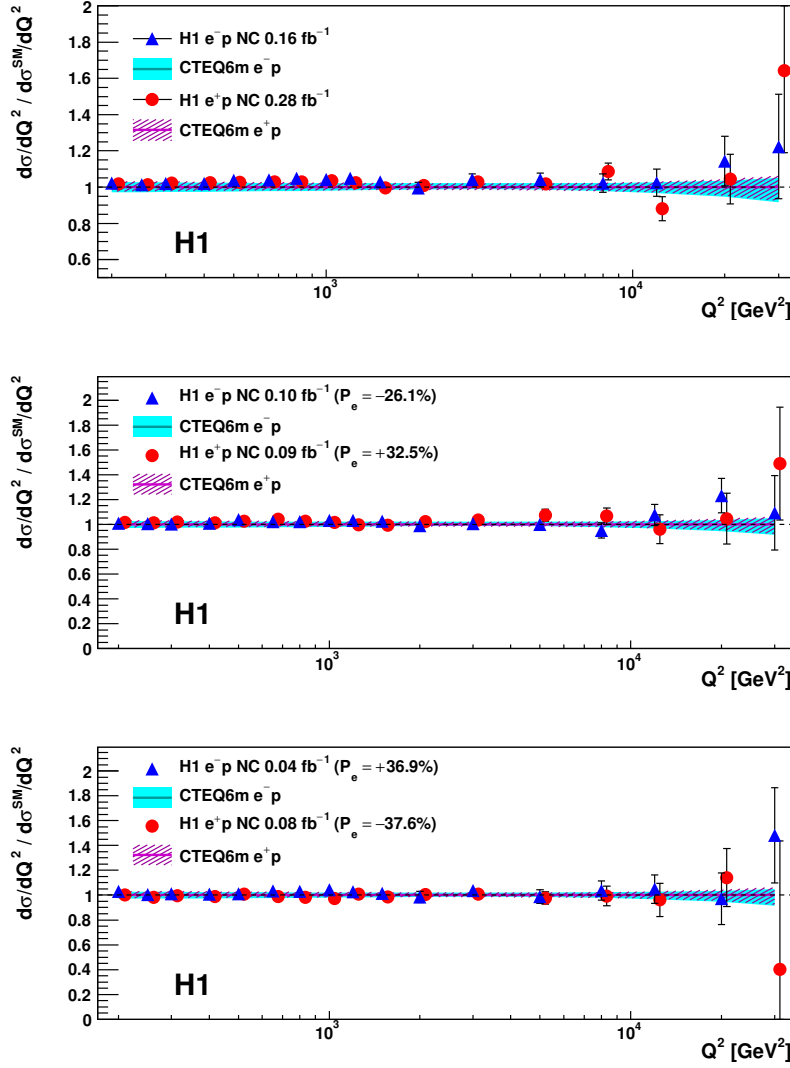
Figure 7.1: The ratio of the measured single differential NC cross section to the SM prediction determined using the CTEQ6m PDF set. The top figure corresponds to the full H1 data with an average longitudinal polarisation of $P \approx 0$. The middle and bottom figures represent polarised H1 data taken from the year 2003 onwards. The blue triangles correspond to the e^-p and the red dots to the e^+p processes. The error bars represent the statistical and uncorrelated systematic errors added in quadrature. The bands indicate the PDF uncertainties of the SM predictions. The plots are taken from [109]

and polarisations. The data agree well with the predictions from CTEQ6m PDF set in the full kinematic range of the measurements.

The consistency of the prediction given by the CTEQ6m set of PDFs and the NC single differential cross section measurements is checked by a χ^2 fit. The χ^2/n_{dof} value for the combined e^+p data is 16.4/17 and for the combined e^-p data is 7/17.

The comparison data versus the alternative PDF set prediction is shown in the Figure 7.2. The predictions from the extracted PDF set are compared to the H1 NC single differential cross sections as a function of Q^2. The results of the comparison of the theoretical prediction and the $d\sigma/dQ^2$ NC cross section measurements are: for the combined e^+p data $\chi^2/n_{dof} = 13.4/17$ and for the combined e^-p data $\chi^2/n_{dof} = 9/17$. Those are comparable with the results obtained using the set of CTEQ6m parton distribution functions. Both the prediction and the data are normalised to the predictions based on CTEQ6m set. The prediction from the alternative PDF set has a systematically larger prediction for the cross section. The difference is larger at relatively low and medium values of Q^2. As the Q^2 gets larger the discrepancy with the CTEQ6m predictions becomes less. The CTEQ6m seems to describe the normalisation of the data better than the alternative PDF set. The normalisation shift obtained from fit for e^+p data set is 3.2% and for the e^-p is 4.1%.

The dedicated fit shows a good description of the data. The normalisation shifts are estimated from the fit to be 5.1% for the e^+p data and 4.3% for the e^-p data. In Figure 7.2 the lower plot presents the data points shifted by the normalisation factors obtained from the fit.

7.3 Limits on new physics

The good description of the data by the SM expectations considerably decreases the parameter space, where new physics might appear. The lack of evidence of novel effects, motivate to determine the exclusion limits for the individual SM extensions. The compatibility of the data within the different SM+CI scenarios is tested by determining limits on the CI parameter η of each model.

To derive limits the method of least squares can be used. Limits of a model parameter are derived by varying the parameter until the value of
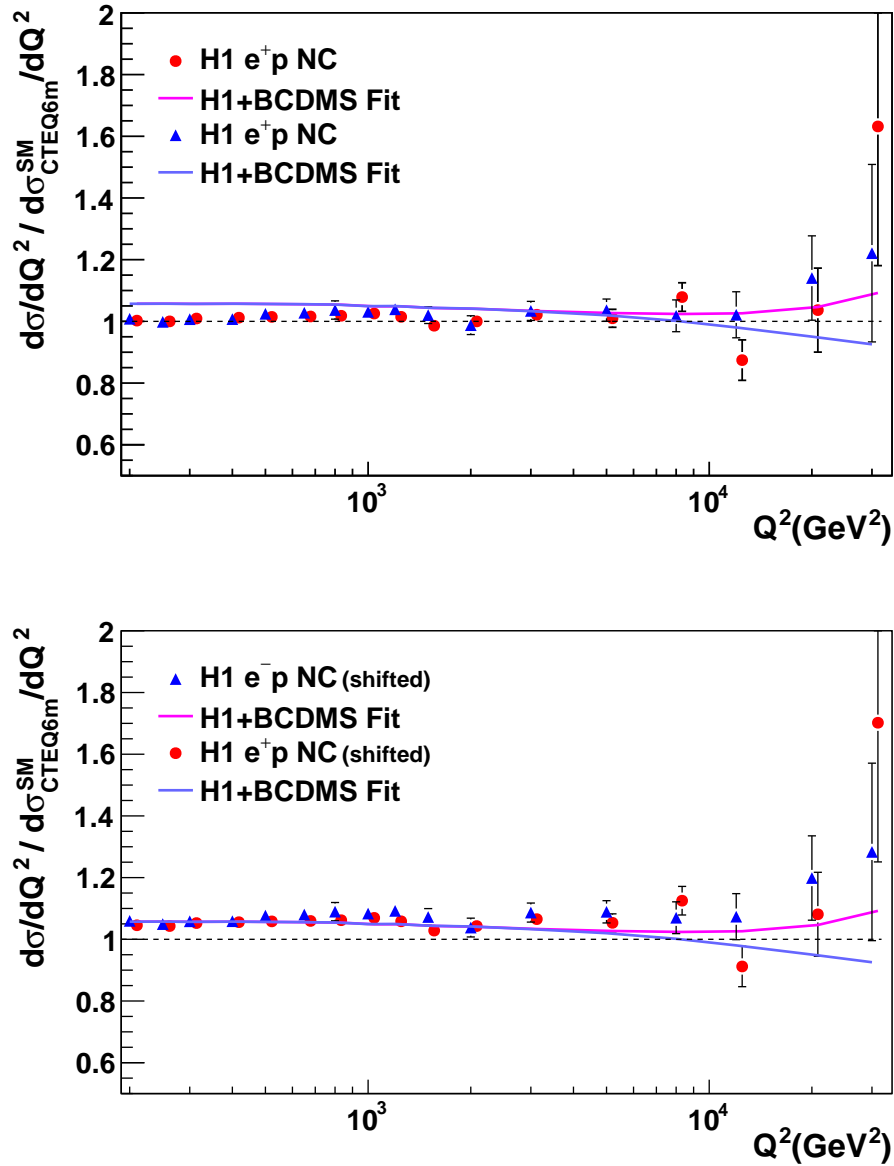
Figure 7.2: The measured cross sections compared to the prediction from the extracted PDFs. The blue triangles correspond to the e^-p and the red dots correspond to the e^+p processes. In the lower plot the data points are shifted by the normalisation factors obtained from the fit, corresponding to 1.053 for e^+p and 1.043 for e^-p data.

the χ^2 changes by a certain amount with respect to the χ^2 obtained in the Standard Model fit. The condition for a 95% confidence level (CL) limit is $\chi^2 - \chi^2_{SM} = 3.84$ [4]. However, this method will not give a meaningful results in case of secondary minima or other structures in the shapes of the χ^2 curves than the expected quadratic behaviour. The Figure 7.3 illustrates
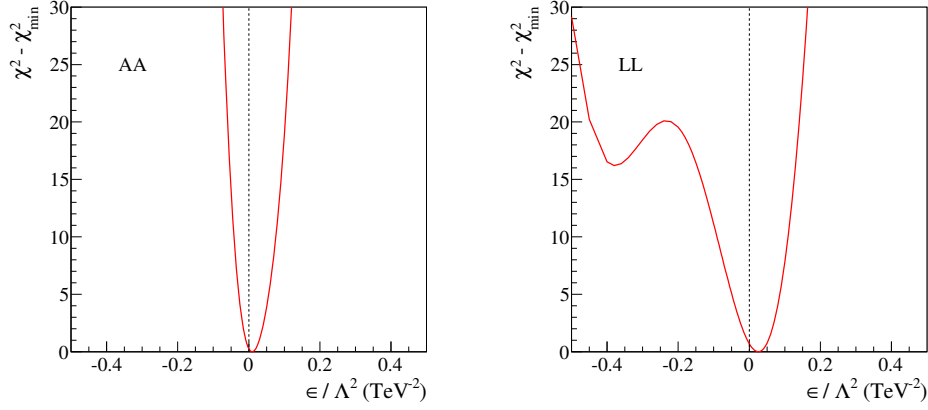
Figure 7.3: $\chi^2 - \chi^2_{min}$ as a function of ϵ/Λ^2 from fits to LL and AA compositeness models. For model AA the curve is parabolic, while in case of model LL the curve has more than one minima. In both cases the minimal value for the χ^2 differs from the Standard Model prediction ($\eta^{SM} = 0$. The definition of the models is given in Table 2.1.

the presence of a local secondary minima in the distribution of $\chi^2 - \chi^2_{min}$ as function of ϵ/Λ^2 for a specific compositeness model, where $\eta \sim \epsilon/\Lambda^2$. The presence of secondary minima makes the limit estimation using the method of least squares ambiguous .

In order to avoid these complications an alternative method is used to derive limits on the CI model parameters η, the frequentist approach [110]. The frequentist approach is more robust than the χ^2 approach to obtain parameters limits, in the case of a complicated χ^2 behaviour. The approach is described in more details in the next subsection.

7.3.1 Frequentist approach

The frequentist approach is based on toy Monte Carlo (MC) experiments. This approach is used to set limits on the contact interaction parameter η, which is specific to each of the CI scenarios. This parameter is related to a scale Λ in case of compositeness models, the leptoquark mass M_{LQ} or the gravitational scale M_s. The limit estimating procedure is described for a specific CI model with parameter η and is applied in the same way to all of the scenarios considered in the presented analysis.
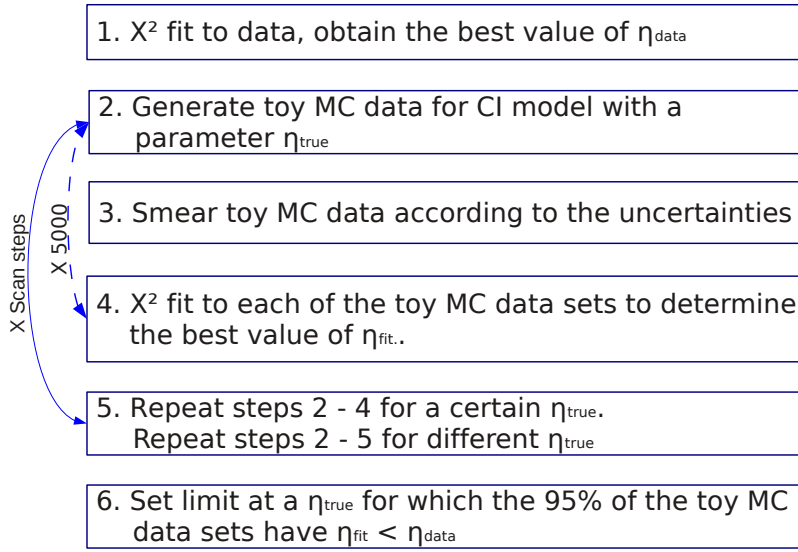
Figure 7.4: A schematic illustration of the frequentist method.

The procedure is shown schematically in Figure 7.4 and described in the following. The procedure starts with a χ^2 fit to data, where the CI parameter η is a free parameter. As a result a value η_{data} is obtained.

The second step is to construct a number toy MC data sets by calculating the predicted cross section in each Q^2 bin for a given value of η^{true},

$$\sigma_{prediction} = \sigma_{SM} + \sigma_{CI}(\eta). \tag{7.1}$$

The such obtained toy MC data are then smeared according to the statistical error given by the predicted number of events and according to the uncorrelated and correlated systematic uncertainties, assuming Gaussian

behaviour of the errors. A fit to each of the constructed toy MC data sets is performed and the best value η_i^{fit} is obtained. The index i here indicates the number of the ith toy MC data set. In the current analysis the number of produced toy MC data sets is 5000, which ensures stability of the obtained results. A larger number of toy MC data sets do not give any improvement.

The next step is to vary the η^{true} and to repeat the procedure described in the second step. The steps in η are not uniform, but are rather small in the region, where the results are expected and larger in the rest of the scan region. The scanned region and the size of the steps vary for different models.

The results are recorded to histograms as shown in Figure 7.5. Each of the four plots shown correspond to a different η^{true} value. The results of the fits to toy MC data sets are distributed around the corresponding η^{true}. The distribution is not always perfectly Gaussian, since the number of toy data sets is limited and some statistical fluctuations are possible.

Finally, an upper limit for the parameter η at the 95% CL is determined as the value η^{true}, for which only 5% of the toy experiments have a fitted value η_i^{fit} smaller than the η^{data} value obtained from the fit to the real data. The shaded area of the histogram in the last plot in Figure 7.5 illustrates the 5% of the toy experiments, for which $\eta_i^{fit} < \eta^{data}$.

The upper limits on the parameter η are then transformed to lower limits on the compositeness scale Λ or

In the following, the limits on various CI model parameters obtained from the H1 NC cross sections analysis are presented.

7.3.2 Limits on compositeness scale

As was described in chapter 2 the substructure of fermions or their composition can be described using the contact interaction formalism Equation 2.44. The limits are determined for the compositeness scale Λ that enters the cross section calculation via the chiral structure parameter $\eta = \epsilon g^2/\Lambda^2$. The coupling strength g is assumed to be $g^2 = 4\pi$. The parameter $\epsilon = \pm 1$ represents the sign of the interference between the investigated compositeness model and the Standard Model. For each particular chiral model both interference scenarios are treated separately.
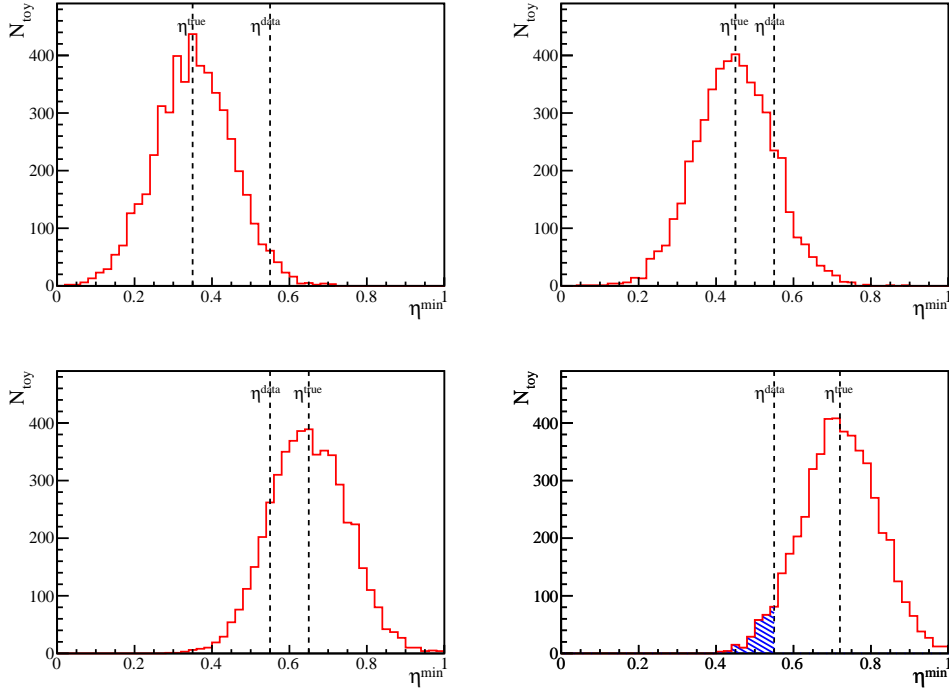
Figure 7.5: An example distribution of the Monte Carlo toy experiments as a function of the η^{fit} is shown. Each of the plots corresponds to a different value of η^{true}. The value of the CI parameter obtained from the fit to data is indicated as η^{data}. The shaded area in the lower right plot indicates the 5% of MC toy experiments with $\eta^{fit} < \eta^{data}$.

The results of the analysis of various compositeness models are summarised in Table 7.2 and shown Figure 7.6. The lower limits at the 95% CL on the compositeness scale parameter Λ are derived for different interference signs $+$ and $-$ separately. Depending on the chiral structure and the interference sign the limits vary in the range of $3.6 - 7.2$ TeV. The $LL + RR$, $LR + RL$ and VV models to have the strongest limits because the chiral couplings enter the Lagrangian with the same sign. In some cases, as the VA model, the combination of the parameters results in a cancellation of the pure contact interaction contributions and the Standard Model interference terms. In those cases the obtained limits are weaker.

H1 Search for General Compositeness

$$\eta_{ab}^q = \epsilon_{ab}^q \, 4\pi/\Lambda^2$$

Model	$[\; \epsilon_{LL}, \; \epsilon_{LR}, \; \epsilon_{RL}, \; \epsilon_{RR}]$	Λ^+ [TeV]	Λ^- [TeV]
LL	$[\; \pm 1, \quad 0, \quad 0, \quad 0]$	4.2	4.0
LR	$[\quad 0, \; \pm 1, \quad 0, \quad 0]$	4.8	3.7
RL	$[\quad 0, \quad 0, \; \pm 1, \quad 0]$	4.8	3.8
RR	$[\quad 0, \quad 0, \quad 0, \; \pm 1]$	4.4	3.9
VV	$[\; \pm 1, \; \pm 1, \; \pm 1, \; \pm 1]$	5.6	7.2
AA	$[\; \pm 1, \; \mp 1, \; \mp 1, \; \pm 1]$	4.4	5.1
VA	$[\; \pm 1, \; \mp 1, \; \pm 1, \; \mp 1]$	3.8	3.6
$LL + RR$	$[\; \pm 1, \quad 0, \quad 0, \; \pm 1]$	5.3	5.1
$LR + RL$	$[\quad 0, \; \pm 1, \; \pm 1, \quad 0]$	5.4	4.8

Table 7.2: Lower limits at 95% CL on the compositeness scale Λ for various models. The Λ^+ limits correspond to the upper signs and the Λ^- limits correspond to the lower signs of the chiral coefficients $[\epsilon_{LL}^q, \, \epsilon_{LR}^q, \, \epsilon_{RL}^q, \, \epsilon_{RR}^q]$.
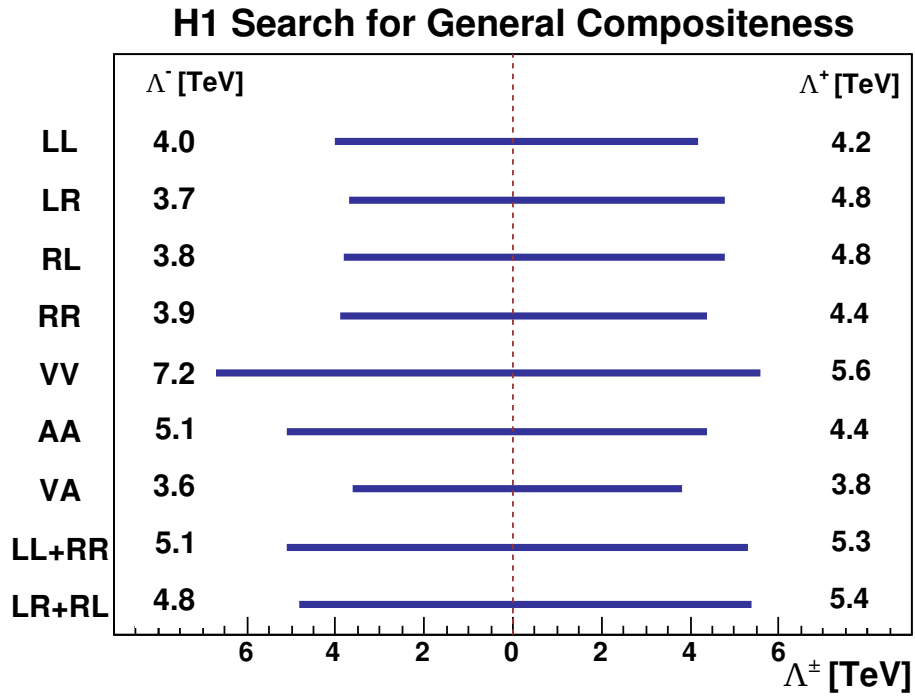
Figure 7.6: Lower limits on the compositeness scale Λ for various chiral models. Both signs of the chiral coefficients Λ^+ and Λ^- are represented. The plot is taken from [109]

7.3.3 Limits on leptoquark masses

Leptoquarks with masses much larger than the available centre of mass energy can be treated similar to the compositeness models. In this case the coupling strength g and the compositeness scale Λ replace the Yukawa coupling λ and the leptoquark mass M_{LQ}. The investigated leptoquarks are considered within the Buchmüller-Rückl-Wyler (BRW) [37] framework as discussed in chapter 2.

Since leptoquarks have a chiral structure, additional sensitivity on the corresponding limits is achieved, due to the data where the lepton beam has a certain polarisation.

Lower limits at 95% CL on the ratio of the leptoquark mass to the Yukawa coupling are summarised in the Table 7.3. The presented results correspond to Yukawa couplings set to unity, $\lambda = 1$. The wide spread of the limits can be explained by the proton structure. The proton at high x predominantly consists of two u and one d quarks, so leptoquarks that couple to u quarks gain more sensitivity compared to those coupling to d quarks, which provides better limits.

The results of this CI analysis for leptoquarks are also comparable to a direct search for leptoquarks performed by the H1 collaboration [111]. The direct search of leptoquarks is based on DIS NC and CC events. The leptoquark mass M_{LQ} spectrum of the events is compared to the SM predictions in search for deviations and the results are interpreted in terms of exclusion limits. An example comparing limits for two scalar types of leptoquarks by the different analyses is shown in the Figure 7.7. The results are in a good agreement for the leptoquarks that are sensitive to the neutral current data only (left plot). Since the direct search is also using charged current data the sensitive to charged current limits are more stringent compared to the contact interaction analysis, which is using only neutral current data.

7.3.4 Limits on gravitational scale

The possible influence of large extra dimensions (LED) on the cross section $d\sigma/dQ^2$ is characterized by the coupling coefficient $\eta = \lambda/4M_s$. The coupling λ depends on the theory and is expected to be of the order of unity. In analogy with the general compositeness models the behaviour of the interference with the SM is left open, by convention λ is set to ± 1.

H1 Search for Heavy Leptoquarks

$$\eta^q_{ab} = \epsilon^q_{ab}\,\lambda^2/M^2_{\mathrm{LQ}}$$

LQ	ϵ^u_{ab}	ϵ^d_{ab}	F	M_{LQ}/λ [TeV]
S^L_0	$\epsilon^u_{LL}=+\frac{1}{2}$		2	1.10
S^R_0	$\epsilon^u_{RR}=+\frac{1}{2}$		2	1.10
$\tilde{S}^R_0$		$\epsilon^d_{RR}=+\frac{1}{2}$	2	0.41
$S^L_{1/2}$	$\epsilon^u_{LR}=-\frac{1}{2}$		0	0.87
$S^R_{1/2}$	$\epsilon^u_{RL}=-\frac{1}{2}$	$\epsilon^d_{RL}=-\frac{1}{2}$	0	0.59
$\tilde{S}^L_{1/2}$		$\epsilon^d_{LR}=-\frac{1}{2}$	0	0.66
S^L_1	$\epsilon^u_{LL}=+\frac{1}{2}$	$\epsilon^d_{LL}=+1$	2	0.71
V^L_0		$\epsilon^d_{LL}=-1$	0	1.06
V^R_0		$\epsilon^d_{RR}=-1$	0	0.91
$\tilde{V}^R_0$	$\epsilon^u_{RR}=-1$		0	1.35
$V^L_{1/2}$		$\epsilon^d_{LR}=+1$	2	0.51
$V^R_{1/2}$	$\epsilon^u_{RL}=+1$	$\epsilon^d_{RL}=+1$	2	1.44
$\tilde{V}^L_{1/2}$	$\epsilon^u_{LR}=+1$		2	1.58
V^L_1	$\epsilon^u_{LL}=-2$	$\epsilon^d_{LL}=-1$	0	1.86

Table 7.3: Lower limits at 95% CL on M_{LQ}/λ for scalar (S) and vector (V) leptoquarks, where L and R denote the lepton chirality and the subscript (0, 1/2, 1) is the weak isospin. For each leptoquark type, the relevant coefficients ϵ^q_{ab} and fermion number $F = L + 3B$ are indicated. Leptoquarks with identical quantum numbers except for weak hypercharge are distinguished using a tilde, for example V^R_0 and $\tilde{V}^R_0$. Quantum numbers and helicities refer to $e^- q$ and $e^- \bar{q}$ states.
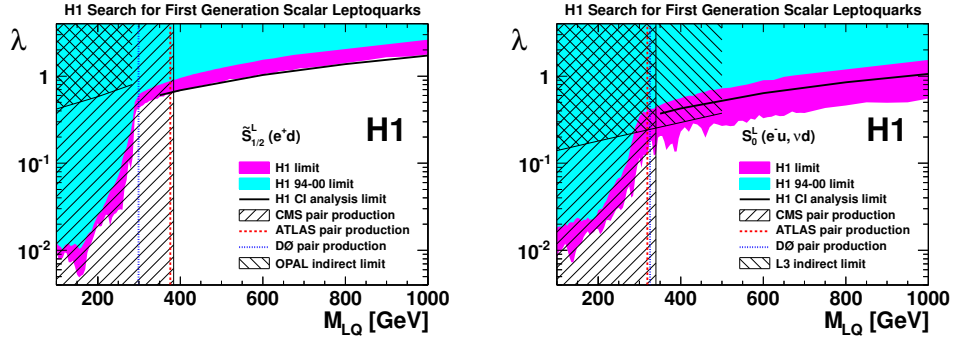
Figure 7.7: Exclusion limits on the coupling λ as a function of the leptoquark mass for scalar leptoquarks in the framework of the BRW model [37] from the direct search for leptoquarks by the H1 [111]. The parentheses after the LQ name indicate the fermion pairs coupling to the LQ, where pairs involving anti-quarks are not shown. The domains above the curves are excluded at the 95% CL. Constraints on LQs with masses above 350 GeV from the current CI analysis are indicated by the solid line. The results of both analyses are in a good agreement for the LQs, which are probed in NC data. The limits obtained from the direct search are more stringent for those LQs which are probed in CC data, since the CI analysis is based on the NC data only. Limits from LEP (OPAL and L3), the Tevatron (D0) and the LHC (CMS and ATLAS, $\sqrt{s} = 7$ TeV data) are shown for comparison [112–118]. The plots are taken from [111]

The obtained limits on the gravitational scale M_S are presented in Table 7.4, negative (M_s^-) and positive (M_s^+) signs of the coupling λ are taken into account separately. For both cases of the interference sign the results are similar.

7.3.5 Limits on quark radius

The effect of the finite size of the quark represented by the root mean squared radius of the electroweak charge distribution on the cross section is described in the chapter 2. An upper limit on the quark electroweak charge

H1 Search for Large Extra Dimensions

$$\eta_G = \lambda/M_S^4$$

coupling λ	M_S [TeV]
+1	0.90
−1	0.92

Table 7.4: Lower limits at the 95% CL on a model with large extra dimensions on the gravitational scale M_S in $4+n$ dimensions, assuming positive ($\lambda = +1$) or negative ($\lambda = -1$) couplings.

distribution radius is determined to be:

$$R_q < 0.65 \cdot 10^{-18}\,\text{m}.$$

7.4 Conclusions

The full amount of neutral current data collected by the H1 experiment are analysed in search for contact interaction effects at the scales beyond the HERA center of mass energy. The good agreement between the measurements and the Standard Model predictions allows to set constrains on various models, whereas the limits are set using the frequentist method. The results of the presented analysis supersede the previous limits by the H1 [110] and ZEUS [119] experiments.

The latest LHC results achieved for scalar leptoquark masses [120, 121], chiral coupling η_{LL} [122–125] and extra dimensions [126] competed out the limits set by the presented analysis. However, for the models where LHC experiments have no up to date results, the presented limits are competitive and in some cases the best compared to those obtained by the LEP [127] or the Tevatron [114, 115, 128, 129].
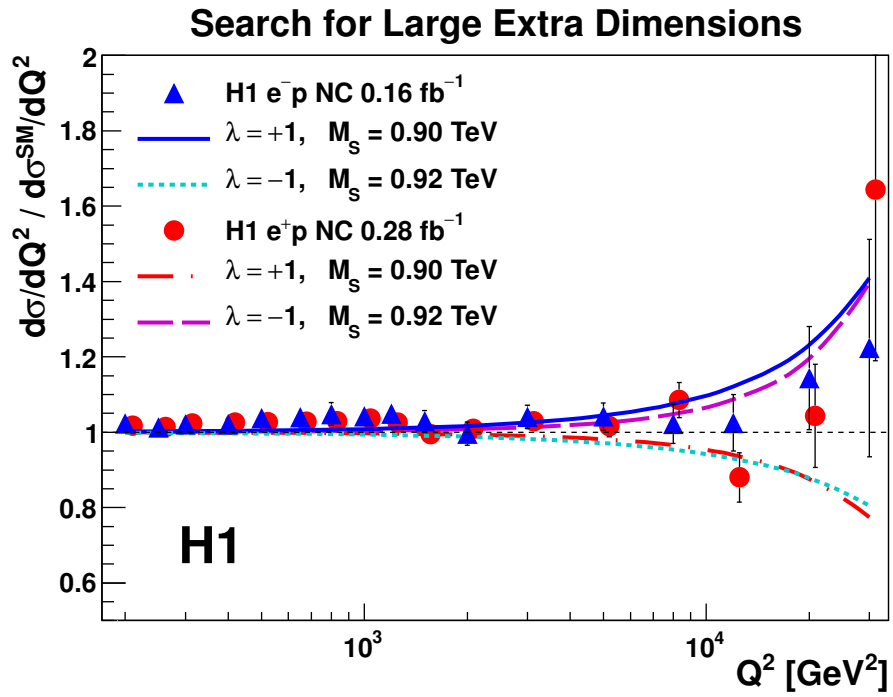
Figure 7.8: The measured neutral current cross section normalised to the SM prediction. The H1 $e^{\pm}p$ data are compared to 95% CL exclusion limits from the full H1 data on the gravitational scale M_S. The plot is taken from [109].

Chapter

8

Summary

In this thesis the QCD analysis of inclusive neutral and charged current deep inelastic $e^{\pm}p$ scattering cross sections and a search for deviations from the Standard Model predictions in neutral current cross section are presented. Both analyses are based on data taken in the years 1994 - 2007, which corresponds to a total integrated luminosity of about $0.5\,\mathrm{fb}^{-1}$. The data cover a large kinematic phase space with $0.5\,\mathrm{GeV}^2 \leq Q^2 \leq 30000\,\mathrm{GeV}^2$ and $3 \cdot 10^{-5} \leq x \leq 0.65$, allowing for a test of QCD, as well as a search for effects of new physics.

The QCD analysis of the data results in a set of parton distribution functions named as H1PDF 2012, which is the final result of the PDF determination based on the H1 inclusive data only. The results of this analysis provide better constraints on the partonic structure of the proton compared to previous H1 PDF sets. A significant improvement is achieved for the flavour separation in the region of high x. The results of the analysis can be used in a future QCD fit of the combined inclusive data from the H1 and ZEUS, to reach even better measurements of the proton structure. These results are an important input for ongoing or future analyses at the Large Hadron Collider (LHC).

Chapter 8 Summary

The NC single differential cross sections are investigated to search for signs of new physics in the framework of contact interactions. The data show a good agreement with the SM predictions, which allows to interpret the results in terms of exclusion limits for various contact interaction scenarios.

- For different compositeness scenarios lower limits on the characteristic scale Λ vary in the range of $3.6 - 7.2\,\mathrm{TeV}$.

- Lower limits on the leptoquarks masses, assuming the Yukawa coupling to be unity, depending on the particular leptoquark type are set between $0.41\,\mathrm{TeV}$ and $1.86\,\mathrm{TeV}$.

- In a model with large extra dimensions a lower limit on the gravitational scale is obtained $M_S > 0.91\,\mathrm{TeV}$.

- Finally, an upper limit on the quark radius is set of $R_q < 0.65 \cdot 10^{-18}\,\mathrm{m}$ using a from factor approach.

The results are exploiting the sensitivity to new physics of the full H1 data and are comparable and partly complementary to those obtained at LEP or the Tevatron.

Appendix

A

Correlation of the PDF parameters

The correlations between PDF parameters of the H1PDF 2012 fit, as obtained by the MINUIT package, are presented in Table A.1.

The global correlation ρ_k, as defined in [130], is the largest value of $\rho(X_k, Y)$. This quantity is a measure of the total amount of correlation between variable X_k and all the other variables. If $\rho_k = 0$, the variable X_k is uncorrelated with all others. If $\rho_k = 1$, X_k is completely correlated with at least one linear combination of the other variables.

The global correlation coefficient can be found from the diagonal elements V_{kk} of the covariance matrix, and the diagonal elements $(V^{-1})_{kk}$ of its inverse,

$$\rho_k = \sqrt{1 - [V_{kk} \cdot (V^{-1})_{kk}]^{-1}}. \tag{A.1}$$

Param	Global	B_g	C_g	A'_g	B'_g	B_{u_v}	C_{u_v}	E_{u_v}	B_{d_v}	C_{d_v}	$C_{\bar{U}}$	$A_{\bar{D}}$	$B_{\bar{D}}$	$C'_{\bar{D}}$
B_g	0.99	1.00	0.51	-0.66	0.12	0.10	0.01	-0.04	0.10	0.07	0.01	-0.04	-0.07	0.06
C_g	0.98	0.51	1.00	0.08	0.34	0.25	-0.04	-0.19	-0.01	-0.08	-0.02	-0.19	-0.22	-0.46
A'_g	0.99	-0.60	0.08	1.00	0.63	0.11	-0.01	-0.09	0.03	0.02	-0.03	-0.10	-0.12	-0.06
B'_g	0.98	0.12	0.34	0.63	1.00	0.10	0.01	-0.03	0.12	0.07	0.04	0.06	0.07	0.06
B_{u_v}	0.98	0.10	0.25	0.11	0.10	1.00	-0.16	-0.71	-0.01	-0.19	0.55	0.22	0.13	0.09
C_{u_v}	0.94	0.00	-0.04	-0.01	0.01	-0.16	1.00	0.69	-0.26	-0.18	-0.13	-0.08	-0.07	-0.06
E_{u_v}	0.97	-0.04	-0.18	-0.08	-0.03	-0.70	0.69	1.00	-0.12	0.06	-0.22	-0.04	-0.01	-0.15
B_{d_v}	0.97	0.10	-0.01	0.03	0.13	-0.01	-0.26	-0.12	1.00	0.83	0.14	0.16	0.11	0.39
C_{d_v}	0.96	0.07	-0.08	0.02	0.07	-0.19	-0.18	0.07	0.83	1.00	-0.13	-0.04	-0.05	0.31
$C_{\bar{U}}$	0.97	0.01	-0.02	-0.03	0.04	0.55	-0.13	-0.22	0.14	-0.13	1.00	0.55	0.49	-0.15
$A_{\bar{D}}$	0.94	-0.04	-0.19	-0.11	0.06	0.22	-0.08	-0.04	0.16	-0.04	0.55	1.00	0.93	0.20
$B_{\bar{D}}$	0.96	-0.07	-0.22	-0.12	0.07	0.13	-0.07	-0.01	0.11	-0.05	0.49	0.93	1.00	0.16
$C'_{\bar{D}}$	0.96	0.06	-0.46	-0.06	0.06	0.09	-0.06	-0.16	0.39	0.31	-0.15	0.20	0.16	1.00

Table A.1: The correlation factors between the PDF parameters obtained from the fit are presented. The totally correlated case is indicated by coefficient value of 1, unticorrelated case corresponds to -1 and not correlated is 0. The global correlation coefficients represent the level of correlation between a particular parameter and the rest of the parameters.

Bibliography

[1] H1 Collaboration, I. Abt *et al.*, "The H1 detector at HERA", *Nucl.Instrum.Meth.* **A386** (1997) 310–347.

[2] ZEUS Collaboration, "The ZEUS Detector". Status report (unpublished), 1993. http://www-zeus.desy.de/bluebook/bluebook.html.

[3] F. Halzen and A. Martin, *Quarks & Leptons: An introductory course in modern particle physics.* John Wiley & Sons, New York, USA, 1984.

[4] Particle Data Group Collaboration, K. Nakamura *et al.*, "Review of particle physics", *J.Phys.G* **G37** (2010) 075021.

[5] R. P. Feynman, "Very high-energy collisions of hadrons", *Phys. Rev. Lett.* **23** (Dec, 1969) 1415–1417. http://link.aps.org/doi/10.1103/PhysRevLett.23.1415.

[6] J. D. Bjorken, "Asymptotic Sum Rules at Infinite Momentum", *Phys. Rev.* **179** (1969) 1547–1553.

[7] E. D. Bloom *et al.*, "High-Energy Inelastic *ep* Scattering at 6-Degrees and 10-Degrees", *Phys.Rev.Lett.* **23** (1969) 930–934.

[8] M. Breidenbach *et al.*, "Observed Behavior of Highly Inelastic Electron-Proton Scattering", *Phys.Rev.Lett.* **23** (1969) 935–939.

[9] A. Bodek, M. Breidenbach, D. Dubin, J. Elias, J. I. Friedman, *et al.*, "Experimental Studies of the Neutron and Proton Electromagnetic Structure Functions", *Phys.Rev.* **D20** (1979) 1471–1552.

Bibliography

[10] BCDMS Collaboration, A. Benvenuti *et al.*, "A High Statistics Measurement of the Proton Structure Functions $F_2(X, Q^2)$ and R from Deep Inelastic Muon Scattering at High Q^2", *Phys.Lett.* **B223** (1989) 485.

[11] H1 Collaboration, F. Aaron *et al.*, "Inclusive Deep Inelastic Scattering at High Q^2 with Longitudinally Polarised Lepton Beams at HERA", `arXiv:1206.7007 [hep-ex]`.

[12] G. Sterman *et al.*, "Handbook of perturbative QCD", *Rev. Mod. Phys.* **67** (Jan, 1995) 157–248. `http://link.aps.org/doi/10.1103/RevModPhys.67.157`.

[13] M. E. Peskin and D. V. Schroeder, *An Introduction to Quantum Field Theory.* Perseus Books, Cambridge, Massachusetts, 1995.

[14] V. Gribov and L. Lipatov, "Deep inelastic e p scattering in perturbation theory", *Sov.J.Nucl.Phys.* **15** (1972) 438–450.

[15] L. Lipatov, "The parton model and perturbation theory", *Sov.J.Nucl.Phys.* **20** (1975) 94–102.

[16] G. Altarelli and G. Parisi, "Asymptotic Freedom in Parton Language", *Nucl.Phys.* **B126** (1977) 298.

[17] Y. L. Dokshitzer, "Calculation of the Structure Functions for Deep Inelastic Scattering and e^+e^- Annihilation by Perturbation Theory in Quantum Chromodynamics.", *Sov.Phys.JETP* **46** (1977) 641–653.

[18] J. C. Collins, "Hard scattering factorization with heavy quarks: A General treatment", *Phys.Rev.* **D58** (1998) 094002, `arXiv:hep-ph/9806259 [hep-ph]`.

[19] M. Aivazis, F. I. Olness, and W.-K. Tung, "QCD formulation of charm production in deep inelastic scattering and the sea quark - gluon dichotomy", *Phys.Rev.Lett.* **65** (1990) 2339–2342.

[20] M. Aivazis, J. C. Collins, F. I. Olness, and W.-K. Tung, "Leptoproduction of heavy quarks. 2. A Unified QCD formulation of charged and neutral current processes from fixed target to collider energies", *Phys.Rev.* **D50** (1994) 3102–3118, `arXiv:hep-ph/9312319 [hep-ph]`.

[21] R. Thorne and R. Roberts, "An Ordered analysis of heavy flavor production in deep inelastic scattering", *Phys.Rev.* **D57** (1998) 6871–6898, `arXiv:hep-ph/9709442 [hep-ph]`.

[22] R. Thorne and R. Roberts, "A Practical procedure for evolving heavy flavor structure functions", *Phys.Lett.* **B421** (1998) 303–311, `arXiv:hep-ph/9711223 [hep-ph]`.

[23] M. Gluck, E. Hoffmann, and E. Reya, "Scaling Violations and the Gluon Distribution of the Nucleon", *Z.Phys.* **C13** (1982) 119.

[24] M. Gluck, R. Godbole, and E. Reya, "Heavy Flavour Production at High-Energy *ep* Colliders", *Z.Phys.* **C38** (1988) 441.

[25] M. Aivazis, F. I. Olness, and W.-K. Tung, "Leptoproduction of heavy quarks. 1. General formalism and kinematics of charged current and neutral current production processes", *Phys.Rev.* **D50** (1994) 3085–3101, `arXiv:hep-ph/9312318 [hep-ph]`.

[26] R. Thorne and R. Roberts, "A Variable number flavor scheme for charged current heavy flavor structure functions", *Eur.Phys.J.* **C19** (2001) 339–349, `arXiv:hep-ph/0010344 [hep-ph]`.

[27] R. Thorne and W. Tung, "PQCD Formulations with Heavy Quark Masses and Global Analysis", `arXiv:0809.0714 [hep-ph]`.

[28] E. Derman, "Tests for a weak neutral current in $l^{\pm} + N \longrightarrow l^{\pm} + anything$ at high energy", *Phys.Rev.* **D7** (1973) 2755–2775.

[29] G. Ingelman and R. Rückl, "Determination of Quark Distributions in *ep* Collisions", *Phys.Lett.* **B201** (1988) 369.

[30] E. Fermi, "An attempt of a theory of beta radiation.", *Z.Phys.* **88** (1934) 161–177.

[31] P. Haberl, F. Schrempp, and H. Martyn, "Contact Interactions and New Heavy Bosons at HERA", in *Proc. Workshop Physics at HERA*, W. Buchmüller and G. Ingelmann, eds., vol. 2, p. 1133. 1991.

[32] E. Eichten, K. D. Lane, and M. E. Peskin, "New Tests for Quark and Lepton Substructure", *Phys.Rev.Lett.* **50** (1983) 811–814.

[33] R. Rückl, "Effects of Compositeness in Deep Inelastic Scattering", *Phys.Lett.* **B129** (1983) 363.

Bibliography

[34] R. Rückl, "Probing Lepton and Quark Substructure in Polarised $e^{\pm}N$ Scattering", *Nucl.Phys.* **B234** (1984) 91.

[35] H. Harari, "Composite models for quarks and leptons", *Phys.Rept.* **104** (1984) 159.

[36] J. Wudka, "Composite leptoquarks", *Phys.Lett.* **B167** (1986) 337.

[37] W. Buchmüller, R. Rückl, and D. Wyler, "Leptoquarks in Lepton - Quark Collisions", *Phys.Lett.* **B191** (1987) 442–448.

[38] J. Kalinowski *et al.*, "Leptoquark / squark interpretation of HERA events: Virtual effects in e^+e^- annihilation to hadrons", *Z.Phys.* **C74** (1997) 595–603, `arXiv:hep-ph/9703288 [hep-ph]`.

[39] O. Klein, "Quantum Theory and Five-Dimensional Theory of Relativity.", *Z.Phys.* **37** (1926) 895–906.

[40] N. Arkani-Hamed, S. Dimopoulos, and G. Dvali, "The Hierarchy problem and new dimensions at a millimeter", *Phys.Lett.* **B429** (1998) 263–272, `arXiv:hep-ph/9803315 [hep-ph]`.

[41] G. F. Giudice, R. Rattazzi, and J. D. Wells, "Quantum gravity and extra dimensions at high-energy colliders", *Nucl.Phys.* **B544** (1999) 3–38, `arXiv:hep-ph/9811291 [hep-ph]`.

[42] S. Mandelstam, "Determination of the pion-nucleon scattering amplitude from dispersion relations and unitarity, general theory", *Phys. Rev.* **112** (Nov, 1958) 1344–1360. `http://link.aps.org/doi/10.1103/PhysRev.112.1344`.

[43] G. Köpp *et al.*, "Bounds on radii and magnetic dipole moments of quarks and leptons from LEP, SLC and HERA", *Z.Phys.* **C65** (1995) 545–550, `arXiv:hep-ph/9409457 [hep-ph]`.

[44] HERMES Collaboration, K. Ackerstaff *et al.*, "The HERMES spectrometer", *Nucl.Instrum.Meth.* **A417** (1998) 230–265, `arXiv:hep-ex/9806008 [hep-ex]`.

[45] H1 Collaboration, B. Andrieu *et al.*, "The H1 liquid argon calorimeter system", *Nucl.Instrum.Meth.* **A336** (1993) 460–498.

[46] C. Issever, K. Borras, and D. Wegener, "An Improved Weighting Algorithm to Achieve Software Compensation in a Fine Grained LAr Calorimeter", H1-IN-H1-03/03-608, 2003.

[47] H1 Collaboration, B. Andrieu *et al.*, "Results from pion calibration runs for the H1 liquid argon calorimeter and comparisons with simulations", *Nucl.Instrum.Meth.* **A336** (1993) 499–509.

[48] H1 Collaboration, R. Appuhn *et al.*, "The H1 lead / scintillating fiber calorimeter", *Nucl.Instrum.Meth.* **A386** (1997) 397–408.

[49] H1 Collaboration, T. Nicholls *et al.*, "Performance of an electromagnetic lead / scintillating fiber calorimeter for the H1 detector", *Nucl.Instrum.Meth.* **A374** (1996) 149–156.

[50] R. Kogler, "Measurement of jet production in deep-inelastic *ep* scattering at HERA". PhD thesis, Hamburg University, 2011. http://www-h1.desy.de/publications/theses_list.html. DESY-THESIS-2011-003, MPP-2010-175.

[51] J. Bürger *et al.*, "The Central jet chamber of the H1 experiment", *Nucl.Instrum.Meth.* **A279** (1989) 217–222.

[52] C. Kleinwort, "H1 alignment experience", in *Proc. Detector Alignement Workshop II*, pp. 41–50. 2006.

[53] D. Pitzl *et al.*, "The H1 silicon vertex detector", *Nucl.Instrum.Meth.* **A454** (2000) 334–349, arXiv:hep-ex/0002044 [hep-ex].

[54] H. Bethe and W. Heitler, "On the Stopping of fast particles and on the creation of positive electrons", *Proc.Roy.Soc.Lond.* **A146** (1934) 83–112.

[55] J. Blümlein, "Leading Log Radiative Corrections to Deep Inelastic Neutral and Charged Current Scattering at HERA", *Z.Phys.* **C47** (1990) 89–94.

[56] H1 Collaboration, F. Aaron *et al.*, "Determination of the Integrated Luminosity at HERA using Elastic QED Compton Events", *Eur.Phys.J.* **C72** (2012) 2163, arXiv:1205.2448 [hep-ex].

[57] R. Placakyte, "First measurement of charged current cross sections with longitudinally polarised positrons at HERA". PhD thesis, Ludwig-Maximilians-Univ., München, 2006. http://www-h1.desy.de/publications/theses_list.html.

[58] C. Kiesling *et al.*, "The H1 Neural Network Trigger Project", 2000.

[59] J. Bizot and D. Hoffmann, "Strategy Studies for the H1 Topological L2-Trigger (L2TT)", H1-IN-H1-1/97-508, 1997.

[60] A. Baird *et al.*, "A Fast high resolution track trigger for the H1 experiment", *IEEE Trans.Nucl.Sci.* **48** (2001) 1276–1285, `arXiv:hep-ex/0104010 [hep-ex]`.

[61] D. Meer *et al.*, "A Multifunctional processing board for the fast track trigger of the H1 experiment", *IEEE Trans.Nucl.Sci.* **49** (2002) 357–361, `arXiv:hep-ex/0107010 [hep-ex]`.

[62] H1 Collaboration, A. Schöning, "A fast track trigger for the H1 collaboration", *Nucl.Instrum.Meth.* **A518** (2004) 542–543.

[63] H1 Collaboration, A. Schöning, "The Fast Track Trigger at the H1 experiment design concepts and algorithms", *Nucl.Instrum.Meth.* **A566** (2006) 130–132.

[64] H1 Collaboration, C. Adloff *et al.*, "Measurement of neutral and charged current cross-sections in positron proton collisions at large momentum transfer", *Eur. Phys. J.* **C13** (2000) 609–639, `arXiv:hep-ex/9908059`.

[65] H1 Collaboration, C. Adloff *et al.*, "Measurement of neutral and charged current cross-sections in electron - proton collisions at high Q^2", *Eur. Phys. J.* **C19** (2001) 269–288, `arXiv:hep-ex/0012052`.

[66] A. Nikiforov, "Measurements of the neutral current $e^\pm p$ cross sections using longitudinally polarised lepton beams at HERA II". PhD thesis, Ludwig-Maximilians-Univ., München, 2007. `http://www-h1.desy.de/publications/theses_list.html`.

[67] H1 Collaboration, F. D. Aaron *et al.*, "Measurement of the inclusive $e^\pm p$ scattering cross section at high inelasticity y and of the structure function F_L", *Eur. Phys. J.* **C71** (2010) 1579, `arXiv:1012.4355 [hep-ex]`.

[68] S. Habib, "Unpolarized neutral current $e^\pm p$ cross section measurements at the H1 experiment, HERA". PhD thesis, Hamburg University, 2009. `http://www-h1.desy.de/publications/theses_list.html`. DESY-THESIS-2009-039.

[69] T. H. Tran, "Precision measurement of cross sections of charged and neutral current processes at high Q^2 at HERA". PhD thesis, Univ. Paris-Sud 11, 2010.

http://www-h1.desy.de/publications/theses_list.html.
DESY-THESIS-2011-009.

[70] S. Shushkevich, "Measurement of neutral current cross sections with longitudinally polarised leptons at HERA". PhD thesis, Ludwig-Maximilians-Univ., München, 2011.

[71] S. Bentvelsen *et al.*, "Reconstruction of (x, Q^2) and extraction of structure functions in neutral current scattering at HERA", in *Proc. Workshop: Physics at HERA*, W. Buchmüller and G. Ingelmann, eds., vol. 1, pp. 23–40. DESY, 1991.

[72] A. Blondel and F. Jacquet, "Measurement of Neutral and Charged Current Cross-Sections in Electron-Proton Collisions at High Q^2", in *Proceedings of the Study of an ep Facility for Europe*, U. Amaldi, ed., p. 391. DESY, 1979.

[73] U. Bassler and G. Bernardi, "On the kinematic reconstruction of deep inelastic scattering at HERA: The Sigma method", *Nucl.Instrum.Meth.* **A361** (1995) 197–208, arXiv:hep-ex/9412004 [hep-ex].

[74] U. Bassler and G. Bernardi, "Structure function measurements and kinematic reconstruction at HERA", *Nucl.Instrum.Meth.* **A426** (1999) 583–598, arXiv:hep-ex/9801017 [hep-ex].

[75] A. Mehta, "New Track Based Electron Finder". Talk at the H1 High Q^2 Analysis meeting, 2003. www-h1.desy.de/~mehta/trackandelectronefficiency.ps.

[76] B. Portheault, M. Peez, and E. Sauvan, "An energy flow algorithm for hadronic reconstruction in OO: Hadroo2", H1-IN-H1-IN-616, 2005.

[77] H1 Collaboration, "H1 Reconstruction documentation page". https://www-h1.desy.de/icas/imanuals/h1rec/h1rec9/h1rec.html.

[78] J. Cao and Z. Zhang, "Towards an Unbiased Measurement of Kinematic Variables at Low y Region", H1-IN-H1-12/99-580, 1999.

[79] L. Goerlich and H. P. Wellisch, "Documentation of the LAr Clustering", H1-IN-H1-IN-204/1991, 1991.

Bibliography

[80] C. Veelken, "H1NonepBgFinder - Rejection of cosmic muon and beam-halo events in the H1OO framework", H1-IN-H1-09/02-603, 2002.

[81] B. Portheault and Z. Zhang, "Radiative Corrections for Charged Current Process at HERA Revisited", H1-IN-H1-11/04-614, 2004.

[82] J. Pumplin *et al.*, "New generation of parton distributions with uncertainties from global QCD analysis", *JHEP* **0207** (2002) 012, `arXiv:hep-ph/0201195 [hep-ph]`.

[83] H.-L. Lai *et al.*, "New parton distributions for collider physics", *Phys.Rev.* **D82** (2010) 074024, `arXiv:1007.2241 [hep-ph]`.

[84] A. D. Martin *et al.*, "Parton Distributions for the LHC", *Eur. Phys. J.* **C63** (2009) 189–285, `arXiv:0901.0002 [hep-ph]`.

[85] R. D. Ball *et al.*, "", *Nucl. Phys. B.* **849** (2011) 296, `arXiv:1002.4407 [hep-ph]`.

[86] E. Perez and E. Rizvi, "The Quark and Gluon Structure of the Proton", `arXiv:1208.1178 [hep-ph]`.

[87] H1 and ZEUS Collaboration, F. D. Aaron *et al.*, "Combined Measurement and QCD Analysis of the Inclusive ep Scattering Cross Sections at HERA", *JHEP* **01** (2010) 109, `arXiv:0911.0884 [hep-ex]`.

[88] H1 Collaboration, C. Adloff *et al.*, "Measurement and QCD analysis of neutral and charged current cross-sections at HERA", *Eur.Phys.J.* **C30** (2003) 1–32, `arXiv:hep-ex/0304003 [hep-ex]`.

[89] H1 Collaboration, F. Aaron *et al.*, "A Precision Measurement of the Inclusive ep Scattering Cross Section at HERA", *Eur.Phys.J.* **C64** (2009) 561–587, `arXiv:0904.3513 [hep-ex]`.

[90] R. J. Barlow, *Statistics: A Guide to the Use of Statistical Methods in the Physical Sciences (Manchester Physics Series)*. WileyBlackwell, reprint ed., 1989.

[91] G. Cowan, *Statistical Data Analysis*. Oxford University Press, Oxford, 1998.

[92] F. Huber, "Elastic and Proton Dissociative J/ψ Photoprodiction at low $W_{\gamma p}$ with the H1 Detector at HERA". PhD thesis, Heidelberg University, 2012.

[93] J. Sherman and W. J. Morrison, "Adjustment of an inverse matrix corresponding to a change in one element of given matrix", *Ann. Math. Stat.* **21** (1950) 124–127.

[94] D. Stump *et al.*, "Uncertainties of predictions from parton distribution functions. 1. The Lagrange multiplier method", *Phys.Rev.* **D65** (2001) 014012, `arXiv:hep-ph/0101051 [hep-ph]`.

[95] V. Blobel, "Comments on χ^2 minimisation", 2003. `http://www.desy.de/~blobel/Tcommchi.pdf`.

[96] A. Glazov, "Data combination". Talk at School on data combination and limit setting, 2011. `https://indico.desy.de/getFile.py/ access?contribId=9&resId=1&materialId=slides&confId=4489`.

[97] A. Glazov, "Combination of H1 data, xF_3 and chi^2 studies". Talk at H1 ELAN group meeting, 2011. `https://www-h1.desy.de/ icgi-h1wiki/moin.cgi/ElanInclusive/Meeting2011-09-13? action=AttachFile&do=get&target=sasha.pdf`.

[98] M. Botje, "QCDNUM: Fast QCD Evolution and Convolution", *Comput.Phys.Commun.* **182** (2011) 490–532, `arXiv:1005.1481 [hep-ph]`.

[99] F. James and M. Roos, "Minuit: A System for Function Minimization and Analysis of the Parameter Errors and Correlations", *Comput.Phys.Commun.* **10** (1975) 343–367.

[100] M. Beckmann *et al.*, "The Longitudinal polarimeter at HERA", *Nucl.Instrum.Meth.* **A479** (2002) 334–348, `arXiv:physics/0009047 [physics]`.

[101] F. Corriveau *et al.*, "A Callibration of the HERA Transverse Polarimeter for the 2003/2004 Data", 2004. `http://www.desy.de/~pol2000/documents/`.

[102] R. S. Thorne, "Variable-flavor number scheme for next-to-next-to-leading order", *Phys. Rev.* **D73** (2006) 054019, `arXiv:0601245 [hep-ph]`.

[103] R. K. Ellis, W. Furmanski, and R. Petronzio, "Unraveling Higher Twists", *Nucl.Phys.* **B212** (1983) 29.

Bibliography

[104] NuTeV Collaboration, D. Mason *et al.*, "Measurement of the Nucleon Strange-Antistrange Asymmetry at Next-to-Leading Order in QCD from NuTeV Dimuon Data", *Phys. Rev. Lett.* **99** (2007) 192001.

[105] J. Pumplin *et al.*, "Uncertainties of predictions from parton distribution functions. 2. The Hessian method", *Phys.Rev.* **D65** (2001) 014013, `arXiv:hep-ph/0101032 [hep-ph]`.

[106] J. Pumplin, D. Stump, and W. Tung, "Multivariate fitting and the error matrix in global analysis of data", *Phys.Rev.* **D65** (2001) 014011, `arXiv:hep-ph/0008191 [hep-ph]`.

[107] Z. J. Ajaltouni *et al.*, "Proceedings of the workshop: HERA and the LHC workshop series on the implications of HERA for LHC physics", `arXiv:0903.3861 [hep-ph]`.

[108] ATLAS Collaboration, G. Aad *et al.*, "Determination of the strange quark density of the proton from ATLAS measurements of the W and Z cross sections", *Phys.Rev.Lett.* **109** (2012) 012001, `arXiv:1203.4051 [hep-ex]`.

[109] F. D. Aaron *et al.*, "Search for Contact Interactions in ep Collisions at HERA", *Phys. Lett.* **B705** (2011) 52–58, `arXiv:1107.2478 [hep-ex]`.

[110] H1 Collaboration, C. Adloff *et al.*, "Search for new physics in $e^{\pm}q$ contact interactions at HERA", *Phys.Lett.* **B568** (2003) 35–47, `arXiv:hep-ex/0305015 [hep-ex]`.

[111] F. D. Aaron *et al.*, "Search for First Generation Leptoquarks in ep Collisions at HERA", *Phys. Lett.* **B704** (2011) 388–396, `arXiv:1107.3716 [hep-ex]`.

[112] OPAL Collaboration, G. Abbiendi *et al.*, "Tests of the standard model and constraints on new physics from measurements of fermion pair production at 183 GeV at LEP", *Eur.Phys.J.* **C6** (1999) 1–18, `arXiv:hep-ex/9808023 [hep-ex]`.

[113] L3 Collaboration, M. Acciarri *et al.*, "Search for manifestations of new physics in fermion pair production at LEP", *Phys.Lett.* **B489** (2000) 81–92, `arXiv:hep-ex/0005028 [hep-ex]`.

[114] D0 Collaboration, V. Abazov *et al.*, "Search for pair production of first-generation leptoquarks in p anti-p collisions at $\sqrt{s} = 1.96$ TeV", *Phys.Lett.* **B681** (2009) 224–232, `arXiv:0907.1048 [hep-ex]`.

[115] D0 Collaboration, V. Abazov *et al.*, "Search for first generation leptoquark pair production in the electron + missing energy + jets final state", *Phys.Rev.* **D84** (2011) 071104, `arXiv:1107.1849 [hep-ex]`.

[116] CMS Collaboration, V. Khachatryan *et al.*, "Search for Pair Production of First-Generation Scalar Leptoquarks in *pp* Collisions at $\sqrt{s} = 7\,\text{TeV}$", *Phys.Rev.Lett.* **106** (2011) 201802, `arXiv:1012.4031 [hep-ex]`.

[117] CMS Collaboration, S. Chatrchyan *et al.*, "Search for First Generation Scalar Leptoquarks in the evjj channel in *pp* collisions at $\sqrt{s} = 7\,\text{TeV}$", *Phys.Lett.* **B703** (2011) 246–266, `arXiv:1105.5237 [hep-ex]`.

[118] ATLAS Collaboration, G. Aad *et al.*, "Search for pair production of first or second generation leptoquarks in proton-proton collisions at $\sqrt{s} = 7\,\text{TeV}$ using the ATLAS detector at the LHC", *Phys.Rev.* **D83** (2011) 112006, `arXiv:1104.4481 [hep-ex]`.

[119] ZEUS Collaboration, S. Chekanov *et al.*, "Search for contact interactions, large extra dimensions and finite quark radius in e p collisions at HERA", *Phys.Lett.* **B591** (2004) 23–41, `arXiv:hep-ex/0401009 [hep-ex]`.

[120] ATLAS Collaboration, G. Aad *et al.*, "Search for first generation scalar leptoquarks in *pp* collisions at $\sqrt{s} = 7$ TeV with the ATLAS detector", *Phys.Lett.* **B709** (2012) 158–176, `arXiv:1112.4828 [hep-ex]`.

[121] CMS Collaboration, S. Chatrchyan *et al.*, "Search for pair production of first- and second-generation scalar leptoquarks in *pp* collisions at $\sqrt{s} = 7$ TeV", *Phys.Rev.* **D86** (2012) 052013, `arXiv:1207.5406 [hep-ex]`.

[122] ATLAS Collaboration, G. Aad *et al.*, "Search for contact interactions and large extra dimensions in dilepton events from *pp* collisions at $\sqrt{s} = 7$ TeV with the ATLAS detector", *Phys.Rev.* **D87** (2013) 015010, `arXiv:1211.1150 [hep-ex]`.

[123] CMS Collaboration, S. Chatrchyan *et al.*, "Search for contact interactions in opposite-sign dimuon events in *pp* collisions at $\sqrt{s} = 7$ TeV", `arXiv:1212.4563 [hep-ex]`.

Bibliography

[124] CMS Collaboration, V. Khachatryan *et al.*, "Measurement of Dijet Angular Distributions and Search for Quark Compositeness in *pp* Collisions at $\sqrt{s} = 7\,\text{TeV}$", *Phys.Rev.Lett.* **106** (2011) 201804, `arXiv:1102.2020 [hep-ex]`.

[125] ATLAS Collaboration, G. Aad *et al.*, "Search for contact interactions in dilepton events from *pp* collisions at $\sqrt{s} = 7\,\text{TeV}$ with the ATLAS detector", *Phys.Lett.* **B712** (2012) 40–58, `arXiv:1112.4462 [hep-ex]`.

[126] CMS Collaboration, S. Chatrchyan *et al.*, "Search for large extra dimensions in dimuon and dielectron events in *pp* collisions at $\sqrt{s} = 7$ TeV", *Phys.Lett.* **B711** (2012) 15–34, `arXiv:1202.3827 [hep-ex]`.

[127] K.-m. Cheung, "Constraints on electron quark contact interactions and implications to models of leptoquarks and extra Z bosons", *Phys.Lett.* **B517** (2001) 167–176, `arXiv:hep-ph/0106251 [hep-ph]`.

[128] D0 Collaboration, V. Abazov *et al.*, "Search for Large extra spatial dimensions in the dielectron and diphoton channels in $p\bar{p}$ collisions at $\sqrt{s} = 1.96\,\text{TeV}$", *Phys.Rev.Lett.* **102** (2009) 051601, `arXiv:0809.2813 [hep-ex]`.

[129] D0 Collaboration, V. Abazov *et al.*, "Measurement of dijet angular distributions at $\sqrt{s} = 1.96\,\text{TeV}$ and searches for quark compositeness and extra spatial dimensions", *Phys.Rev.Lett.* **103** (2009) 191803, `arXiv:0906.4819 [hep-ex]`.

[130] F. James, *Statistical Methods in Experimental Physics.* World Scientific Publishing Co., 2006.

Acknowledgment

In the end of my thesis, I would like to thank all the people who helped this work to happen. Your knowledge and experience allowed me to successfully complete my more than three years long journey. The contribution of yours is really invaluable. The risk to miss somebody while thanking you name by name is very high, so I am just skipping that part and simply saying "Thank you very much".